12-2016

Ceramic Thin Films with Embedded Magnetic Nanofibers or Nanorods of Controlled Orientations

Zhaoxi Chen
Clemson University, zhaoxic@g.clemson.edu

CERAMIC THIN FILMS WITH EMBEDDED MAGNETIC NANOFIBERS OR NANORODS OF CONTROLLED ORIENTATIONS

A Dissertation
Presented to
the Graduate School of
Clemson University

In Partial Fulfillment
of the Requirements for the Degree
Doctor of Philosophy
Materials Science and Engineering

---

by
Zhaoxi Chen
December 2016

Accepted by:
Dr. Fei Peng, Committee Chair
Dr. Konstantin Kornev
Dr. Rajendra K. Bordia
Dr. Igor Luzinov
Dr. Huijuan Zhao

ABSTRACT

Ceramic thin films embedded with oriented magnetic nanofibers or nanorods are highly demanded for the applications in remote sensing, electromagnetic shielding, and thermal management at high temperatures. The general strategy for developing ceramic composite thin films with aligned magnetic nanorods or nanofibers has not been developed yet. This dissertation is centered on fundamentally understanding a sol-gel and polymer-based route towards creation of ceramic thin films with aligned magnetic nanostructures. The topics cover fabrication and properties of ceramic and ceramic-based nanofibers, precipitating magnetic nanoparticles within ceramic fibers, aligning and embedding nanofibers or nanorods within ceramic films, and preventing cracking during the sol-gel film dip-coating processing on flat substrates or on substrates with protrusions such as nanorods or nanofibers. The recent status and challenges in developing ceramic based nanocomposite and its potential applications are reviewed in chapter I. The feasible methodologies and general approaches are described. In chapter II and chapter III, we present the development of mullite and mullite-based composite nanofibers as potential fillers in ceramic thin films. The detailed schemes of materials formation and approaches for microstructure control are discussed in detail. The mechanical and magnetic properties of the mullite-based fibers are studied. In chapter IV, the high temperature in situ precipitation of nickel nanoparticles within the mullite fiber host is studied, to fundamentally understand the processing mechanism and its potential for high temperatures applications. In chapter V, we present the fundamental understanding of processing crack-free mullite thin films by sol-gel method. In chapter VI, the scientific

approach is described for processing macroscopic ceramic thin films embedded with magnetic nanorods of controlled alignment. In chapter VII, the ceramic thin film formation with embedded nanorods is studied both theoretically and experimentally. The mechanism and criterion of microscopic cracking within the thin film composites is discussed.

DEDICATION

This dissertation is dedicated to my wife Ying Ma and my family in China for their support.

ACKNOWLEDGMENTS

Foremost, I would like to express my greatest appreciation to Professor Fei Peng, my Ph. D. advisor, for his kind guidance, support and patience during my graduate study at Clemson University. He is not only a tremendous mentor who provides me with valuable advices on my researches, but also a helpful friend who supports my choices and gives me useful life guidance. I will always cherish the memories of working under his supervision.

Very special thanks to Professor Konstantin Kornev, who has been helpful in providing advice many times during my graduate school career. He is so knowledgeable and insightful, and can always enlighten me with better ideas and greater improvement. My sincere thanks also goes to my committee members, Professor Rajendra Bordia, Professor Igor Luzinov and Professor Huijuan Zhao, for their profound comments and valuable suggestions.

I also want to thank my group mates and collaborators, Dr. Yu Gu, Dr. Ruslan Burtovyy, Mr. Zhao Zhang, Mr. Yuzhe Hong, Mr. Jincheng Lei, Mr. James Townsend, Mr. Arthur Salamatin and Mr. Pavel Aprelev. I enjoyed the time when we cooperate on various projects, when we do brainstorming on research issues, when we eat and laugh together and when we encourage each other during difficulties.

I also want to give thanks to my beloved wife, Ying Ma. Words cannot express how grateful I am. Her kind support and encouragement to me throughout this experience is what sustained me so far.

TABLE OF CONTENTS

Page

LIST OF TABLES

List of Tables (Continued)

Table Page

LIST OF FIGURES

List of Figures (Continued)

Figure Page

List of Figures (Continued)

Figure Page

List of Figures (Continued)

Figure Page

List of Figures (Continued)

Figure Page

List of Figures (Continued)

Figure Page

List of Figures (Continued)

Figure Page

CHAPTER I

INTRODUCTION

1.1 Applications

Nanocomposites are a family of materials made of dissimilar phases with at least one phase dispersed at nanoscale, typically smaller than 100 nm. Nanocomposite materials circumscribe an extensive forms of materials, including zero-dimensional (*e.g.* core-shell nanoparticles), one-dimensional (*e.g.* composite filamentary structures), two dimensional (*e.g.* layered films) or bulk. A nanocomposite usually consists of a continuous phase (the matrix) and a dispersed phase (the filler).

Ceramic nanocomposites enjoy broad applications in energy conversion, construction, automotive, nuclear energy, aerospace, electronics and power generations [1]. They generally have the advantages of higher strength, thermal stability and chemical inertness and unique optical and electronic properties, making them exceptionally good candidates for the applications at elevated temperatures and in harsh environments. For example, adding nanofiber or nanorods in ceramics can greatly enhance the mechanical performances of ceramic materials [2-4].

Composite materials with aligned nanorods are especially attractive for applications in a wide variety of fields [2, 5-9]. Our goal in this dissertation is to develop ceramic thin films with embedded magnetic nanorods or nanofibers of controlled orientations. The materials are anticipated with multiple functions. The principle of

materials design is governed by a synergetic combination of the following expected properties.

1.1.1 Corrosion resistance and wear protection

Corrosion and wear are combined in many applications, for example, in combustion engines and turbine engines. Ceramic thin films are corrosion and wear resistant materials owing to their inherent chemical inertness, high elastic modulus and hardness. It is desired to apply ceramic thin films or coatings on metal substrates to provide these environmental and mechanical protections.

For such applications, dense and mechanically robust ceramic coatings with tunable thickness are desired in principle. Cracks are deleterious for applications in corrosive media. It is often the cause of poor mechanical properties. The crack formation is often irreversible, therefore cracking in the thin film matrix during processing should be eliminated. In addition, the segregation of nanorods often initiates cracks when used as fillers in composites [2-4]. The design principle requires: the homogeneous distribution of the nanofibers or nanorods in the thin film matrix; dense and crack-free thin films.

1.1.2. Faraday rotators

A Faraday rotator is a polarization rotator based on the Magneto-optic effect. It is caused by the phase velocity difference of the left and right circularly polarized waves (*e.g.* a linearly polarized light can be considered as the superposition of two identical circularly polarized waves rotating in opposite directions). Magnetic nanorods and nanofibers demonstrate superior and unique magnetic, magnetooptic and magnetotransport properties [10, 11]. The alignment of the magnetic nanorods and chains within the film offers

optically anisotropic properties [12-15]. This phenomenon was first observed in the magnetic fluids subjected to the magnetic field, and the magnetic particles in the fluids aggregates to form aligned chains (1D) and induce magnetic anisotropy [12-14]. The Faraday effect in composite thin film with aligned magnetic chains demonstrates the following characteristics. When magnetic field was off, the thin film composite was optically isotropic and the polarization changes through the film does not depend on the chain orientation, which is in general governed by the Faraday effect of the magnetic materials [13]. In magnetic field, the polarization of light depends on the chain orientation [13].

1.1.3. Microwave absorption

One particular application of the magnetic composite films with ferromagnetic nanoparticles is the microwave absorption at the ferromagnetic resonance (FMR) frequencies [16-23]. The FMR frequency of the composite film can be controlled by the shape, size and concentration of ferromagnetic nanoparticles in a composite. Under no external magnetic field, the FMR frequency shifts to lower values and the intensity increases as the concentration of the nanoparticle increases [23]. The coefficient of microwave absorption also increases as the concentration of the magnetic nanoparticles increases. Enhanced microwave absorption at the ferromagnetic resonance (FMR) frequency was observed in single domain ferromagnetic nanoparticles, which typically presents with small particle size [24, 25].

Due to a combination effect of shape and magnetocrystalline anisotropy, ferromagnetic nanorods or nanofibers often demonstrate anisotropic magnetization

behavior [26]. The effects of magnetic nanorod alignment on microwave absorption were demonstrated in the composite film with vertically aligned nanorods [16-22]. This type of materials is sometimes called ferromagnetic nanowire metamaterials [19]. This configuration of nanorods alignment is because that the materials are typically obtained by electrodeposition in nanoporous membranes [17, 19]. The FMR studies were usually carried out with different external fields (the field swept mode). Due to the anisotropic magnetization behavior of the nanorods, the equilibrium magnetization of the composite film depends on the sample geometry and its relative orientation to the external magnetic field [16, 17]. This results in the specific dependence of the FMR field positions and line width on the direction of applied magnetic fields [16, 17]. In general, the orientation of magnetic nanorods offers additional degree of freedom to tune the microwave absorption properties of the composite films. As the absorbed energy dissipates into heat, it is also desired to have the nanorods orientation for potential applications in controlled heat dissipations and thermal managements [27]. In principle, a feasible process should be able to control the concentration of magnetic nanoparticles in the composite film, the size of the magnetic nanoparticles or nanorods, the orientation of the nanorods.

Additional applications of ceramic films with oriented magnetic nanofibers or nanorods can be found in high density magnetic recording and magnetic sensors. With aligned ferromagnetic nanostructures, the preferred magnetization can be achieved in a thin film matrix with enhanced coercivities [10]. Specific magnetization anisotropy admits a smaller bit size with higher magnetic recording density.

1.2 Scientific challenges

The goal of this thesis is to explore the fundamental thermodynamics and kinetics of processing low dimensional ceramics (e.g. thin films, fibers, and nanoparticles) driven by the local equilibrium, especially the processing science and kinetic phenomena driven under the local surface and strain energies. These phenomena have wide impacts on a number of key phenomena in materials science, such as cracking in film, nucleation and growth of nanoparticles.

1.2.1 Mechanical characterization of ceramic fibers of small diameters

Mechanical characterization of ceramic fibers of small diameters (<10μm) is a difficult task. Due to its brittleness, ceramic fiber readily suffers mechanical failure even at small deformations. This makes it very difficult to handle the fibers without damaging them [28, 29]. This is why reports on measuring mechanical properties of ceramic microfibers obtained from electrospinning can rarely be found. For this reason, the conventional method of tensile test is often applicable only for thick ceramic fiber, with a diameter greater than tens of micrometers [30]. Due to these difficulties, microfibers are typically tested in strands composed of many individual fibers [31, 32] and then different mathematical models have been employed to interpret the data [33]. A simple and cost-efficient method of measuring the mechanical property of individual fiber should be developed and verified.

1.2.2 Coarsening of nanoparticles (NPs) at high temperatures

High temperature stability of metal nanoparticles has been a long standing problem in the field of catalysis and high power laser plasmonics [34-37]. Over time, the metal NPs suffer degradation at high temperatures and, if embedded with ceramic materials, they are

prone to coalesce and sinter [38-40]. Coarsening is usually irreversible and nanoparticles have an inherent tendency to grow in order to minimize their total surface energy. Although controlling the size of metal NPs at high temperatures is highly desired, stabilization of them with respect to coarsening is difficult to achieve. It is generally believed that the Ostwald ripening is the underlying process of NP coarsening at high temperatures [41-43]. However, the theory is in contradictory with many cases, e.g. the observation of growth stagnation. A theory with appropriate explanation remains unclear.

The problem of interactions of elastic nuclei with an elastic matrix stands at the core of materials science and solid mechanics. The model of a NP equipped with an interfacial layer having a residual spontaneous stress became popular as it is adapted from the fluid mechanics model of a drop with and interfacial Laplace-Young tension [44]. For a constant surface energy and elastic moduli, the radial displacement due to the interfacial stress should not depend on the particle size [45, 46]. However, these theories often assume constant transformation strains which has no dependence on the particle size [45, 46]. The hypothesis of size-dependent transformation strain has essential impacts to the classical theories, and should be examined carefully. This study brings new perspective to the non-classical theory and has broad impact to both the fundamental understanding and materials design principles.

1.2.3 Cracking during thin film processing

Films and coatings deposited on rigid substrates often develop large in-plane tensile stress [47-50]. This tensile stress could be due to the residual stress caused by the thermal expansion mismatch or the capillary forces during thin film processing (e. g. thin film

processed from solution) [47-51]. For example, solvent evaporation, polymerization reactions and sintering produce a shrink tendency for the film [47-50]. Thus intrinsic stress develops due to the capillary forces. This intrinsic stress, when exceeded the material's limit, caused the failure of the film [47-50]. It is difficult to prevent cracking due to the stress, especially for thick films. The maximum film thickness of non-repetitive deposition above which the cracking occurs is often termed as "critical thickness" (τ_c). For sol-gel derived ceramic coatings, the τ_c value is typically below 100 nm [49, 50].

Although the cracking problem in thin films has been extensively studied over the years, the crack formation in thin films with the nanorods remains unclear. It is sometimes challenging to process crack-free thin films embedded with nanorods, although the thin film itself (without the presence of rods) is free of cracks. When processing thin films with nanorods inclusions, the presence of such features often cause topographic evolution of the films, which gives rise to non-uniform thickness [52-58]. The thickness evolution, sometimes planarization is driven by the local equilibrium between surface tension and the hydrostatic pressure in the liquid at rest [52-54]. It is practical to apply the concept of critical thickness to determine the cracking criterion in thin films with different film thickness. The application of critical thickness concept to the cracking problem with non-uniform film thickness needs to be verified. The study contributes to a more comprehensive understanding of the cracking problem during thin film processing.

1.2.4 Aligning nanofibers and nanorods

There are a number of reported methods to process ceramic thin films with aligned nanofibers or nanorods. These include the *in-situ* growth of nanorods within the thin film

templates or deposition of ceramic thin film on pre-aligned nanorods [59, 60]. For example, the anodizing method was used to generate nanoporous alumina thin film template with highly ordered pore-templates normal to the reacting surface, followed by integration of carbon nanotubes using chemical vapor deposition (CVD) [4]. In the other approaches, nanorods were aligned normal to the plane of substrate by template-based growth, hydrothermal or laser deposition [61-65]. Those methods are in general, limited to a few kinds of nanofibers or nanorods. Additionally, very few of them can be applied to achieve the alignment macroscopically.

To our best knowledge, there are only few successful attempts in making ceramic composite thin films with magnetic nanorods or nanofibers of controlled orientations [66]. Magnetic nanofibers or nanorods can be aligned in polymer solutions under externally applied magnetic fields [13, 23, 67, 68]. When the motion of nanorods are constrained two dimensionally (e.g. in a thin film), the criterion for alignment can be derived from theoretical approaches [69]. The distribution function theory explains the alignment of ferromagnetic nanorods in solidifying polymer films [87]. However, the criterion for aligning superparamagnetic nanorods remains unclear.

1.2.5 Thin film evolution on substrates with nanofibers

Innovative processing methods are conceived to make the thin film materials with oriented nanofibers/nanorods in macroscopic and cost-effective manner. Especially, it is beneficial to have a simple method of thin film implementation with precise control of film thickness. The sol-gel method is versatile in processing ceramic thin films [70, 71]. It allows processing via liquids of low viscosity, with intriguing prospects of tailoring the

morphology of thin films with the nanofibers. The morphology of the film is not only determined by the coating parameter (e.g. parameters used in dip-coating), but also the dynamic equilibrium of the liquid film with nanofiber inclusions. The mechanism of thin film evolution, including the layer thickness evolution of liquid films in the vicinity of nanofibers, remains unclear. A dynamic model needs to be developed to explain the observed phenomena.

1.3 General approach

The general experimental approach is shown in Figure 1.1. The sol-gel/electrospinning method was used to align nanofibers on a substrate. The magnetic field assisted assembly was used to align magnetic nanorods . The sol-gel/dip-coating method was used to process ceramic thin films and to cope with the above two methods for the generation of thin film nanocomposites.

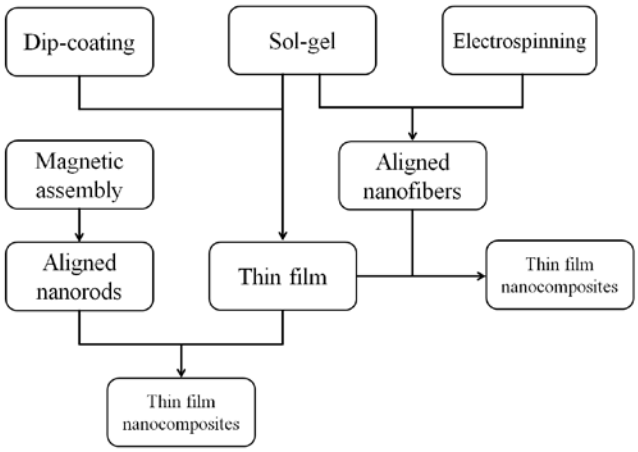

Figure 1.1. The general scheme for the fabrication of ceramic thin film nanocomposites embedded nanofibers of controlled orientations

1.3.1 Sol-gel techniques

The most commonly used precursors for processing ceramics include inorganic salts, hydroxides, alkoxides and other organic salts. Metal alkoxides belong to the family of *metalorganic* compounds. They are most commonly used as the precursors. During the sol-gel processing, metal alkoxides undergo the following hydrolysis and condensation reactions [72]:

$$M(OR)_n + H_2O \rightleftharpoons M(OR)_{n-1} - OH + ROH \tag{1.1}$$

and,

$$M(OR)_{n-1}OH + OHM(OR)_{n-1} \rightleftharpoons M(OR)_{n-1} - O - M(OR)_{n-1} + H_2O \tag{1.2}$$

where *M* stands for metal ion and *R* stands for the alkyl group. The hydrolysis reaction is the replacement of the alkoxide groups (-*OR*) with hydroxyl group (-*OH*) and releasing of the alcohol molecules (*ROH*). Subsequent condensation reactions involve the combination of hydroxyl group which leads to the oxygen bridge between metal ions. The condensation reaction is followed by an inorganic polymerization process. Effectively, water serves as a catalyst regent as it is consumed during hydrolysis and then generated during the condensation process. The hydrolysis, condensation and polymerization reactions strongly depend on the pH of the solutions. For example, controlled hydrolysis reaction in moderate acidic condition favors the polymerization in a preferentially linear arrangement, which facilitates the fiber formation from the sol-gel precursor [73]. The polymerization greatly restricts chemical diffusion and phase segregation, which is desired for making high purity product and lower the reaction temperature [72].

In a sol-gel system containing more than two metal ions, special attention should be given to the reaction rates between the species. For example, titanium or aluminum

alkoxide is much more reactive with water than alkoxisilanes due to the lower electronegativity and higher *Lewis* acidity [72]. Different reaction rates of the alkoxides within one system may result in significant phase separation and degraded mixing levels between the constituents. Depending on the homogeneity level of the metal ions, a ceramic gel can be further categorized as monophasic gel or diphasic gel [74]. Monophasic gels are endowed with atomic-level mixing. The gel is diphasic when the homogeneity level is in the nanoscale (1-100 nm). The monophasic gel is desired for two reasons. First, it favors complete phase formation without significant grain growth at relatively low temperatures. Second, formation of metastable intermediate phases can be avoided. The homogeneity level can be controlled by adjusting precursor reactivity with the organic additives such as carboxylic acids and acetylacetonate which serve as chelating regents [74]. It can also be adjusted by replacing the more reactive alkoxide by a hydrated salt [74].

1.3.2 Synthesis of mullite

Mullite is an aluminosilicate belonging to a class of refractory ceramics. It has been endowed with excellent high temperature strength, creep resistance, and good chemical stability [75-77]. This is why mullite has been widely used in ceramic matrix composites and the thermal and environmental barrier films for components operated at severe environments [78, 79]. The sol-gel method has been widely used for synthesizing mullite. According to the homogeneity degree, the precursor gel for mullite is often divided by monophasic and diphasic. A phase that can appear during mullite synthesis is the spinel type intermediate phase. The formation of spinel phase that usually appears in di-phasic gel indicates the homogeneity level of the precursor. It’s usually due to the difficulty of

controlling hydrolysis and condensation rates of the alkoxides. The monophasic precursors for mullite are obtained from a solution containing tetraethylorthosilicate (TEOS), aluminum isopropoxide (AIP) and aluminum nitrate (AN) [74]. Some other reports generate monophasic precursors from two of the above precursors such as AN and TEOS, which is usually obtained in an alcoholic solution with slow hydrolysis [80]. Formation of monophasic mullite gels indicates that aluminum and silicon are mixed at atomic level. These gels are formed by replacing silicon in the silica three dimensional network by atoms or hydrolyzed aluminum molecules, giving rise to the formation of Si-O-Al bonding similar to the bond formed during the crystallization stage [74]. The formation of the bonding at low temperatures decreases the temperature of crystallization, which is important for low temperature synthesis of mullite. For mullite synthesis, chemically synthesized precursors are converted into mullite between 850 and 1350°C. The conversion temperature further depends on the homogeneity level of the precursor synthesized. This is significantly lower than the classical solid-state reaction from powder mixtures, for example, with a formation temperature ranging from 1500 to 1700°C [75].

1.3.3 Sol-gel nanocomposites

Sol-gel nanocomposites belong to an important class of sol-gel materials. Among the synthesis techniques for advanced ceramic nanocomposites, sol-gel is certainly one of the most attractive ones. Sol-gel can be made to obtain both the matrix and the filler of the nanocomposite. Even from a same precursor, powders, fibers and thin films can be made. Inherently, it’s capable of chemically adjust the interface to optimize structure and properties [72].

Ceramic nanocomposite can be directly made by taking advantage of the sol-gel method to include all precursors in one liquid batch, including the precursors for both the matrix and fillers. The matrix is typically obtained by the hydrolysis and condensation reactions, and the dispersed phase remains inside the matrix as precipitated salts or in an ionic state. The phase separation is triggered by chemical reactions or by thermal treatment. Precursors for both the matrix and dispersed phase (e. g. nanoparticles) were mixed to form a stable sol at the first step. Hydrolysis and condensation reactions of the precursors lead to the gelation. They can also be generated during the thermal treatment of the dried gel. For example, in situ thermal reduction was applied to the materials derived from sol gel to obtain ceramics with finely dispersed magnetic nanoparticles [81, 82]. The advantage of the in situ strategy is assigned to the reduced number of steps in the preparation. Although it's convenient to generate nanocomposites from this approach, fundamental understanding should be made to the in situ process which involves the formation of multiple phases, because nanostructures can be very difficult and sometimes even impossible to obtain [72].

1.3.4 Magnetic assembly

Ceramic thin film composites are desired in many modern electronics and optics devices with miniaturized sizes and complex shapes. Challenges in ceramic thin film nanocomposites remain in the process made with commercial viable processing methods [83]. The major findings so far in thin film composites with aligned nanostructures mainly address polymer nanocomposites [84-86]. In polymer films, magnetic nanorods can be readily aligned under magnetic field [67]. Non-magnetic nanorods can be coated with minimum amount of magnetic nanoparticles, which simultaneously enriches the materials

with the magnetic induced functions [84-86] As schematically shown in figure 1.2, orientation of nanorods can be controlled by using small and moderate magnetic fields within a drying or curing polymer solution [87]. The degree of alignment is controlled by the kinetics of both nanorod rotation and film solidification/curing process [87].

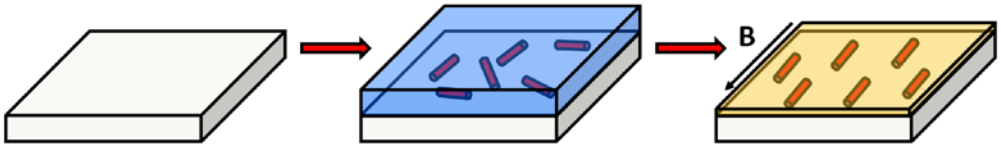

Figure 1.2. Using magnetic field to align nanorods in solidifying polymer films

Ceramic thin films embedded with oriented nanorods have not been developed yet. The magnetic field assisted assembly demonstrates intrinsic advantages in processing thin films composites with oriented magnetic nanorods. Making ceramic thin film composite from the magnetic field assembly method should be explored with the combination of wet-chemistry methods such as the sol-gel.

1.3.5 Electrospinning

Electrospinning has been extensively explored as a versatile tool of generating nanofibers with designed nanofiber size, alignment and compositions. In a typical process, the polymeric solutions are loaded into a syringe and extruded from the orifice of a needle (as shown in Figure 1.3). A high voltage electric field is applied to the needle. When the electric field is sufficiently strong, surface charges are built up and the static electric repulsive forces will overcome the surface tension to induce the formation of a jet stretched toward the grounded collector.

Electrospinning was at first designed for processing polymer fibers from organic solutions. Polymer solution or melt with appropriate rheological properties can be made to meet the requirement of electrospinning [88]. Direct spinning of ceramic fibers is considered only in principle possible from their melts at high temperatures [89]. With the success in the fields of polymer-derived ceramics and sol-gel, chemists and materials scientists were able to prepare spinnable ceramic precursors for electrospinning [90]. An extensive variety of oxide nanofibers have been processed with the notable examples of Al_2O_3, SiO_2, mullite, ZnO, TiO_2, $BaTiO_3$, Fe_2O_3, $NiFe_2O_4$ and $Y_3Al_5O_{12}$ (YAG). etc [91-97]. The have also been extended to make non-oxide ceramics such as the carbide, boride and nitride nanofibers [98-100]. One advantage of electrospinning method for ceramic nanofiber processing is assigned to the tunable properties of the nanofibers readily controlled by the precursor conditions for electrospinning [101]. It also has the capability of scaling up to the commercial level [102].

The precursors for electrospinning of ceramic nanofibers are usually categorized as co-precipitation (PPT) and sol-gel precursors [103]. In the co-precipitation method, inorganic salts (e. g. hydrated salts) of metals are typically used as the ceramic precursors [104]. This method usually requires high polymer content as spin-aid, because the precursor solutions (without adding polymers) shows limited spinnability [90]. Sol-gel precursors differ from PPT precursors as it involves sol-gel reaction with strict control of polymerization process proceeded by hydrolysis and condensation reactions. The precursors with certain spinnability can be derived from the sol-gel process [105-107]. The combination of electrospinning with sol-gel processing is feasible to obtain ceramic fibers

from this approach as it may require less spin-aid to form fibers with desired microstructures [108]. For both PPT and sol-gel method, the fibers obtained from electrospinning (usually called as-spun fibers or green fibers) need to be heat treated to convert into ceramics fibers.

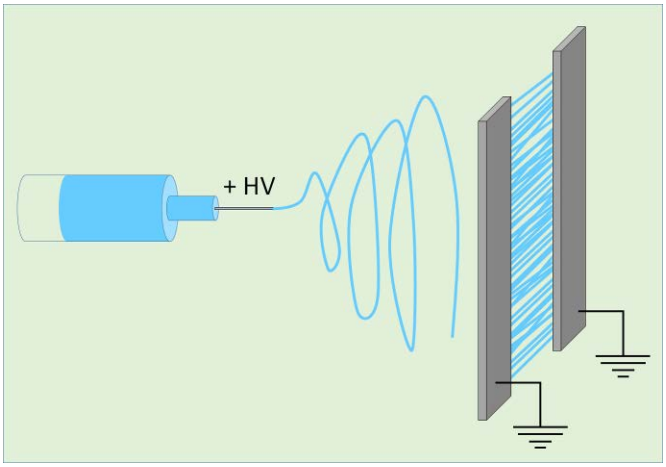

Figure 1.3 An electrospinning setup for collecting aligned nanofibers using parallel grounded plates

One of the emerging topics is specifically aimed to address organized clustering of fibers. Randomly oriented nanofibers are usually obtained by collecting fibers on a single piece of conductive substance. The fiber orientations were usually achieved by using specially designed collectors, such as a high-speed rotating cylinder, collector with tip-like edge or auxiliary electrode [109-112]. The parallel electrodes configuration, which is schematically shown in Figure 1.3, has the advantage of simple set-up, easy to obtain highly aligned fibers, and the capability of transferring the aligned fibers to another substrate [113]. In this setup, metal plates (e.g. aluminum) were grounded and positioned in parallel separated by a small gap (typically < 2cm) between them. The orientation of fibers was improved due to the opposite directions of electric field near the plates. When

the jet hits one electrodes, charges on the tip of the jet are neutralized and the electric force pulls the rest of the jet towards another plate. As a result, the charged fibers align perpendicular to the plates. The disadvantage is that there is a limit in the length of aligned fibers.

1.3.6 Dip-coating

Sol-gel/dip-coating is versatile in processing ceramic thin films of various compositions [49, 114]. It requires simple and low cost equipment compared with other methods of obtaining thin films such as vapor deposition, electron beam vaporation and sputtering [49, 114]. It also has the possibility of coating large areas [115]. In a dip-coating process, the substrate is normally withdrawn vertically from the solution at a constant speed. For thin films (e.g. thickness < 1μm) processed from Newtonian fluids, low withdrawal speeds are typically applied where the gravity force can be neglected. The stationary film thickness is determined by the withdrawing speed, viscosity and surface tension of the solution [49, 114]. Experimentally, it is convenient to control the thickness of the film processed from dip-coating by adjusting the withdrawal speed.

1.4 Objectives

A general methodology of processing ceramic thin films embedded with aligned nanorods needs to be developed. The objectives and specific tasks within the objectives are given as follows:

1. **The exploration of the sol-gel/electrospinning approach to generate ceramic nanofibers as potential fillers for the multifunctional thin films;**

Mullite fibers have been widely used as the reinforcement in ceramic matrix composites [116, 117]. These fibers are also used as the high temperature or electrical insulating materials [118, 119]. Mullite fibers have been produced for decades using the dry-spinning technology [105-107, 120120]. The diameters of the dry-spun fibers are generally about tens of micrometers. The precursors were often derived from aluminum alkoxide and tetraethyl orthosilicate (TEOS) [105, 106, 120]. The polymerization reaction was controlled via hydrolysis and condensation until the appropriate viscoelastic behavior was reached. In many applications, it is desirable to have fibers with small diameters and high surface areas. For instance, thin fibers are desired in sensing and catalyst applications. Owning to their high surface areas, the sensitivity and catalytic activity have been significantly improved [121, 122]. In structural ceramic composites, nanosized ceramic fibers in a ceramic matrix can lead to an improvement in the mechanical properties [123]. Hence nanofibers become especially important. The dry spinning technology is difficult to achieve sub-micrometer diameters. Electrospinning is a versatile processing tool for ceramic fibers, especially nanofibers [124, 125]. The experimental route of using sol-gel/electrospinning method towards mullite nanofibers will be explored in chapter 2. A novel, nondestructive method of testing micro and nanofibers by applying a magnetic torque on the free end of a suspended fiber is developed to examine the flexural rigidity of ceramic microfibers.

2. **The design of experimental protocol to fabricate ceramic nanofibers embedded with magnetic nanoparticles by in situ precipitation;**

Many research efforts have been made to fabricate nanocomposites with unique properties and multi-functionality enabled by the nanoscale microstructure [126-128]. Novel properties have been achieved with the ceramic-based nanocomposites of embedded metallic nanoparticles (NPs). Controlling the dispersion and the size distribution of the NPs is the key to achieve optimum performance and desired properties [129]. These nanocomposites can be achieved using thermal reduction, mechanical mixing, liquid phase deposition, chemical vapor deposition, laser deposition, or sol-gel method [81, 130-134]. The thermal reduction method is one of most commonly used ones, through which metal oxide precursors can be converted to dispersed metallic nanoparticles with a heat-treatment in the reducing atmosphere [82, 126]. Aerogels, films, fibers and powders are especially suitable for this method due to their low density, open porous structure, and high specific surface area that allow easy diffusion of reducing gases [126, 135, 136].

Transition metal NPs often have interesting properties and important applications in catalysts, sensors, magnetic, electronic and optical devices [82, 135, 136]. Nickel NPs are particularly important as catalytic, conductive and magnetic materials. Embedding Ni NPs into the ceramic matrix provides the magnetic functionality, which can be used for non-destructive evaluation (NDE) of the materials condition [137]. It has been demonstrated in many ceramic/metal nanocomposites systems such as the SiO_2/Ni, Al_2O_3/Ni, Y-TZP/Ni and ZrO_2/Ni [128, 135, 136, 138]. The thermal reduction method is one of the most convenient ways to introduce dispersed nickel NPs [128, 138, 139]. Reduction sintering of ceramics with additives of NiO or Ni^{2+} salts resulted in intragranular Ni NPs of sizes between 20 and 100 nm dispersed at the grain boundaries and within the

grains of an oxide host [128, 139]. The way to synthesize mullite-nickel nanocomposite fibers using electrospinning, followed by thermal reduction will be explored in chapter 3. The consequent properties and materials microstructures will be elaborated in detail.

3. **The fundamental understanding of the nanoparticle formation and its mechanical state at high temperatures;**

Synthesis and stabilization of metal nanoparticles of well-defined size has been one of the emerging themes of nanoparticle research. For example, high temperature stability of metal nanoparticles is the main issue in the field of catalysis and high power laser plasmonics [38, 39, 140, 141]. Over time, the metal NPs suffer degradation at high temperatures and, if embedded with ceramic materials, they are prone to aggregate and sinter [38-40]. Stabilizing metal nanoparticles at high temperatures within a ceramic host is highly desirable and should be fundamentally understood [142, 143].

The problem of interactions of elastic nuclei with an elastic matrix stands at the core of materials science and solid mechanics [144-147]. The seminal works by Eshelby [144] put this problem at the forefront of materials science and mechanics and the appreciation of its importance is raised with the progress of nanotechnology offering different ways of making metal/ceramic, metal/metal or ceramic/ceramic nanocomposites. An important example is the analysis of stresses caused by the lattice mismatch in nanoparticles-quantum dots embedded in a matrix. These spontaneous stresses are of particular significance as the means to tailor the band-gap structures of the quantum dots in heterostructures of the electronic devices [145]. With the recent nanotechnology developments, especially in semiconductor industry, it becomes clear that the interface

separating the nanoparticle from the matrix significantly influences the stress field inside and outside the inclusion [144-147].

However, the theories overlooked the size dependence of the transformation strain. To fundamentally understand the process, theoretical analysis and experimental study of the misfit elastic strain of the Ni NP precipitated from a mullite fiber matrix is performed in chapter 4. The transformation strain is presumed caused by the volume dilatation from the matrix.

4. Design of experimental procedure to fabricate defect-free ceramic coatings

The sol-gel process is a versatile technique in processing low dimensional glass and ceramic materials such as fibers and coatings. In the coating process, the condensation during drying and decomposition upon heat-treatment can greatly affect film formation. The capillary and coherent forces during these processes are the driving forces for densification of films. On the other hand, the intrinsic stress caused by the shrinkage, if exceeds the material's limit, results in uncontrollable cracking and decohesion. It is difficult to prevent cracking due to the stress, especially for thick films [47, 48, 148]. The maximum film thickness of non-repetitive deposition above which the cracking occurs is often termed as "critical thickness" (τc). For sol-gel derived ceramic films, the τc value is typically below 100 nm [49, 50]. Many attempts have been made to increase the critical thickness, such as using additives with chelating ligands (*e.g.* acetylacetone), or high molecular weight solvents and/or organic polymers [149-153]. The polymers are soft and more ductile than ceramics. Such polymers as polyethylene glycol and polyvinylpyrrolidone (PVP), were used as the additives to prevent cracking [153, 154].

They were demonstrated to be effective for stress relaxation during heat-treatment in sol-gel film studies [148, 154].

It is often desirable to have the dense, crack-free, thick and coherent mullite coating for corrosion protection. There are many reports on the preparation of mullite coatings using the sol-gel method [155-158]. However, in these reports, mullite coatings were usually obtained from diphasic precursors [155-158]. For instance, mullite coatings can be synthesized from a colloidal precursor using boehmite and Tetraethyl orthosilicate (TEOS) as the starting materials [155]. Polymers and chelating agents were added to suppress the condensation reaction which gave rise to a high τ_c value of above 1 μm [155]. The intermediate phase, such as the Al-Si spinel, was observed [155]. The high temperature heat-treatment at above 1400°C is usually required to obtain the mullite phase, once the intermediate spinel phase was formed. Due to the high temperature sintering, abnormal grain growth often occurred, resulting in substantially large grains [155]. In other reports, aluminum nitrates (AN) and TEOS were used to process the sol-gel precursors for mullite coatings [156-158]. In those works, the mullite phase was achieved at or above 1200°C due to the diphasic precursors, and adding polymer modifiers did not change the di-phasic nature of the precursors. [156-158].

A monophasic precursor has the advantage of low processing temperature and excellent single phase purity. It is interesting for ceramists to understand the low temperature processing of dense crack-free mullite coating, using the monophasic precursor with the addition of polymers as structural modifiers. In chapter 5, the role of polymer additives as the sol-gel structure modifier is explored for the coating process.

5. **The general strategies for making macroscopic ceramic thin films embedded with nanorods.**

Ceramic fibers with submicron diameters, including short fibers such as whiskers and rods, exhibit superior physical and chemical properties. They are chosen as a platform for multifunctional, hierarchically organized nanocomposites [2, 5, 159-161]. Aligning submicrometer ceramic fibers is one of the state-of-art technologies for advanced nanocomposites [13, 162-164]. Particularly, we present two promising methods to process ceramic thin film nanocomposites: the magnetic assembly and electrospinning. The magnetic field assisted assembly of nanorods demonstrates intrinsic advantages in processing thin films composites with oriented magnetic nanorods. In a drying or solidifying polymer film, short nanorods or whiskers can be well aligned [87]. The strategy for nanorod alignment in macroscopic materials has also been developed recently [23]. Electrospinning enables fabrication of extensive variety of ceramic and composite fibers of small diameters [103, 108, 165-167]. Although the strategies for alignment have been developed in the literature, integration of ceramic films or bulk composites with embedded electrospun nanofibers while retaining the ordering structure remains challenging [165, 166]. Processing ceramic thin film composite from the magnetic field assembly and electrospinning method is explored in chapter 6.

6. **The fundamental understanding of the ceramic thin films formation on substrates with nanorods or nanofibers;**

Integrating pre-aligned submicrometer ceramic fibers into thin ceramic films has broad technological implications. Fundamentally understanding the sol-gel thin film

formation with submicrometer fibers offers perceptive knowledge in engineering novel ceramic composites. With the formation of a thin solid film, the submicron short fibers were confined in the plane of the substrate with retained orientations. On the other hand, presence of submicron fibers affects the local equilibrium where the gel film conforms on the fiber inclusions. This could initiate microscopic cracks at the interfaces [168]. However, fundamental studies on the detailed mechanism were not carried out. Detailed investigations should be given to understand the topographic evolution of sol-gel composite thin film and the cracking problem with the fiber inclusions.

Researchers have been investigating the micrometer thick film formation on substrates with features in micrometer scale, such as holes, trenches or wedges [52-58]. The thickness evolution was determined by flow of liquids over topography. Introducing surface tension as a driving mechanism into standard lubrication theory for thin Newtonian fluid layer leads to a fourth order nonlinear equations [52-58169]. Furthermore, extended investigations were carried out to understand the effect of solvent concentration profiles, composition-dependent viscosity, fluid inertia and viscoelasticity, Marangoni stress and gravity-driven cases [170-173]. There are only a few cases that static equilibrium can be reached [55, 174]. For example, in spin-film, equilibrium profile was reached when centrifugal and capillary forces are exactly balanced [55, 174]. For the cases that capillary force is non-balanced, the thickness profile is dominated by the kinetics of evaporation, liquid transportation and time-dependent viscosities. Without external body forces, driving force for planarization of the film always exists in order to minimize the curvature of the meniscus.

The fundamental studies on nanoscale thin film formation with nanorods were not carried out. The film thickness evolution with nanorods and formation and microscopic cracks are investigated both experimentally and theoretically.

CHAPTER II

DEVELOPMENT OF THE ELECTROSTATIC SPINNING OF FIBERS AS POSSIBLE CANDIDATES FOR FILLERS IN CERAMIC COMPOSITE THIN FILMS

2.1 Introduction

2.1.1 Synthesis of mullite fibers by sol-gel/electrospinning

In this chapter, we present the method of synthesizing mullite fibers with controlled morphologies using the sol-gel/electrospinning method. Mullite fibers have been produced for decades using dry-spin technology [105-107]. However, the diameters of the dry-spun fibers are generally about tens of micrometers. In many applications, it is desirable to have fibers with small diameters and high surface areas. For instance, thin fibers are desired in sensing and catalyst applications. Owning to their high surface areas, the sensitivity and catalytic activity have been significantly improved [121, 122]. In structural ceramic composites, nanosized ceramic fibers in a ceramic matrix can lead to an improvement in the mechanical properties [123]. Hence nanofibers become especially important.

Electrospinning is a versatile processing tool for ceramic fibers, especially nanofibers [124, 125]. There are only a few successful attempts in processing mullite nanofibers by electrospinning [175-177]. The mullite nanofibers have been fabricated by electrospinning of AIP, AN and TEOS directly mixed with polymer additives, such as polyvinylpyrrolidone (PVP), polyvinyl butyral (PVB) or polyvinyl alcohol (PVA) [175-177]. A high concentration of polymer, normally 5% to 8% in the precursor was required for electrospinning [175-177]. Reducing the polymer content is desired as it increases the ceramic yield, leading to a smaller shrinkage of the material during heat treatment. We

present an approach for electrospinning of mullite fibers which only requires a small concentration of polymer spinning aid of less than 0.3%.

Controlling fiber diameter and its uniformity is an imperative process of electrospinning. The control is usually approached by adjusting the viscosity of the electrospinning solution. The viscosity of the solution is conveniently tuned by changing the solute concentration. Therefore the concentration-dependent viscosity shall be measured to fully appreciate the effect of the solution viscosity on the materials' microstructure. Other processing parameters, including the solution feeding rate, distance between the electrodes, applied voltage and relative humidity should be meticulously controlled. A few groups of trial experiments were carried out in the first step to find the appropriate those processing parameters for electrospinning. A practical method is to fix a moderate feeding rate (e.g. 0.5ml/h) and distance between electrodes (e.g. 20cm), then gradually increase the applied voltage until the formation of stable jets without significant breakage. Then those parameters are finely adjusted around the trial ones to further stabilize the jets and maintain the uniformity of materials on the collectors.

2.1.2 Mechanical characterization of ceramic fibers obtained from electrospinning

Mechanical characterization of ceramic fibers obtained from electrospinning is a difficult task. Due to the difficulties in handling nano- and microscale fibers obtained from electrospinning and measuring small load required for deformation, reports on measuring mechanical properties of the electrospun ceramic fibers can rarely be found. Due to its brittleness, ceramic fiber readily suffers mechanical failure even at small deformations. This makes it very difficult to handle the fibers without damaging them [178, 179]. To

avoid this problem, the tensile test is typically conducted on a thick ceramic fiber, with a diameter greater than tens of micrometers [180]. Due to these difficulties, microfibers are typically tested in strands composed of many individual fibers [181, 182] and then different mathematical models have been employed to interpret the data [183]. Recently, some other approaches have been successfully developed such as a modified tensile test, atomic force microscopy, microcantilever vibration methods, beam bending methods and the nanoindentation method [184-187]. Among these approaches, the fiber bending method assumes the simplest experimental setup [187, 188]. It is instructive to investigate the flexural rigidity of microfibers by examining their shape and comparing it with the Bernoulli-Euler or Timoshenko predictions. This experimental setup, as schematically shown in figure 2.1, utilizes small magnetic forces to deform a fiber attached with a magnetic tip [189]. From the stationary bending profile of the fiber, elastic constant of the fiber can be calculated.

2.2 Experimental Procedure

2.2.1 Materials processing

Aluminum isopropoxide (AIP, $Al(C_3H_7O)_3$, 98%,), aluminum nitrate (AN, $Al(NO_3)_3 \cdot 9H_2O$, 98%, Alfa Aesar, MA, USA) and tetraethyl orthosilicate (TEOS, $Si(OC_2H_5)_4$, 98%, Acros Organics, NJ, USA) were used to synthesize the precursor. The precursor compositions are given in Table 2.1. Water was used as the solvent. For each batch, the total concentration of AIP and AN were kept at 0.6 mole. AN was dissolved in deionized water at room temperature by vigorously stirring it for 30 min. Then AIP and TEOS were added into the solution and stirred for 20 hours. AIP and TEOS were dissolved

completely, and clear solutions were obtained. Each solution was then refluxed at 80°C for 5 hours. Approximately 2/3 part of the solvent was removed using a rotary evaporator (IKA RV 10 digital, IKA, China). The obtained solutions were then set in an oven at 80°C until viscous sols were formed. The spinnability of these sols was determined using hand-drawing with a glass rod.

A polyethylene oxide (PEO, MW 1,000,000, Aldrich, MO, USA) solution of 2 wt% in H_2O was prepared separately as the spinning aid solutions. Sol MS7 from Table 2.1 was diluted in ethanol, and then mixed with small amount of PEO solution. These solutions were ready for electrospinning, and are called 'E-sol' in Table 2.2. The volume ratios between the initial mullite precursor, PEO solution, and ethanol are given in Table 2.2. The calculated mullite yields and PEO concentrations with respect to the E-sol volume are also given in Table 2.2.

Table 2.1. The initial precusor compositions

Sol code	AIP (mol)	AN (mol)	TEOS (mol)	H_2O (mol)
MS1	0.3	0.3	0.2	10
MS2	0.35	0.25	0.2	10
MS3	0.36	0.24	0.2	10
MS4	0.38	0.22	0.2	10
MS5	0.4	0.2	0.2	10
MS6	0.42	0.18	0.2	10
MS7	0.44	0.16	0.2	10
MS8	0.45	0.15	0.2	10
MS9	0.5	0.1	0.2	10

Table 2.2. The electrospinning sol compositions. 'M:P:E' means volume ratios between initial mullite sol, PEO solution, and ethanol.

E-sol code	M:P:E (volume ratio)	Calculated mullite yield (grams per 100 mL E-sol)	PEO concentration (grams per 100 mL E-sol)
E-1	4:1:0.5	32	0.27
E-2	4:1:2	28	0.23
E-3	4:1:4	24	0.20
E-4	4:1:8	18	0.15
E-5	4:1:12	14	0.12
E-6	4:1:16	12	0.10
E-7	4:1:20	10	0.09
E-8	4:2:22	9.4	0.16
E-9	4:2:26	8.3	0.14
E-10	4:2:30	7.5	0.13
E-11	4:2:34	6.8	0.11
E-12	4:2:40	6.0	0.10

The fibers were electrospun under an applied electrical field generated using a high voltage supply (Model PS/FC60P02.0-11, Glassman High Voltage Inc, NJ, USA). A positive voltage of 10kV was applied to the needle of the syringe containing e-spun solutions driven by a syringe pump (Model NE-300, New Era Pump System Inc, NY, USA). The flow rate was set to the vicinity of 0.5 ml/h. The needle was placed 20 cm apart from the collector. The fibers were produced at 25 - 35% ambient relative humidity and collected using a rotating collector. The rotating collector has four grounded stainless steel bars, with a gap of ~10 cm between each pair of adjacent bars. The fibers were then cut from the collector and collected in the form of mats. The obtained fibers were dried at 60°C for 24 hours before firing. The heating rate was set at 1°C/min below 500°C and 10°C/min above 500°C. The fibers were fired at 1000°C, 1200°C, or 1400°C for 2 hours.

2.2.2 Characterization

The viscosity of sols was measured using a viscometer (Viscolead ADV, Fungilab Inc, NY, USA) at room temperature. The thermal characteristics were studied at different heating rate under flowing air condition using DTA (DTA7, Perkin Elmer, Waltham, MA, USA), and TGA (TGA7, Perkin Elmer, Waltham, MA, USA). The materials microstructure was characterized using X-ray diffraction (XRD, Rigaku Co., Ltd., Tokyo, Japan) and scanning electron microscopy (SEM, Hitachi S4800**,** Hitachi, Ltd., Tokyo, Japan). The average size of fiber diameters of the as-spun and fired fibers was calculated from more than 100 randomly selected fibers taken from SEM micrographs.

The single filament tensile tests were carried out using a single filament tensile testing machine (Instron 5582, Instron Ltd., High Wycombe, Buckinghamshire, UK). During each test, a single mullite fiber was mounted and fixed using superglue or tape onto a C-card. After mounted on the test machine, the C-card's neck was cut open. The strain rate is set as 1mm/min. Two gauge lengths (5mm and 10mm) were used. The fiber diameters for each test were measured using optical microscope (Olympus BX51, Olympus Optical Co. Ltd, Tokyo, Japan).

For the fiber bending test, a single 1 mm long fiber was glued to the glass substrate at one end. The iron fillers (FerroTec, Santa Clara, CA) were mixed with the superglue with a 1:1 weight ratio. The fiber tip was immersed into the liquid and then the fiber was pulled out. The residue droplet was dried in ambient atmosphere to form a magnetic tip. This magnetic glue was sufficiently thick to solidify before slipping off of the fiber tip. Magnetic moments of the deposited droplets were measured by using an Alternating Gradient Magnetometer (AGM 2900, Princeton Measurements Inc., NJ, USA). Once the

applied magnetic field is known, one can calculate the applied force. To control the magnetic force in the bending experiment, a cone shaped magnet (SuperMagnetMan, 12.7 * 12.7 mm, N50 grade) was placed on a movable stage as shown in Figure 2.1. The central axis of the magnet was aligned along the z axis. Moving the magnet back and forth, one can force the suspended fiber to bow. The process of the fiber bowing was filmed with a camera and then the images were analyzed with the developed code. The magnetic force was calculated from the simulated magnetic field according to the method of Ref [188].

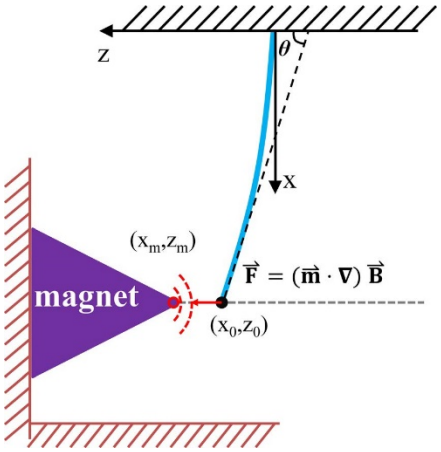

Figure 2.1. Specimen configuration of bending test using magnetic force [189]

2.3 Results

Table 2.3 summarizes the appearance mullite precursor after mixing and condensation. The pH value and spinnability after condensation are also given in Table 2.3. A viscous sol was obtained from sol MS5, MS6, MS7, MS8 and MS9 respectively without apparent phase separation. The viscosity changes with time of the mullite precursors are shown in Figure 2.2. In general, sols MS5 and MS7 had relative mild slopes in the late stage of polymerization, especially when the viscosities were greater than 100 poises. Sols MS8 and MS9 showed steep increase of viscosity with time. In the sol-gel process, the sol

viscosity can be greatly affected by a small change in the processing conditions, such as initial concentration, pH value, and setting temperature. Sometimes the 'relative time' is used to compare the polymerization behaviors [190]. Relative time is defined as t/t_g, where t is the real time and t_g is the total gelation time when the sol becomes the solid gel. Figure 2.2 (b) shows the viscosity change vs. relative time when the viscosity was above 100 poises. At this stage, the viscosity increased drastically. Sols MS8 and MS9 showed narrow viscosity-time windows for processing at the final stage of gelation compared with sols MS5 and MS7. Thus sol MS7 was selected for fabrication of electrospinning precursors. All the mullite fibers obtained in this chapter were from sol MS7.

Table 2.3. The appearances of mullite initial precursor before and after condensation. The pH value and spinnability after condensation are also given in this table. The spinnability is determined using the hand drawing method.

Sol code	Sol appearance		pH value	Spinnable
	before condensation	after condensation		
MS1	white precipitation, opaque	opaque and precipitation	1.28	No
MS2	silver-gray and clear	opaque and precipitation	1.62	No
MS3	colorless and clear	opaque and precipitation	1.69	No
MS4	colorless and clear	opaque and precipitation	1.90	No
MS5	colorless and clear	colorless and clear	2.32	Yes
MS6	colorless and clear	colorless and clear	2.77	Yes
MS7	colorless and clear	colorless and clear	2.88	Yes
MS8	lightly gray and clear	Silver-gray and clear	2.89	Yes
MS9	lightly gray and clear	Silver-gray and clear	3.13	Yes

The initial precursors were too viscous for e-spinning. Therefore, mullite sols were diluted with ethanol and PEO solutions. Figure 2.3 shows the viscosity of modified

precursors (E-sols) at different shear rate. All E-sols exhibited shear-thinning behavior. With increasing ethanol content, the viscosity decreased gradually.

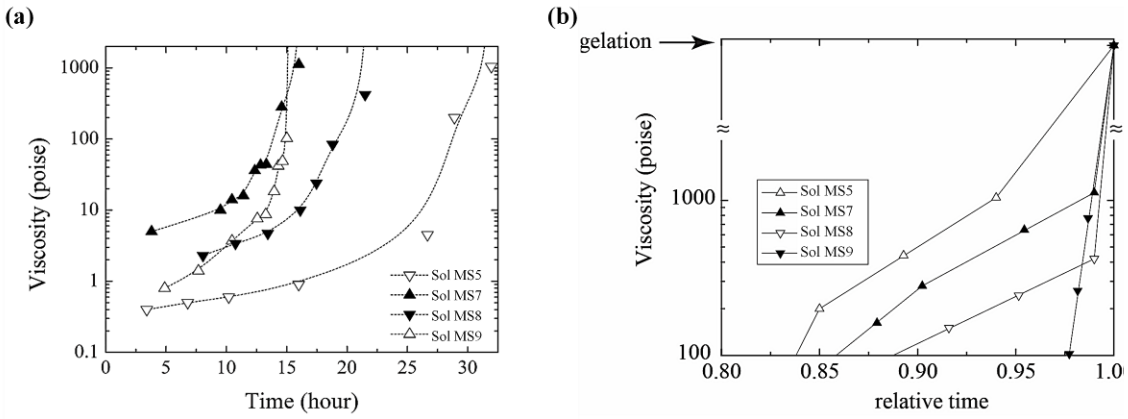

Figure 2.2 Viscosities of sol MS5, MS7, MS8, and MS9 vs. polymerization time. (a) vs. real time and (b) vs. relative time.

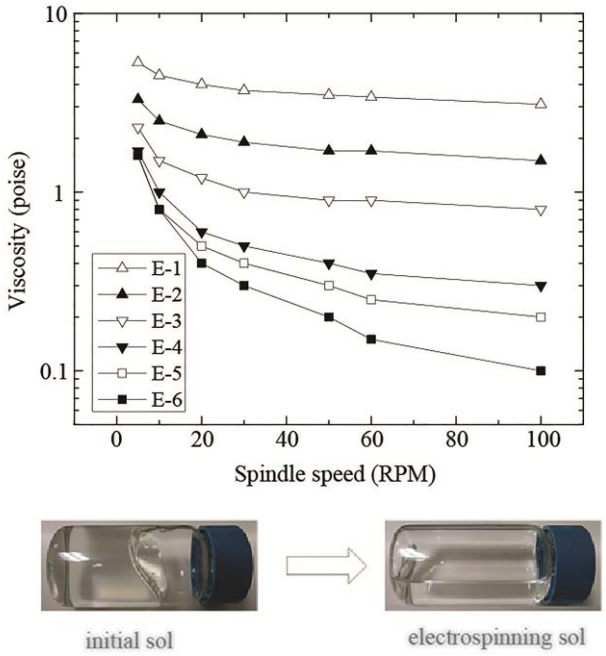

Figure 2.3 Viscosities of diluted precursors versus shear rate. The bottom pictures show the effect of the dilution.

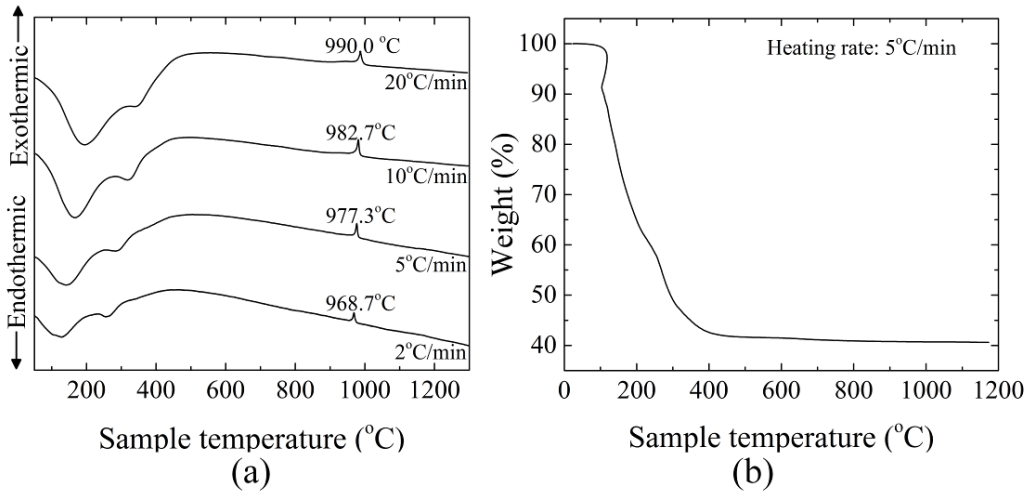

Figure 2.4. DTA (a) and TGA (b) traces of mullite sol

In the DTA traces, shown in Figure 2.4 (a), the endothermic peaks at 100-200°C were attributed to the evaporation of absorbed solvent and low molecular weight organics [191]. The endothermic peak at 300 - 400°C was due to the decomposition of polymer chains [191]. The exothermic peak at around 1000°C corresponded to the crystallization of mullite phase. These peaks are consistent with other reports [107, 191]. With increasing heating rate, the exothermic peaks shifted to the higher temperatures. The TGA result (Figure 2.4 (b)) was consistent with the DTA results. With a heating rate of 5°C/min, the significant weight loss occurred at 100 - 400°C. There was no significant weight loss at above 500°C, indicating the completion of organic decomposition.

The XRD results on the mullite sol after heat-treatment at 800°C, 1000°C and 1200°C was shown in Figure 2.5. The labeled peaks indicate the well-defined pure mullite phase without spinel phase. In the sol-gel processing, elimination of the spinel formation is challenging and important [192-194].

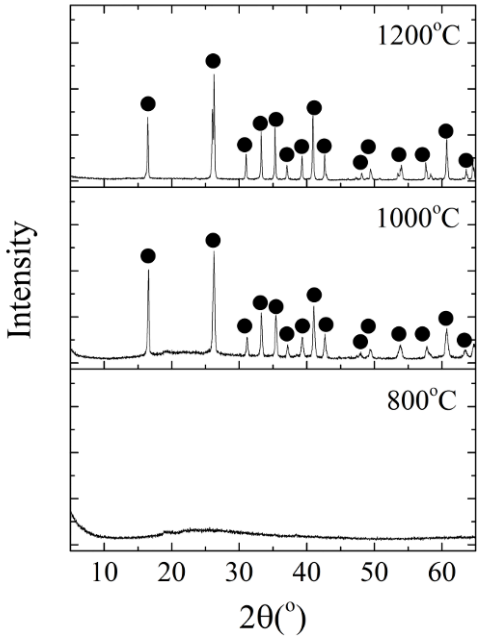

Figure 2.5. XRD trace of mullite powder after calcination at 800°C 1000°C and 1200°C for 2 hours (mullite ●).

The obtained mullite fiber microstructure are summarized in Table 2.4. Except E-12, the rest of the E-sols were spinnable. Only beads were obtained without fiber from E-12. The SEM micrographs of electrospun fibers are shown in Figure 2.6. Mullite fibers with diameters from 500 nm to 15 μm were obtained from the solutions with the compositions described in Table 2.4. Figure 2.6 shows some of the electrospun fibers. The fibers in Figure 2.6 (a) to (e) showed uniform microstructure. The surfaces of the fibers were smooth. With the increasing ethanol content up to 81 vol%, the diameter of the fiber gradually decreased to about 500 nm. Further increasing the ethanol content, we were unable to obtain uniform fibers. The beads appeared and the fiber diameters became uneven, as shown in Figure 2.6 (f) to (g). When the viscosity was too low, only beads were collected (Figure 2.6 (h)).

Table 2.4. Summary of microstructural characteristics of electrospun mullite fibers

Sol code	Average diameter of as-spun fibers (μm)	Average diameter of mullite fibers after firing (μm)	Coefficient of variation	Fiber appearance
E-1	17	12.24	0.167	uniform
E-2	6.0	4.65	0.079	uniform
E-3	4.5	3.53	0.141	uniform
E-4	3.0	1.50	0.123	uniform
E-5	1.5	0.95	0.147	uniform
E-6	0.9	0.77	0.115	uniform
E-7	0.5	0.32	0.130	uniform
E-8	1.2	0.87	0.144	uniform
E-9	0.8	0.68	0.121	uniform
E-10	0.6	0.41	0.262	uniform with a few beads
E-11	0.5	~0.4	NA	nonuniform with beads
E-12	-	-		only beads

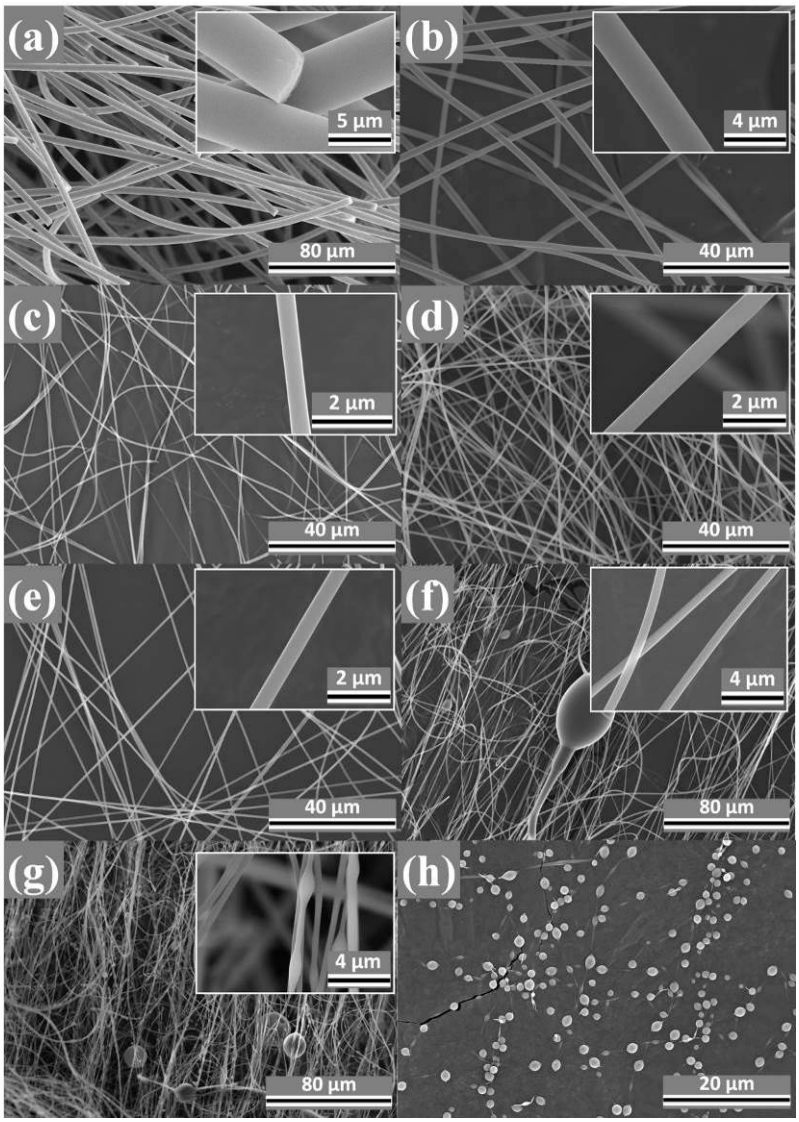

Figure 2.6. Microstructure of electrospun green fibers obtained from. (a) E-3; (b) E-4; (c) E-6; (d) E-7; (e) E-9; (f) E-10; (g) E-11; and (h) E-12.

The mullite fibers fired at 1200°C for 2 h are shown in Figure 2.7. The calcined fibers did not fuse with each other. There were no cracks or pores observed on the fiber surface and cross-sections. The surfaces of the heat-treated fibers exhibited tiny grains and thus were rougher than the as-spun fiber surfaces. This feature was caused by the mullite

grain growth. The fiber diameters can be achieved from above 10 μm to about 400 nm. Figure 2.7 (a) shows the largest diameter, which is about 12 μm. Figure 2.7 (b) - (e) show the mullite fibers with different diameters obtained from E-sols in Table 2.4. The thinnest mullite fiber obtained in our study was about 400 nm in diameter. In general, the obtained mullite fibers have narrow diameter distribution for each batch, not including the fibers obtained from E-10 and E-11. Those fibers have uneven fiber diameters as spun. Figure 2.8 shows the diameter distribution of mullite microfibers obtained from E-3. These fibers were selected for mechanical test, because the fiber diameter of ~3μm is about the limit for our tensile test machine. We were not able to test smaller diameter fibers.

A. Tensile test

There were two mounting methods used to fix the fibers on the C-cards. We use superglue or tapes to fix the fibers on the C-cards. When superglue was used to fix the two ends, the fiber was not able to slide during the test. This is because after superglue was cured, it completely became solid. When the tape was used, the fiber can slip during the test. If the fiber did not slide during stressing, the modulus measurement was accurate. The tape mounting did not generate any meaningful modulus values, but the measured tensile strengths were accurate. The success rate for the 5 mm gauge length measurement was extremely low (less than 10%) if superglue was used. Most of the fibers were broken at the superglue contact spots rather than in the middle of the fibers. The mechanical properties of the mullite fibers were summarized in Table 2.5. The result values were obtained based on at least 20 successful measurements. The 5 mm gauge length test was done using the tape to mount the fibers. The average tensile strengths of the mullite fibers were about 1.46

GPa for 5mm gauge length, and 1.25 GPa for 1 cm gauge length. An average elastic modulus of about 100.02 GPa was determined when superglue was used to mount the fiber.

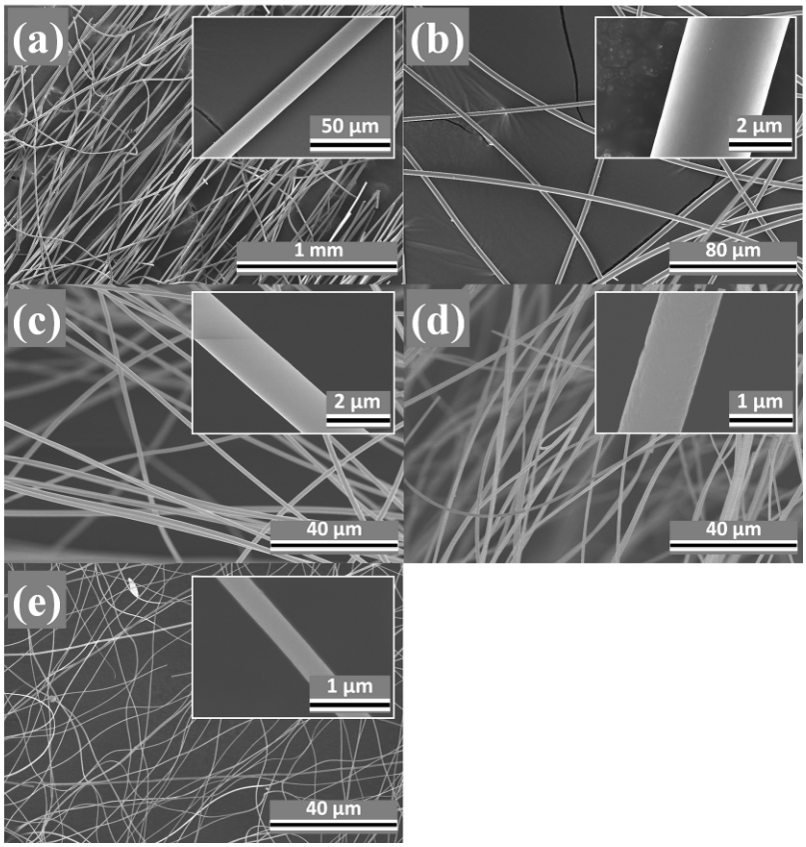

Figure 2.7. SEM images of mullite fibers after calcination at 1200°C for 2 h. (a) thick fibers with diameter (d) > 10 µm; (b) and (c) microfibers with 1 < d <5 µm; (d) sub-micro fibers with d ~ 800 nm; and (e) nanofiber with d ~ 300 nm.

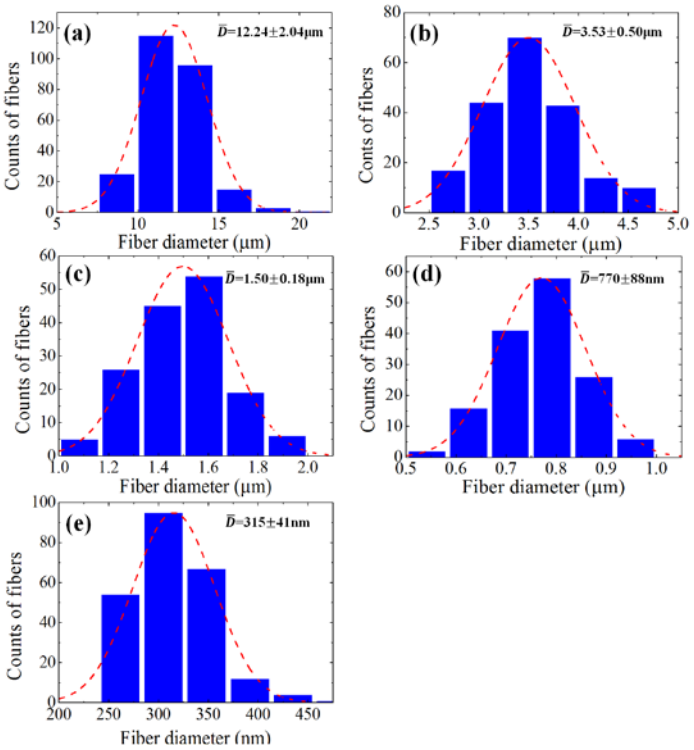

Figure 2.8. Statistical diameter distribution of mullite fibers in Figure 2.7 (a)-(e). The distribution was fitted by normal function (dashed line).

Table 2.5. Average tensile strength, elastic modulus measured at different gauge length. The result values were obtained based on at least 20 successful measurements.

Gauge length	Average tensile strength (GPa)	Elastic modulus (GPa)
10 mm	1.25	96 -104
5 mm	1.46	NA

B. Bending test

A series of snapshots taken during the bending test are shown in Figure 2.9. The fiber had a length of 0.64 mm (measured from the fixed-end to the free-end) and diameter of 4.5 μm. The fiber started to flex to the left in frame 1 and continued to bow with increasing deflection when the magnet was approaching the fiber. As shown above, the torque on the tip was negligible and the fiber bent because of the field gradient. The

magnitudes of forces exerted onto the fiber tip as well as the tip coordinates are summarized in Table 2.6. The change of the x coordinate is initially small, i.e. the tip moves almost along the z - axis. A noticeable displacement of the fiber tip from the magnet axis can be seen in frames 7-9. The angle of the force vector in Table 2.6 was calculated from the magnetic field distribution as discussed in Ref. [188].

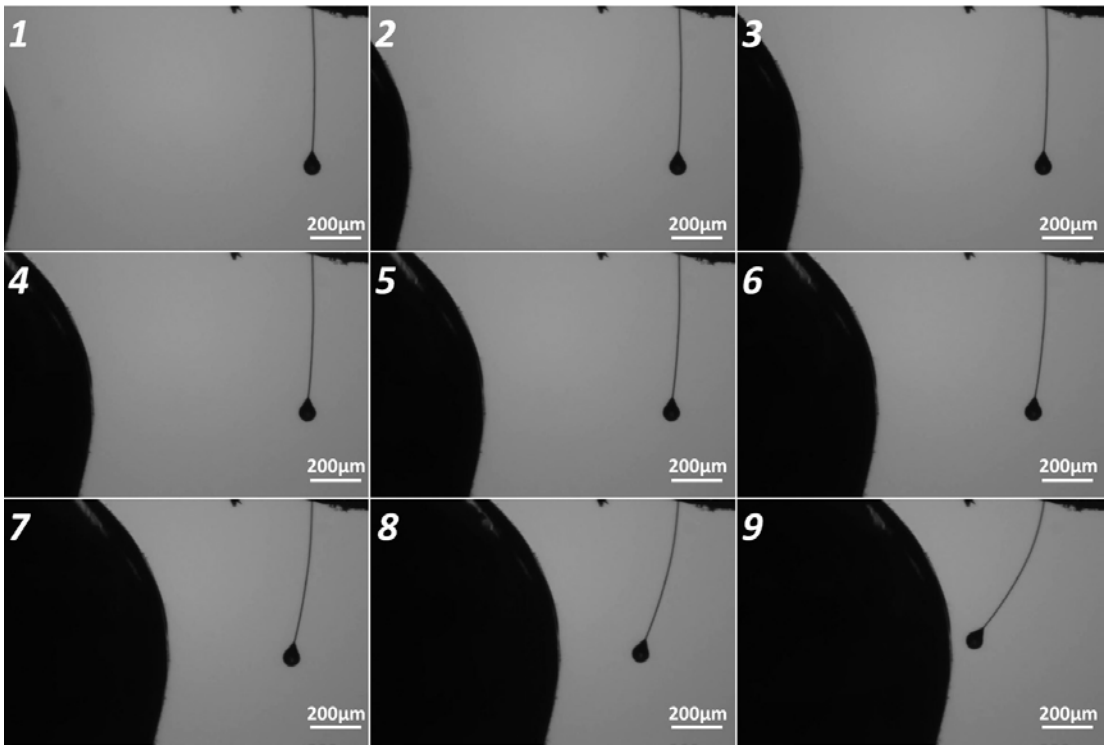

Figure. 2.9. Fiber bending by magnetic field.

Table 2.6. Force-position data of the fiber tip (the force direction is defined as the angle inclined by the force vector and x-axis shown in figure 2.1).

Frame number	Force magnitude (μN)	Force direction (°)	Tip coordinate z_0 (mm)	Tip coordinate x_0 (mm)
1	0.675	90.0	0.019	0.640
2	0.789	90.0	0.027	0.640
3	0.918	90.0	0.032	0.640
4	1.088	90.0	0.038	0.640
5	1.304	90.0	0.048	0.640
6	1.641	90.0	0.070	0.640
7	2.139	89.8	0.100	0.636
8	3.198	88.9	0.172	0.618
9	6.369	86.3	0.300	0.565

After bending, the fibers took on their original configuration, parallel to the vertical axis. This fact suggests that the stresses have been completely relaxed and the fibers have not acquired any irreversible or plastic deformations. Taking into account the complete recovery of the fiber shape after deformations, it is natural to assume that the material is purely elastic. Moreover, we will use the Euler elastica model that neglects any shear deformations in the material [195]:

$$IE\frac{d^2\theta}{dl^2} - Fsin\theta = 0 \tag{2.1}$$

where E is the elastic modulus; I is the second moment of inertia; l is the arclength, $0<l<L$, where L is the fiber length; θ is the angle formed by the tangential line at the point with arclength l with the z-axis; F is the applied magnetic force. For a fiber with the circular cross-section, the second moment of inertia is $I = \pi d^4/64$, where d is the fiber diameter [195]. Since the x-component of the magnetic force is much smaller than the axial z-component, the problem is simplified by assuming that the force F acts only in the z-direction. The weight of the droplet is also negligible. From the dimension of the droplet shown in figure 2.9 we estimated the gravitational force on the order of 10^{-9} N. The

magnetic forces employed are in the micronewton range which is at least two orders of magnitude greater than the weight of the droplet. We impose the following boundary conditions to solve Eq. (2.1):

$$\begin{cases} \theta = \frac{\pi}{2} & at\ l = 0 \\ \frac{d\theta}{dl} = 0 & at\ l = L \end{cases} \tag{2.2}$$

With the known *I* and *F* parameters, one can reproduce the fiber profiles and compare them with the experimental ones. However, since the elastic modulus *E* was not known in advance, we needed to run a series of experiments adjusting E in order to fit the fiber bows.

In order to determine elastic modulus E, we numerically solved the Euler elastica equation with the specified boundary conditions. A comparison of the experimental and theoretical fiber profiles was done at a sequence of points (x_i,z_i) (i=1,2…N) shown in Figure 2.10. A *Matlab* program allows one to determine elastic modulus, *E*, corresponding to the best fit of the experimental and theoretical fiber profiles. Figure 2.10 collects the results of numeric fit of the fiber profiles given in frames 2-8 of Figure 2.9. The solid curves correspond to the theoretical fiber profile according to the numerical Euler elastica solution. The solid symbols correspond to the experimental data points. It is evident that the Euler elastica model describes the fiber profiles fairly well. The extracted elastic modules are summarized in Table 2.7. An average value of E = 104.8 ± 5.7 GPa was obtained from frames 2-6 in Figure 4.8 when the fiber tip was not moving far away from the magnet axis.

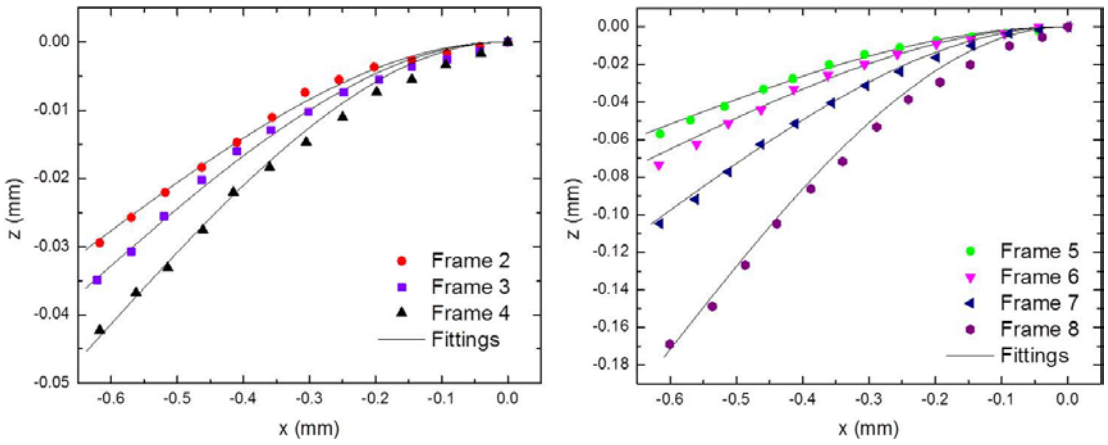

Figure 2.10. Numerical solutions of the Euler elastica model over imposed on the experimental fiber profiles represented by the solid symbols.

Table 2.7. Elastic modulus (*E*) and Flexural rigidity (*EI*) obtained by fitting the fiber bows with numerical solutions of the Euler elastica (2nd column) and by analyzing the movement of the fiber tip using eq. (7) (3rd column)

Frame number	Elastic modulus from full Euler elastica (GPa)	Elastic modulus from Eqs. (7) (GPa)	Flexural rigidity *EI* from Eqs. (7) 10^{-12} Pa m^4)
2	106	109	2.19
3	112	107	2.15
4	108	107	2.15
5	100	102	2.05
6	98	88	1.77
7	84*	80*	1.61
8	74*	70*	1.41

In order to verify the obtained results, we applied another method developed in Ref. [188]. This method takes advantage of the analytical solution of the Euler-elastica model [195]:

$$\begin{cases} z_0 = \sqrt{\frac{EI}{2F}}B(\theta_0), B(\theta_0) = \int_{\theta_0}^{\pi/2} \frac{cos\theta}{\sqrt{cos\theta_0 - cos\theta}} d\theta \\ x_0 = \sqrt{\frac{2EI}{F}} cos\theta_0 \end{cases} \quad (2.3)$$

where θ_0 is the angle formed by the tangential line at the fiber tip and the z-axis. For fiber configurations having $\cos\theta_0 < 0.5$, the analytical solution (4.3) can be approximated by polynomial functions to give useful relations between the applied force and coordinates of the fiber tip [188]:

$$\begin{cases} F \approx 3.19EI\, z_0/L^3 \\ x_0 \approx L - 0.615\, z_0^2/L \end{cases} \tag{2.4}$$

Since the *x* coordinate of the fiber tip does not change significantly in frames 2-5, we therefore used frames 2-5 to specify z_0 and calculate the force and then extract elastic modulus solving Eq. (2.4) for *E*. Figure 2.11 presents the obtained values of the applied force as a function of the tip position z_0. All available data points fall onto a straight line such that $E = 103.1 \pm 3.4$ GPa for the given series of fibers. This value of elastic modulus is in good agreement with results obtained by fitting the fiber bows with the Euler elastic profiles. Solving the Euler elastica model and attempting to fit the fiber bow by adjusting the *E* values, one observes that the modulus drastically decreases when the deformations become significant and the fiber tip moves away from the magnet axis. This non-physical behavior can be taken as an indication of the importance of the x-component of magnetic force within this range of deformations.

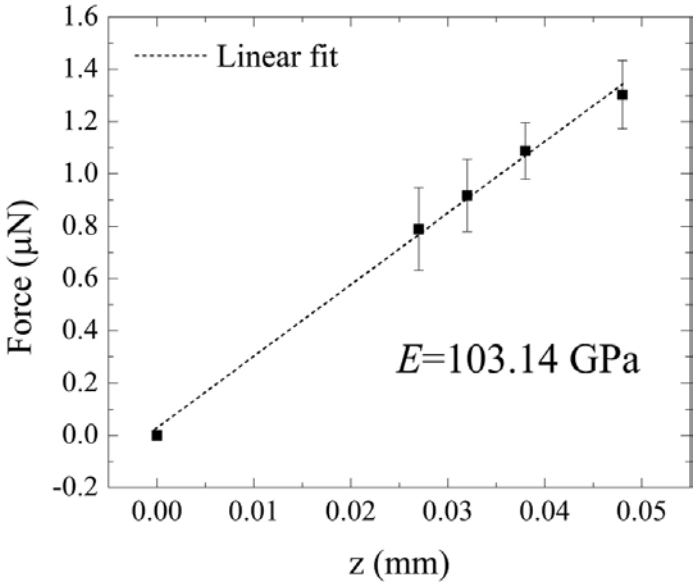

Figure 2.11. Applied magnetic force as a function of the fiber tip position z_0. The error bars come from the uncertainty of the determination of the fiber tip position disturbed by the attached droplet.

2.4 Discussion

The precursors for E-spinning of ceramics are usually characterized as co-precipitation (PPT) and sol-gel precursors [103]. Sol-gel precursors differ from PPT precursors as it involves sol-gel reaction with strict control of polymerization process proceeded by hydrolysis and condensation reactions. The precursors with certain spinnability can be derived from the sol-gel process [105-107, 120, 190, 191]. The combination of electrospinning with sol-gel processing is feasible to obtain ceramic fibers from this approach as it may require less spin-aid to form fibers with desired microstructures [108]. We control the hydrolysis process in the beginning, so that the mullite sol itself was spinnable. The good spinnability was attributed to the increased viscosity in sols containing linear polymers [107, 191]. We can e-spin diluted sol without adding any PEO. However adding PEO does improve the fiber uniformity. For such application, high content of PEO is not necessary. Compared with the previous research,

the polymer contents in the E-sols are substantially lower. Approximately 0.1% to 0.3% PEO was used, which is dramatically less than other reports (e.g. 5 - 8% in ref [175-177]). The microstructures of as-spun fibers are mainly determined by the viscosity and solute concentration of the e-spun solution. From sol E-1 to E-9, solution viscosities were high enough to form continuous fibrous microstructure. The fiber diameter increases from ~315 nm in sol E-7 to ~12 μm in sol E-1, which is assigned to higher viscosity of the solution at higher concentration. The fiber diameter obtained from sol E-8 was greater than that from E-7. This is probably due the viscosity difference in the two precursors, since higher viscosity generally results in a larger fiber diameter. The viscosities of E-7 and E-8 are not presented in here, because of the limitation of our viscosity testing instrument. The viscosities of E-7 and E-8 were too low to be accurately determined, both were below 0.1 poise. The concentration of PEO nearly doubled in sol E-8 than in E-7; and the sol concentration for both, in the term of mullite yield, was similar. In sols E-10 to 11, surface tension was dominant and beaded fibers were formed during the electrospinning process. The conventional PPT/e-spin method shows discrepancy in making thick fibers such as microfiber. This is due to the formation of wide and flat ribbon shaped fibers at high polymer doping level [175-177]. Thanks to the low polymer content, ribbon-like fibers were not engendered in current approach. The fibers obtained from the sol-gel/e-spin precursor shows round shape with controlled diameters from nano- to micrometers, which is unprecedented in previous studies.

The mixing level between TEOS and aluminum alkoxide during hydrolysis is important because sometimes these two chemicals can phase separate during hydrolysis,

resulting in the so-called diphasic gel [74]. The diphasic gel decreases the fiber strength and creep resistance at high temperatures [107]. The obtained mullite fibers had low crystallization temperature at below 1000°C. Thus the grain growth can be effectively prohibited [107, 190, 191]. The single mullite phase formation was caused by the controlled hydrolysis reaction in moderate acidic condition (e.g. pH = 3 - 4.5). This yields Al-O-Si bonding in atomic level [73]. The simple unit of aluminosilicate complex then polymerizes in a preferentially linear arrangement, which facilitates the fiber formation [196]. Phase separation does not occur in the above mentioned precursors. They are often referred as the monophasic precursors. In contrast, diphasic precursor will have phase separation, and as a result, the spinel phase was observed during crystallization [74]. The XRD results show that only single mullite phase was observed at between 800 - 1200°C without any spinel phase. The monophasic gel is desired for two reasons. First, the complete phase formation without significant grain growth at low temperatures is important for mechanical strength. Second, the spinel phase can be avoided to ensure the high temperature creep resistance. In our work, grain growth was inhibited in all fibers with average grain size below 10 nm after firing at 1000°C. In the di-phasic system, the grain size is about 100 nm due to a higher phase formation temperature at 1200°C, where co-existence of γ-AlO_3 phase was also observed [175].

In the DTA experiment, the kinetics of reactions of the type solid state reactions (e. g. crystallization of the amorphous gel) is reflected by the peaks in the curves due to the changes in heat flow and thermal parameter of the samples. The transformation often possesses an activation energy. And the rate of reaction is written in the form that is

proportional to the rate constant ($k(T)$, which is an exponential function of temperature T) times a function of the amount of reactant ($f(X)$, X the fraction of reactant remaining) [197]. The position of the peak varies with the heating rate P_r with other experimental parameters fixed. The variation of the peak temperature could be used to determine the activation energy E_a. The activation energy can be calculated from the DTA exothermic peaks using the Kissinger's equation [197, 198],

$$\ln\left(\frac{T_p^2}{P_r}\right) = \ln\left(\frac{E_a}{R}\right) + \frac{E_a}{RT_p} - \ln\nu \tag{2.5}$$

where T_p is the exothermic peak temperature; R is the gas constant; and ν is the frequency factor constant, which is defined as: $\nu = \frac{df(X)}{dX}$ [197]. Eq. (2.5) is applicable for the reaction that proceeds at a rate varying with temperature, that is to say, the process is thermally activated. And a basic assumption is that the same mechanism and kinetics parameters hold throughout the reaction, which has been proved in the nucleation-growth of mullite [199]. The activation energy for mullite phase formation (also known as mullization) calculated from Eq. (2.5) was E_a = 1411 kJ/mol by linear fitting the data obtained from the DTA experiment (shown in Figure 2.12). This value is in good agreement with many of the previous reports [199-201]. Okada showed that in monophasic gels, the E_a values for mullization range from 800 to 1400 kJ/mol [201]. The corresponding crystallization temperature has a maximum of about 1000°C [201]. This further testifies the monophasic character of the mullite sol.

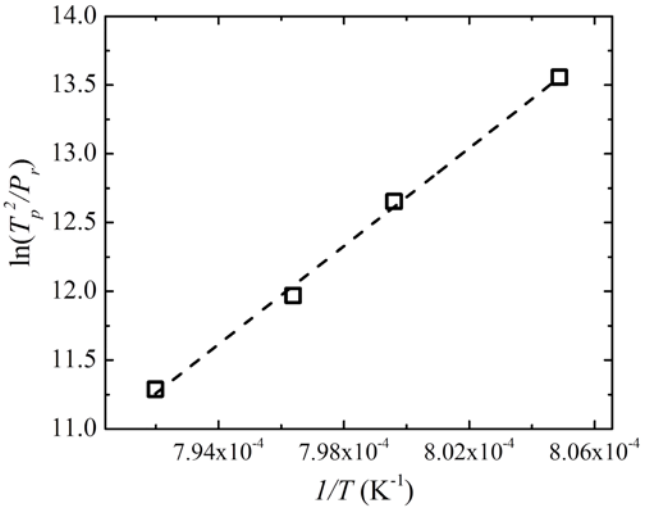

Figure 2.12. The plot of Kissinger's equation to derive the activation energy of crystallization of mullite gel

To our best knowledge, there are very few works have been done on measuring the mechanical properties of electrospun mullite fibers. However some works can be found for measuring the mechanical properties of small diameter (e.g. 3 - 5 μm) dry-spun mullite fibers [202, 203]. Li *et al.* reported a tensile strength of 1.1 - 1.4 GPa for the phase pure mullite fiber of diameter of 3 -5 μm [202]. A tensile strength of 1.3 - 1.6 GPa was reported for alumina rich electrospun mullite fibers of diameter 3 - 12 μm [203]. The tensile strength of the mullite fibers obtained in our study is similar or slightly better than the studies of dry-spinning mullite fiber [202, 203]. This shows the importance of controlling the spinning aid contents. The polymer spinning aid usually leaves porous microstructure after burned off. Controlling the hydrolysis process can significantly reduce the needed spinning aid content, and thus resulting in improved mechanical performance. The grain size to diameter ratio has a crucial effect on the mechanical properties of the fibers. For instance, significant and exaggerated grain growth was found to deteriorate the failure strength of

mullite microfibers [204]. In nanofiber systems, grain growth determines the nanocrystalline structure and mechanical performance [90]. Sometimes good mechanical properties of nanofibers may take advantage of the small grain size and high volume fraction of grain boundary of the nanocrystalline structures.

The results of the bending test were compared with those obtained from the tensile test. An average elastic modulus of about E = 100 GPa was found, which is in agreement with the value found from the bending test. In the tensile test, the fiber strength was identified as 1.25 GPa with 10mm gauge length. On polymeric fibers, the tensile test usually provides a greater elastic modulus relative to that obtained from the bending test [188]. This tendency was explained by the orientation effect of polymer chains during tensile testing: the applied load on an Instron machine is much greater than that experienced by a polymeric fiber upon magnetic flexing. This effect leads to an apparent reinforcement of the fiber after tensile test [205]. As follows from the present results, this effect of apparent hardening does not occur in ceramic fibers.

2.5 Conclusion

In this chapter we demonstrate the processing and characterization of mullite fibers from monophasic sol-gel precursor using electrospinning. The fiber diameter can be controlled with the solute concentration in the electrospinning precursors. Fiber diameters can be controlled from 400 nm up to ~15 μm. The obtained fibers showed narrow diameter distributions. The fiber had an average strength of 1.25 GPa for 1 cm gauge length, and 1.46 GPa for 0.5 cm gauge length. Using the Euler elastic model, we were able to describe the fiber bows. Therefore, the shear deformations in ceramic fibers are not significant. In

the tensile test, the elastic modulus of E = 100 GPa and the fiber strength 1.25 GPa were obtained. In the bending test, the flexural rigidity of $2.06 \times 10^{-12} Pa \cdot m^4$ and elastic modulus of E = 103 Ga were obtained. These results indicate that mullite microfibers are flexible and, due to their microstructural uniformity, do not generate significant shear stresses during bending. These mechanical properties show that electrospinning can be used to fabricate small diameter mullite fibers with good mechanical properties, making them attractive candidates in generating advanced ceramic composites materials for extreme applications.

CHAPTER III

FUNCTIONALIZATION OF MULLITE FIBERS BY NICKEL NPS USING THE IN-SITU REDUCTION METHOD

3.1 Introduction

Many research efforts have been made in nanocomposite thin films with unique properties and multi-functionality comprising nanoscaled constituents [136, 206, 207]. Unprecedented properties can be achieved with the ceramic-based nanocomposite thin films embedded with metallic nanoparticles (NPs) [136, 206, 207]. The fabrication of such nanocomposite is an emerging field of science and technology that has attracted huge interests in the recent years [136, 206, 207]. The magnetic functionalization of non-magnetic nanofibers (e.g. the mullite nanofibers) using metallic nanoparticles provides attractive candidates as fillers in ceramic thin films for advanced applications.

The thermal reduction method is one of most applicable methods to process ceramic nanocomposites, through which metal oxide precursors can be converted to dispersed metallic nanoparticles with a heat-treatment in the reducing atmosphere [82, 126]. In this chapter, we present the method of synthesizing mullite-nickel nanocomposite fibers using electrospinning, followed by thermal reduction. A particular challenge in our study is attributed to the formation of intermediate metastable phase (spinel) other than mullite as the matrix. The formation of metastable phase is not desired, as it is deleterious to the high temperature mechanical properties of mullite. The spinel phase is avoided with proper heat-treatment procedures. We found that the Ni NPs within the mullite fiber has an equilibrium

size of ~20 nm, while the Ni NPs on the fiber surface can grow much larger. The magnetic properties of the nanocomposite fibers reflect this microstructure feature.

3.2 Experimental Procedure

Following the findings in chapter 2, e-spin solution E-6 was chosen to generate fibers with submicrometer diameters. Nickel nitrate hexahydrates ($Ni(NO_3)_2 \cdot 6H_2O$, 95%, Aldrich, MO, USA) was used as the Ni source in the precursor. Solution E-6 was mixed with nickel nitrate at varying concentrations (Ni: 2, 5 and 10 wt. % of mullite yield). Electrospinning was carried out under the same conditions in chapter 2. In order to obtain the mullite phase with embedded nickel NPs, a two-step heating sequence was applied. In the first step, the precursor fibers were heat treated in the reducing gas (5 vol. % H_2 in Ar) to a temperature between 650 to 750°C and isothermally kept for 10 hours to form metallic NPs. The heating rate was set at 1°C/min below 500°C and 5°C/min above 500°C. In the second step, the fibers were heat treated and crystallized at 1000°C for 30 minutes under 5% H_2 - Ar. A parallel calcination experiment was performed in air, in order to demonstrate the effect of heat treatment procedure on the phase transformations. Table 3.1 summarizes detailed information for samples named with different nickel concentration and heat treatment conditions.

Table 3.1. Materials composition, isothermal reduction temperature and heat treatment atmosphere for different Ni-mullite fibers

Specimen codes	Nickel content(wt. %)	Isothermal reduction temperature (10 h)	Crystallization temperature	Heat treatment atmosphere
MN2-750R-1000	2	750°C	1000°C for 30 min	5 at. % H_2 in Argon
MN5-750R-1000	5	750°C	1000°C for 30 min	5 at. % H_2 in Argon
MN5-750R	5	750°C	NA	5 at. % H_2 in Argon
MN5-750R-850	5	750°C	quench at 850°C	5 at. % H_2 in Argon
MN5-A	5	NA	quench between 1000 and 1400°C	Air
MN5-H_2	5	NA	quench between 1000 and 1400°C	5 at. % H_2 in Argon
MN10-750R-1000	10	750°C	1000°C for 30 min	5 at. % H_2 in Argon
MN10-700R-1000	10	700°C	1000°C for 30 min	5 at. % H_2 in Argon
MN10-650R-1000	10	650°C	1000°C for 30 min	5 at. % H_2 in Argon

The thermal behaviors were studied at different heating rate under flowing air or 5% hydrogen - Argon condition using DTA (DTA7, Perkin Elmer, Waltham, MA, USA). The crystalline phases were identified using X-ray diffraction (XRD, Rigaku Co., Ltd., Tokyo, Japan); the microstructure was characterized using scanning electron microscopy (SEM, Hitachi S4800**,** Hitachi, Ltd., Tokyo, Japan) and transmission electron microscopy (TEM, Hitachi 9500 300kV microscope, Hitachi, Ltd**.,** Tokyo, Japan). The average size of fiber diameters or Ni NPs on the fiber surface was calculated from the average of more than 100 randomly selected fibers or NPs taken from SEM micrographs. The magnetic properties of the composite fibers were measured by using the Alternating Gradient Magnetometer (AGM 2900, Princeton Measurements Inc., NJ, USA).

3.3 Results

Figure 3.1 shows the XRD traces of mullite-nickel fibers after heat treatment in 5% hydrogen. The near complete conversion of Ni^{2+} to Ni was reached after thermal reduction at 750°C for 10 hours. For all five samples (MN2-750R-1000, MN5-750R, MN5-750R-850, MN5-750R-1000 and MN10-750R-1000), mullite and nickel were the only two phases observed after the sample was first reduced at 750°C and then quenched at 850°C or crystallized at 1000°C. No residual NiO or spinel phase was observed. Mullite peaks of MN5-750R and MN5-750R-850 were weak. The mullite peaks became strong for MN5-750R-1000. The intensities of nickel peaks compared to the peaks of mullite relatively enhanced with increasing nickel loading, as shown with samples MN2-750R-1000, MN5-750R-1000 and MN10-750R-1000. Coexistence of mullite, nickel and spinel phase was observed in samples (MN10-700R-1000) that were reduced at 700°C for the same duration. The spinel phase was probably a solid solution between Ni-Al spinel (Al_2NiO_4) and Al-Si spinel (near $SiO_2 \cdot 6Al_2O_3$), which will be discussed in the next section. Only nickel and spinel phase were observed in the sample that was reduced at 650°C and then heated to 1000°C (MN10-650R-1000).

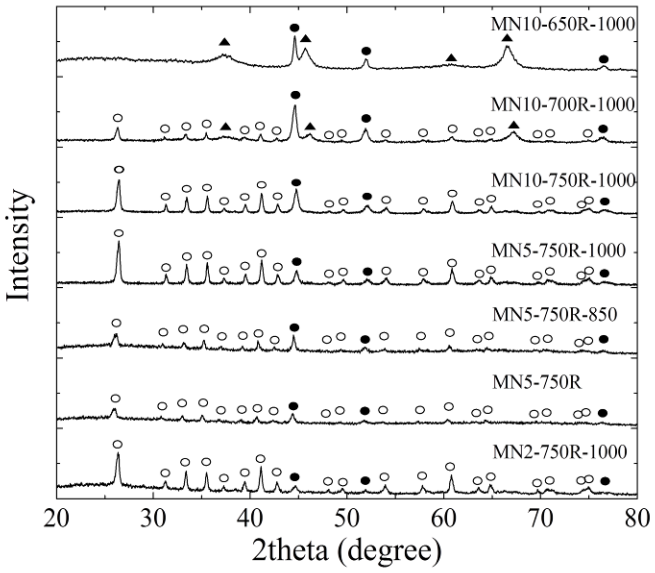

Figure 3.1 XRD patterns of mullite-nickel nanocomposite fibers with different Ni concentration heat treated in 5% H_2-Ar for 10 h, and/or then heated at 850 or 1000°C for 30 min. Labeled phases: ● nickel, ○ mullite, ▲ spinel.

The results of Figure 3.1 suggest that the Ni^{2+} concentration influences the crystallization behavior of mullite. To study this effect, we carried out heat treatment on MN5A samples in air from room temperature to 1400°C. The XRD patterns of the specimens after calcining at different temperatures are shown in Figures 3.2. In last chapter we showed that the fibers without Ni^{2+} addition remained amorphous at low temperatures and were directly transformed to mullite after calcining at 1000°C. No intermediate phase, such as spinel was observed. However, when 5% Ni^{2+} was doped, the spinel phase was observed in MN5-A fibers after calcining at 1000, 1100, 1200 and 1300°C. Trace amount of mullite was observed at temperatures between 1000 and 1300 °C.

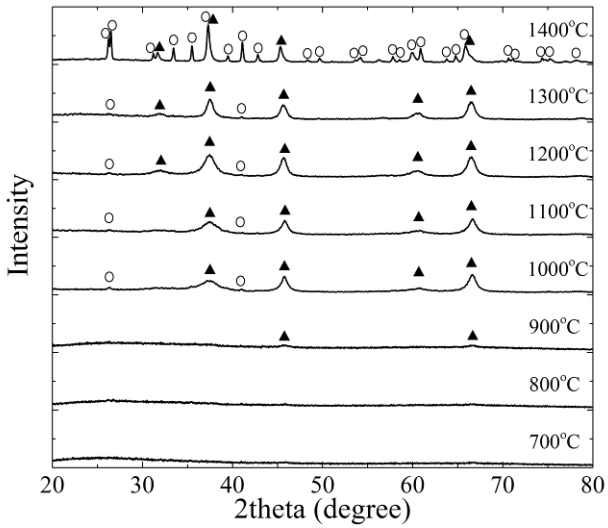

Figure 3.2. XRD traces of MN5-A (5 wt. % Ni loading) fibers heat treated in air. Labeled phases: ○ mullite, ▲ spinel.

The DTA scans of pure mullite (non-doped) and 5% Ni-doped mullite gels under air or 5% H_2 are shown in Figure 3.3. The curves of non-doped mullite, MN5-H_2 and MN5-A are similar at low temperatures, as shown in Figure 3.3 (a). The endothermic peaks around 150°C and 300°C were due to loss of residual solvents and decomposition of organic components. Diverse DTA profiles were observed at temperature ranging from 900 to 1000°C. The non-doped mullite showed a sharp exothermic peak at around 980°C which was due to crystallization of mullite (as we discussed in chapter 2). While a broad exothermic peak corresponding to mullization was observed in MN5-750R-H_2 at around 950°C. MN5-A showed a broad exothermic peak at around 930°C corresponding to the crystallization of Al-Si spinel. No endo- or exothermic peak at temperature ranging from 900-1000°C was observed in MN5-H_2.

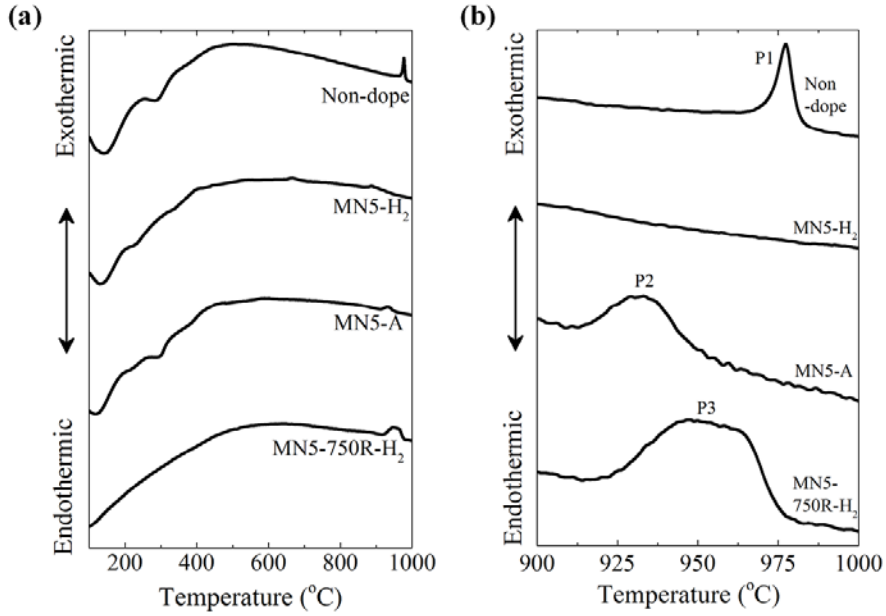

Figure 3.3. Curves of DTA scans at 5°C/min for pure mulite gel in air (non-dope), 5% Ni-mullite in 5% H_2 (MN5-H_2), 5% Ni-mullite in air (MN5-A) and 5% Ni-mullite pre-heat-treated at 750C for 10 h under 5% H_2 (MN5-750R-H_2). P1, P2, and P3 are the exothermic peaks between 900 to 1000°C.

Figure 3.4 shows the SEM micrographs of mullite-nickel fibers after heat treatment in hydrogen. The fiber showed uniform diameter and good straightness. Nickle particles were observed on the surface of the fibers. Diameters of 800 nm - 1 μm were observed. Figure 3.5 shows the TEM images of reduced mullite-nickel fibers with 2 wt.% and 5 wt.% Ni doping. The TEM images indicate that the metallic phase NPs were dispersed within the mullite matrix. No separation at the boundary was observed between mullite and Ni phase which indicates good adhesion between the metal and ceramic phases.

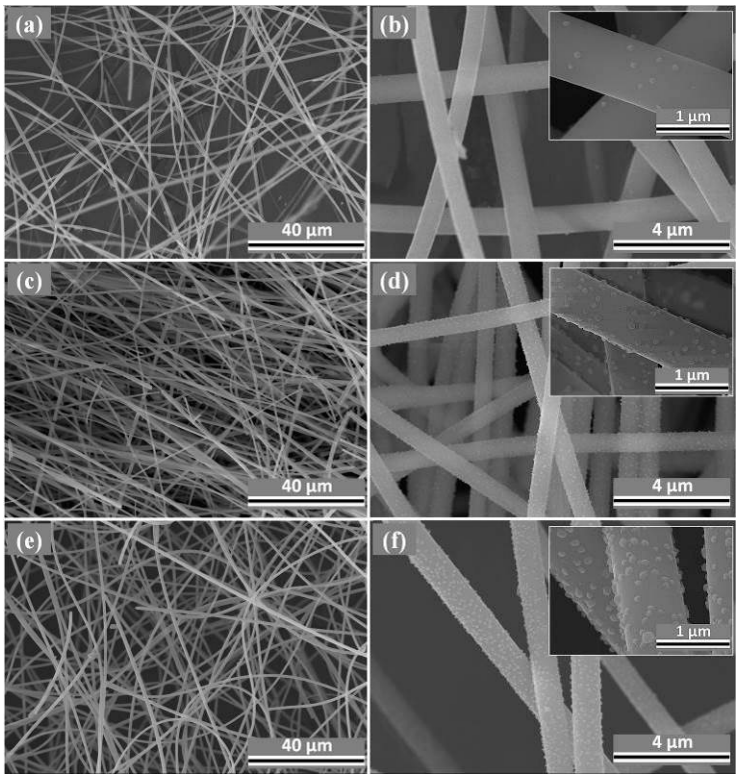

Figure 3.4 SEM images of MN2-750R-1000 ((a) & (b)), MN5-750R-1000 ((c) & (d)) and MN10-750R-1000 ((e) & (f)) mullite-nickel nanocomposite fibers.

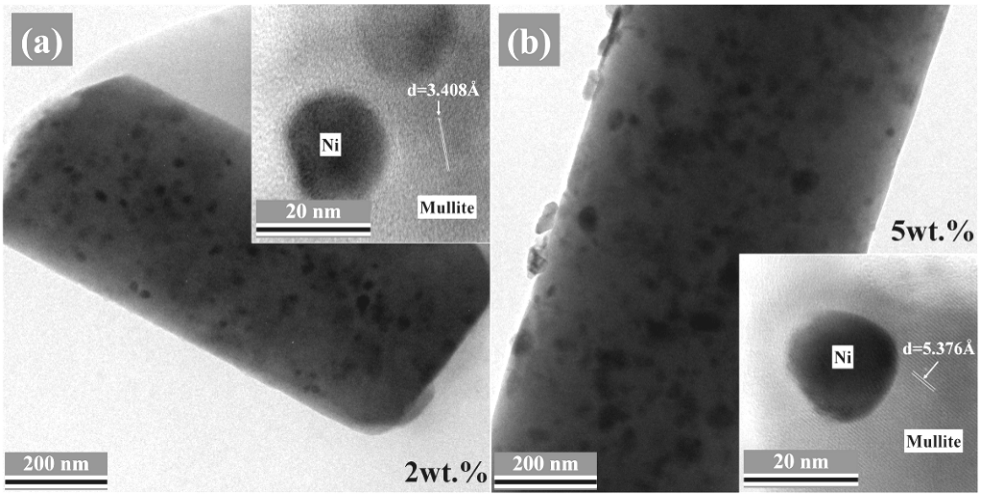

Figure 3.5. TEM images of (a) MN2-750R-1000 and (b) MN5-750R-1000.

The average sizes for Ni NPs observed from fiber surface using SEM micrographs are summarized in Table 3.2. We observed generally smaller Ni NPs within the fiber than on those on the surfaces. However using TEM, it was difficult to generate a representative

average particle size. Thus here we only present the particle sizes on the surface, which was obtained from SEM micrographs. In the ceramic/metal nanocomposites derived from reduction of solid solution, a bimodal particle size distribution for the dispersed phase was usually observed [208]. Relatively large particles were observed on the surface of the fibers and small particles were observed inside the fibers. The increasing of Ni salt loading gave rise to a large size for Ni NPs and range of size distribution.

Table 3.2 Particle size of nickel and the magnetic properties

Specimen name	Average surface particle size (nm)	Overall average particle size (nm)	M_s (Am^2/kg)	M_r (Am^2/kg)	H_c (kA/m)	Observed phase(s)
MN10-750R-1000	80	19	4.177	1.136	6.83	mullite and Ni
MN10-700R-1000	75	NA	3.494	0.592	4.62	mullite, spinel and Ni
MN10-650R-1000	40	NA	0.199	0.031	2.47	spinel and Ni
MN10-550R-1000	15	NA	0.085	0.005	1.68	spinel and Ni
MN5-750R-1000	55	20	1.826	0.409	4.09	mullite and Ni
MN2-750R-1000	25	19	0.918	0.091	1.74	mullite and Ni

The average crystallite size of Ni NPs was determined by the Scherrer Equation from the X-ray diffraction [209]:

$$\tau = \frac{K_S \lambda}{\beta \cos\theta} \tag{3.1}$$

where τ is the crystallite size, K_s the dimensionless shape factor (equal to 0.9 for a spherical crystallite), λ the wavelength of X-ray beam (1.54 Å used in our experiment), β the full width at half of the maximum intensity (FWHM) and θ the X-ray diffraction angle. The τ values for MN2-750R-1000, MN5-750R-1000 and MN10-750R-1000 specimens were

calculated according to Eq. (3.1) and is summarized in Table 3.2. The values were obtained from the peaks corresponding to the [111]-plane which showed the highest intensity. The calculated τ of Ni NPs had almost identical values of around 20 nm. The τ values were compared with the particle size evaluated from SEM and TEM. The particle size in MN2-750R-1000 specimen was very close to the τ value obtained. In the higher Ni salt loaded samples, a significant greater particle size was observed on the fiber surface from the SEM and TEM micrographs. As mentioned earlier, the SEM and TEM studies indicate a bimodal size distribution of Ni NPs on the surface and inside the fiber. The larger particle size was caused by the significant coalescence of Ni crystallites on the fiber surface.

The obtained fibers are highly magnetic and can be easily attracted and lifted by a magnet. Figure 3.6 shows the plots of magnetization versus magnetic field (*M-H* loop) of mullite-nickel composite fibers. A notable magnetic hysteresis was observed in fibers synthesized from the 5% and 10% Ni salt loaded samples. This is also confirmed by a quantitative analysis of fiber magnetization. The Saturation magnetization M_s, Remanence M_r and Coercivity H_c of the samples are summarized in Table 3.2. The measured magnetic moments were normalized by the total weight of the composite fiber. The M_r and H_c values were determined by the zero magnetic moment and magnetic field. At 300K, a small M_s was measured on MN10-550R-1000 and MN10-650R-1000 fibers. The M_s of MN10-700R-1000 was about 17 times of that of MN10-650R-1000. The MN10-750R-1000 fibers exhibit the highest M_s of 4.18 Am^2/kg and H_c of 6.83 kA/m. With the increasing temperature, a significant increase of M_s was observed, which implied that a greater portion of Ni^{2+} cations were transformed into the metallic form. The H_c value increased with

increasing Ni salt concentration and temperature, which implied a greater particle size of Ni.

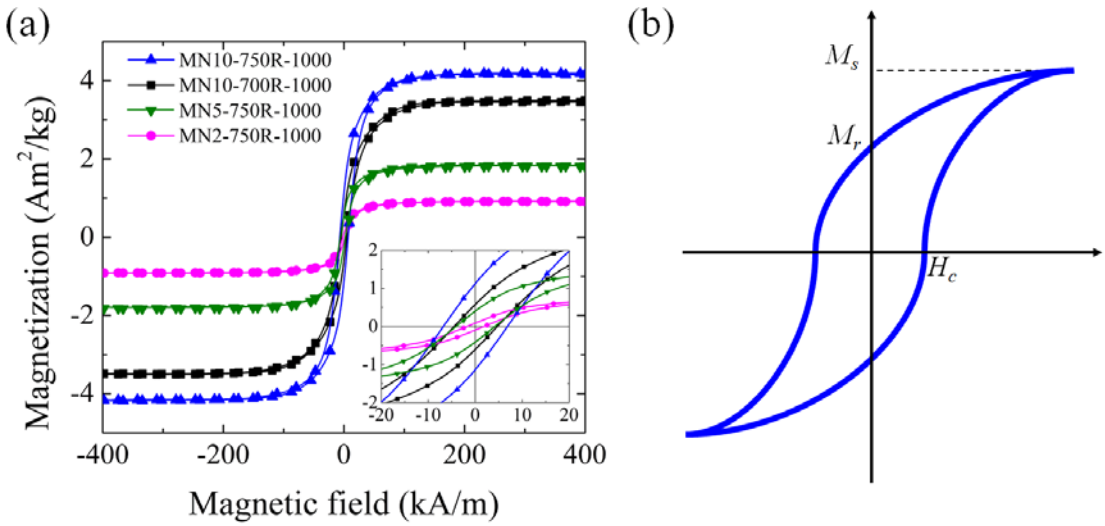

Figure 3.6. (a) Magnetic properties of mullite-nickel composite fibers (b) Schematic illuminating the meaning of M_s, M_r and H_c.

3.4 Discussion

In chapter 2, we discussed the sol-gel precursors for mullite, which are usually divided into monophasic and diphasic gels. The monophasic gel can be directly transformed to mullite phase without intermediate phases. The diphasic gel features the formation of intermediate phases, such as Al-Si spinel. For the non-doped mullite fibers, the monophasic gel characteristics were proven by XRD and DTA results showing no metastable phases during crystallization. For the fibers doped with nickel, the presence of Ni^{2+} cation induced the formation of spinel, which suppressed the formation of mullite until above 1400°C [210]. If the fibers were isothermally reduced at a temperature lower than 750°C, the spinel phase, instead of the mullite phase, was formed at 1000°C. Table 3.3 summarizes the positions of the top three intense x-ray diffraction peaks which correspond

to the 311, 400 and 440 crystalline planes of Al-Si and Ni-Al spinels. A clear trend can be seen with an increasing the 2θ angle at higher isothermal reduction temperature, indicating a gradual decrease of the lattice parameter.

Table 3.3. Comparison of the peak positions of {311}, {400} and {440} of the spinel phase from this work and references

Specimen name	2θ (degrees)			Reference
	{311}	{400}	{440}	
MN10-550R-1000	37.36	45.7	66.6	This work
MN10-650R-1000	37.36	45.7	66.7	This work
MN10-700R-1000	37.45	46.2	67.1	This work
Al_2NiO_4	37.01	45.0	65.7	[213]
Al-Si Spinel	37.81	46.0	66.7	[212]
γ-Al_2O_3	37.71	45.9	66.5	[212]

In this study, the identified spinel phase could be a solid solution of Al-Si spinel and Al_2NiO_4 spinel. The Al_2NiO_4 spinel has a larger lattice parameter of 8.050 Å than those of Al-Si spinel and γ- Al_2O_3 [211-213]. The Al-Si spinel (~8 wt. % SiO_2) and γ-Al_2O_3 have close lattice parameters *a* which are respectively 7.886 and 7.906 Å [212]. The lattice parameter of $NiAl_2O_4$-γ-Al_2O_3 (Al rich) solid solution was reported to be 8.011-8.034 Å which further depends on the amount of the dissolved Ni^{2+} cations [213]. In our experiment, more Ni^{2+} cations were converted into metallic phase at a higher reduction temperature. This coincided with our observation that the crystal unit cell became smaller (2θ shifts to higher angle) if the fibers were reduced at the higher temperatures. Therefore we interpret that the residual Ni^{2+} were dissolved in a solid solution containing Al-Si and Al-Ni spinels.

Upon thermal reduction, the metallic nickel phase first nucleates within an amorphous Al_2O_3-SiO_2 matrix. After the Ni^{2+} cations were reduced, the Al_2O_3-SiO_2 matrix exhibited monophasic characteristics and crystallizes at around 950°C. The importance of

retaining the monophasic characteristics is that a higher temperature (e.g. ~1400°C) for sintering is essentially needed to eliminate the spinel phase. This high temperature heat-treatment is undesirable because the metallic nickel NPs coarsens when the sintering temperature is close to the melting point of Ni (1455°C) [128]. In that case it is difficult to obtain nickel particles of nanometer size. The mullite crystallization temperature in nickel-mullite systems reduced at 750°C is lower than that in non-doped mullite system. This shift could be explained by the increasing number of sites available for nucleation-growth of mullite in the presence of finely dispersed nickel NPs. The boundary between Ni NPs and amorphous matrix tends to act as nucleation sites for mullite nucleation and growth [214]. The reduced energy barrier for nucleation can be used to explain this catalytic effect and temperature shift (about 30°C) for mullite crystallization.

Eq. 3.1 was applied to calculate the activation energies for crystallization of mullite and spinel, which are summarized in Table 3.4. We showed in chapter 2 that the pure mullite gel is monophasic. For mullite crystallization with the presence of Ni NPs, the activation energy was slightly smaller (1221 kJ/mol) than that of the pure mullite gel. This difference could be assigned to the error generated in determining the T_p values of the broad exothermic peaks in mullite-nickel samples. Nevertheless, the value (1221 kJ/mol) stayed in the range for monophasic mullization. The DTA curve of MN5-H2 was significantly different from that of MN5-750R-H2, because in MN5-750R-H2, the pre-existing nickel nanoparticles served as heterogeneous nuclei for mullite growth. Under constant heating rate, heterogeneous nucleation and crystallization overlapped over a wide temperature range. Thus in the DTA curve of MN5-H2, instead of observing a strong exothermic peak,

we did not observe an obvious peak. The activation energy for spinel formation in MN5-A specimen had been determined to be 1131 kJ/mol. This value was slightly lower than the di-phasic mullite gel system doped with 3wt. % of nickel, of which has activation energy of 1320 kJ/mol was reported [210].

Table 3.4. Calculation of the activation energies of the crystallization of mullite and spinel; Avrami constant for nucleation and growth of Ni-mullite fibers

	Mullization in MN0-A	Spinel crystallization in MN5-A	Mullization in MN5-750R
Activation energy(kJ/mol)	1403±58	1131±187	1221±282
Avrami constant	3.156±0.438	1.143±0.063	0.773±0.031

The mechanism of crystallization is described by the Avrami constant. The constant indicates that the solid transforms through the 3-dimensional growth of the nuclei (bulk crystallization) or the growth that is restricted to 1 or 2-dimensions (surface crystallization). The crystallization mechanism could be determined from the Avrami constant *n* by the Augis-Bennett equation [215]:

$$n = \frac{2.5RT_p^2}{\Delta T E_a} \tag{3.2}$$

where ΔT is the full width at half maximum of the exothermic peak. The rest of the parameters were defined in chapter 2. Small value of n indicates surface crystallization mechanism instead of volume crystallization. The resulting Avrami constants are summarized in table 3.4. A relatively greater value of *n* for mullite crystallization indicates a volume crystallization mechanism. Such mechanism of crystallization is often observed in materials that are homogeneous [215]. On the other hand, a small *n* for mullite crystallization in MN5-750R was obtained, revealing the surface crystallization mechanism. Such mechanism of crystallization is often observed in heterogeneous

materials [215]. The surface crystallization mechanism was interpreted by the catalytic sites provided for nucleation at the interface between Ni NPs and the matrix phase that facilitates the growth.

The M_s, M_r and H_c of bulk nickel at room temperature (300K) are about 55 mAm^2/kg, 2.7 mAm^2/kg and 8.0 kA/m [216]. The saturation magnetization of nano-sized particles is usually smaller than that of the bulk materials due to the interfacial rearrangement of spins of ferromagnetic particles [217-216]. M_s of the composite fibers, if normalized by the weight of nickel, were about 70%-80% of the bulk nickel. It is known that coercivity of the magnetic particle is sensitive to the particle size corresponding to a single or multi-domain structure. As the particle size decreases, fluctuations of the spin orientation become important and the particle behave as a superparamagnetic particle. The small H_c observed in MN2-750R-1000 specimen indicated a stronger size effect. In our experiments, the normalized value M_r/M_s was about 0.1, the H_c of the 2% sample being 1.74 kA/m, implying the dominance of the superparamagnetic NPs. The suggested method to achieve superparamagnetism was to decrease the Ni-salt concentration and the lower the reduction temperature.

In the previous literature, precipitation and growth of metallic NPs in a refractory ceramics has been thought as a diffusion-limited process by the transport of either electrons or oxygen vacancies [138]. The Schmalzried model was applied to describe the growth of Ni NPs, which starts from the grain boundaries [138, 219]. In our study, we observed significantly different growth behaviors on the surface and inside the ceramic host. The growth of the surface particles depends on the concentration of Ni-salts. As shown in

Figure 3.7, the NPs precipitated within mullite, on the other hand, were insensitive to the concentration of Ni-salts, which indicates a totally different growth mechanism. It has been reported that the volume change during phase transformation can impose large strain energy on the system and thus possibly impose a thermodynamic energy well resulting in an equilibrium particle size [220]. The equilibrium size at high temperatures and its relations to the mechanical state of the nanoparticles will be investigated in detail in chapter 4.

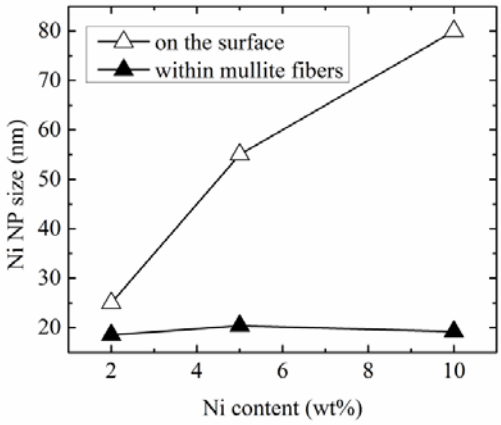

Figure 3.7. The Ni NP sizes on the fiber surface and within mullite vs. different Ni concentrations. The samples were heat-treated at the same temperatures.

3.5 Conclusion

Mullite-nickel nanocomposite fibers were obtained via the reduction on heating the sol-gel/electrospinning-derived fibers. The reduction of the mullite-nickel fibers resulted in the nanocomposites with Ni NPs embedded in the mullite host fibers. With the reduction of Ni^{2+} at 750°C, the formation of spinel phase was prevented. Suppressing the spinel phase formation helped to obtain only mullite phase at low temperatures (~1000°C). Nickel NPs had a size of about 20 nm within the mullite fibers, which was insensitive to the Ni

concentration. The surface Ni NPs had larger sizes with higher Ni concentration at the same heat-treatment temperatures. The presence of Ni NPs slightly lowered the temperature for mullization, which was ascribed to the catalytic effect of secondary phase particles providing heterogeneous nucleation-growth sites at the interface between nickel NPs and matrix. The magnetic characterization of the composite fibers suggested ferromagnetism. A small coercivity close to superparamagnetic behavior was obtained in mullite fibers with Ni NPs, which was due to the small size of nickel NPs in the matrix. Relatively large Ni particles on the surface contributed to the ferromagnetism widening the hysteresis loop.

CHAPTER IV

HIGH TEMPERATURE STABILITY OF NANOPARTICLES IN CERAMIC FIBER HOST

4.1 Introduction

4.1.1 Challenges and problem formulation

Transition metal nanoparticles (NPs) (e.g. Au, Pt, Ag, Cu, Ni, Fe, Co) belong to an important family of materials that enjoy broad applications in energy conversions, chemical sensing, plasmonics and many other applications in electronics [221-223]. High temperature stability of metal nanoparticles has been a long standing problem in the field of catalysis and high power laser plasmonics [38, 39, 140, 141]. Over time, the metal NPs suffer degradation at high temperatures and, if embedded with ceramic materials, they are prone to coalesce and sinter [38-40]. Coarsening is usually irreversible and nanoparticles have an inherent tendency to come together in order to minimize their total surface energy. This complex process of collapse or coalescence of small particles and growth of large particles is called Oswald ripening [224-226]. It is generally believed that the Ostwald ripening is the most important cause of the degradation of small NPs and growth of the large ones at high temperatures [224-226]. Although stabilization of metal nanoparticles at high temperatures within a ceramic host is highly desirable, it is believed that the kinetic process of coarsening is fundamentally unstoppable.

Ceramic host is often considered as a good diffusion barrier slowing down the sintering process [142, 143]. In chapter 3 we observed different mechanisms for the growth of Ni NPs on the surface and inside mullite fibers. As the time progresses and the surface

particles keep grow, the internal particles seem to stop the growth. This discovery contradicts the currently accepted scenario of nucleation of NP in solids and calls for its careful analysis.

When nanoparticles precipitate from a solid solutions, elastic fields cannot be simply ignored: metal is much denser than ceramic matrix, hence a metal precipitate always pull the surrounding material towards its surface causing the matrix to deform [227-229]. In a homogeneous solid solution, an addition or withdrawal of the solute atoms do not change significantly the structure of the host solvent. Our system is unique because the supersaturated solution is amorphous, that is, the atoms and molecules are not organized in a definite lattice pattern. However, one cannot add the dopants infinitely: when the solute concentration surpasses the solubility limit of the solvent, the solid solution becomes supersaturated, resulting in nucleation of the solute crystals. As a result, the solid turns into a two-phase system, e.g. in our case, Ni nanoparticles are precipitated out from its host mullite. When this happens, Ni NP immediately generates elastic stresses in the mullite matrix due the volume misfit. Due to the specific dependence of misfit strain on matrix composition, such phase transformation cannot be modeled on the basis of thermodynamics that is valid only for liquids.

Many of the theoretical approaches modeling the growth of precipitated nanoparticles with elastic fields generated by the misfit between particle and matrix have been based on the energetic calculations [227-229]. According to the inverse coarsening theory, the free energy of a system is the sum of the total elastic energy and the total interfacial energy. The total free energy of the system must decrease as the system of

particles evolve. The analysis showed that for a pair of elastically interacting particles, the energy of the system would decrease if the small particle were to grow at the expense of the large one. The condition corresponding to the nucleus growth is exactly opposite to the interfacial energy driven coarsening, therefore, the process is often called the inverse coarsening [227-229]. Elastic strain favors an array of equally sized precipitates for the reason that equally sized particles can be a minimizer of the system's free energy [227-229]. The dynamic approach by solving the field equations under quasi-stationary approximations: $\nabla^2 C = 0$ for concentration of solute atoms in the matrix with stress-modified boundary conditions, and the kinetics equations for particle growth also confirms the observation of inverse coarsening for a system of particles of equal size [227]. However, this theory cannot explain the possible stabilization of the multi-particle system with certain particle size distributions.

Our discovery of the growth stagnation of Ni NPs inside mullite nanofibers, calls for development of a new theory which we introduce below. The Ni nanoparticles, called here the β phase, are considered uniformly dispersed in a matrix, called here the α phase. These two immiscible phases (α and β) are separated by an interface (I). The essential difference between our theory and the inverse coarsening theory is that the deformation of the interface causes a different concentration distribution of Ni atoms in the matrix [230]. The concentration in precipitate and matrix phase is schematically shown in figure 4.1. In the inverse coarsening theory, the concentration field in the matrix is non-uniform, which is determined by the field equations describing mass flow in a stressed solid [230]. The difference between far field concentration of Ni atoms C_∞^α and interface concentration of

Ni atoms C_I^{α}, is the thermodynamic driving force for particle growth. In our theory, the composition in the matrix is assumed uniform. This flat composition profile accounts for the cease in particle growth over time, through a universal change of concentration of Ni atoms in the matrix during precipitation. Such compositional change imposes change in atomic volume in the matrix and therefore a dilatational strain. The dilatational strain will in turn, affects the mechanical equilibrium at the interface. The effect of non-uniform stress field on the compositional distribution in the matrix was neglected in our theory. Additionally, the classic theories assume constant far-field concentration C_{∞}^{α} [227-229]. As in our case, C_{∞}^{α} depends on the growth of the nanoparticles. That is to say, the total volume of the second phase β (Ni NPs) is not constrained.

Formulation of this problem is based on the following basic postulations:

1. During precipitation, the far field concentration in the matrix can change with time. The compositional change in the matrix leads to the dilatational strain which determines the mechanical equilibrium at the interface.

2. The mechanical equilibrium at the interface further determines the equilibrium concentration of Ni atoms (C_I^{α}) at the interface, that levels with the far field concentration at the time of particle growth stagnation. The flat concentration profile is maintained with the cease in growth of the Ni NPs.

3. The interface between the precipitate and the matrix is assumed coherent. That is, the displacement field is continuous across the interface.

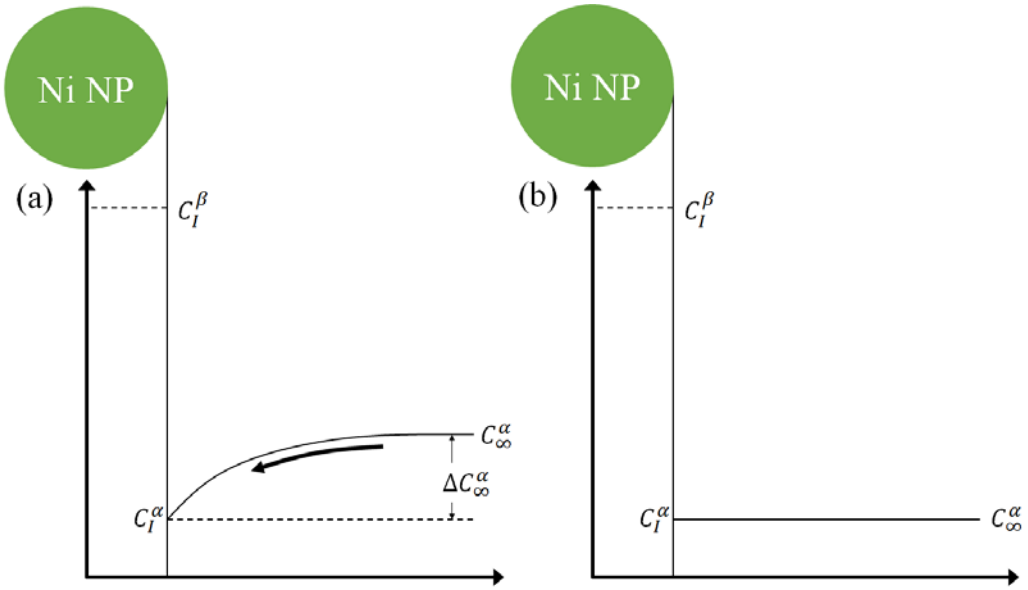

Figure 4.1 Schematic representation showing concentration in matrix (α) and precipitate (β) phase corresponding to the inverse coarsening (a) and our theory (b). C_I^α and C_I^β are the equilibrium concentration of Ni atoms at the interface in α (mullite-nickel solid solution) and β (Ni) phase respectively. C_∞^α is the far-field concentration.

The advantage of our theory is that it can explain the particle stabilization and the strain-size relation, which was overlooked in classic and inverse coarsening theories [227-229].

4.1.2 The *in situ* TEM

The term '*in situ*' describes an event where it takes place. The *in situ* characterization method enables direct observation and helps to develop improved understanding of the precipitation process. Precise *in situ* observation of particle growth has been made in many ceramic-metal NPs systems [231-233]. For example, the in situ scanning tunneling microscopy has shown that growth of Pd NPs is governed by the Ostwald ripening mechanism [231-233]. The process of Ostwald ripening evolves through the growth of the larger NPs and shrinkage of the smaller ones [231-233]. In this case, the

total energy of the matrix-particle system is reduced via the increase in the size of the second phase particles, which is accompanied by the decrease of total interfacial area [231-233]. It is attractive to use the *in situ* approach to directly visualize the particle growth in our system at high temperatures.

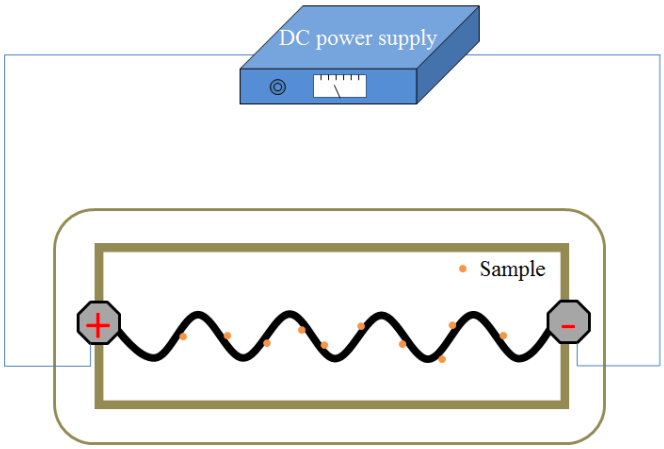

Figure 4.2. Schematically showing the setup of hot stage in TEM.

In electron microscopy, the condition (e.g. the alignment) of the incident electron beam determines the quality of the obtained images. The beam condition can be optimized by adjusting the magnetic lenses during the TEM operation at room temperature. However, for high temperature applications (e.g. the *in situ* TEM), the specimen is often heated by electrical current which generates magnetic field. The magnetic field interferes with the electron beam which compromises the quality of the images. The experimental setup for the TEM hot stage used in our study is schematically shown in Figure 4.2. The samples (nanofibers) were attached to a curved heating element which connects to a DC circuit. The circuit is integrated into the TEM probe which connects to an external power supply. The electrical current that runs through the heating element is controlled by the power supply.

The temperature was calibrated by the probe manufacturer (Hitachi. Ltd) so that the chosen current corresponds the particular temperature.

There are several challenges during the execution of *in-situ* TEM. Firstly, it is desired to maintain the position of materials that are attached onto the heating element. This requests that those nanofibers used in our study must be short. Long fibers are easily disturbed by thermal fluctuations which changes their positions. The long fibers needs to be chopped into short ones before they are attached to the TEM specimen. Secondly, the heating process has to be slow in order to stabilize the electrical current and homogenize the temperature. It's desired to follow a step heating procedure before the samples are heated to the target temperature. Thirdly, beam adjustment during heating is often needed. As mentioned previously, electron beam can be interfered by the magnetic field generated by the electrical current. Adjusting the beam condition and performing beam focus from time to time.

4.2 Experimental procedure

Our experiments were carried out in a 300kV Hitachi H9500 transmission electron microscope (TEM) with a base pressure of 5×10^{-5} Pascal. Before performing *in situ* TEM, the as-spun mullite-nickel (5 wt. %) fibers were first heat treated in reduced atmosphere (5 mol. % H_2 in Ar) for 20 hours at 750°C. The obtained nanofibers were chopped using high energy sonicator in ethanol. The obtained suspension was brushed onto the heating element of the TEM heating probe. The specimen was slowly heated to 850°C. We imaged our samples with time under bright-field mode. X-ray diffraction was performed on samples that were heat treated at 750°C and 850°C for different durations. For the etched samples,

treatment in a hydrochloric acid-water (pH=2) solution was applied to remove the surface particles before the X-ray measurement. The etched samples were characterized by SEM (as shown in Appendix) to prove the removal of surface particles. High purity ZnO powder (Alfa Aesar, 99.99%, MA, USA) was used as an internal standard. The ZnO peaks (in comparison to the ZnO JCPDS peak positions) were used as an internal calibration for *2θ*. The strain was calculated from the shift between the measured and the JCPDS Ni d-space (JCPDS#: 01-070-0989) using the following equation:

$$\varepsilon = \frac{d_{hkl} - d^0_{hkl}}{d^0_{hkl}} \tag{4.1}$$

Where d_{hkl} is the measured d-space, d^0_{hkl} the standard JCPDS Ni d-space. Eq. 4.1 was applied to calculate the crystallite size of nickel nanoparticles.

4.3 Results and discussion

4.3.1 Precipitation of Ni NPs in nanofibers

Figure 4.3 shows the *in situ* TEM of mullite-nickel (5 wt.% Ni) nanocomposite heat treated at 850°C. Due to a significant density difference between nickel and the matrix mullite, the distinguished dark region is the metallic phase. We observed considerable amount of metal nanoparticles formation in the fiber matrix. The typical size of the nickel nanoparticles was well-below 20 nm. Some of those particles already formed at the initial stage, as shown in the first and second frame. However, there was no significant growth in those large particles. At the same time, more and more Ni NPs precipitated around the stagnant ones, the nanoparticles did not coalesce. The SEM micrograph (Figure 4.4 (a)) of the fiber surface did not show any nanoparticles with diameter below 20 nm, confirming that those NPs were precipitated within the fiber. Only relatively large particles (e.g. about

50 - 100 nm) were observed on the surface. The particle size evolution generated from XRD (for overall and embedded ones) and SEM (for surface ones) is shown in Figure 4.4 (c). The large NP of 50 - 100 nm observed during *in-situ* TEM were probably surface NPs.

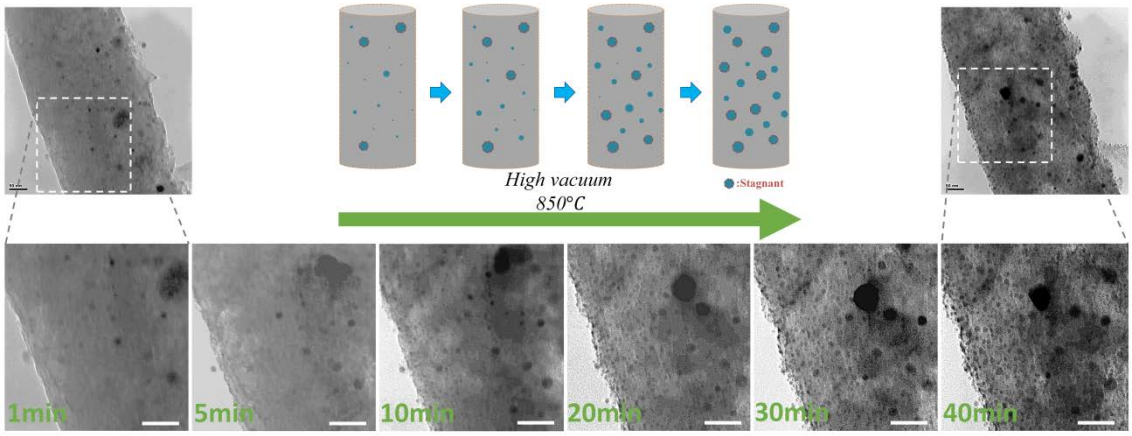

Figure. 4.3. Insitu TEM at 850°C showing the precipitation of small Ni nanoparticles (scale bar: 50 nm)

Contradicting the typical coarsening effect observed on the metal NPs at high temperatures [38, 39], we observed a very unique phenomenon that the NP growth ceased or stagnated when the NPs reached certain size. The stagnation size was about 20 nm. This phenomenon was not caused by possible insufficient diffusion length of Ni within mullite during observation, because the newly-formed NPs can be very close to the pre-existing NPs, with the distance on the same order of the NP diameters. The Ni diffusion length must be much larger than the NP diameters, because only dilute Ni was pre-existing in mullite before precipitation. All NP growths were ceased at certain sizes, which indicates that the small and lately-formed NPs did not give up Ni atoms to the previously-formed NPs.

We also observed that the precipitated NPs have a broad distribution in sizes. In classic theory, a multi-particle system containing small and large particles is not

thermodynamically stable. The cause is that interfacial equilibrium concentration for small and large particles is different according to the classic theory. In our experiment, we observed interesting phenomena showing that a system of particles of different sizes can be stable at high temperature. This phenomenon was rebelling against the classic Lifshitz-Slyozov-Wagner (LSW) theory, which predicts that smaller particles shall disappear and larger ones shall grow [234].

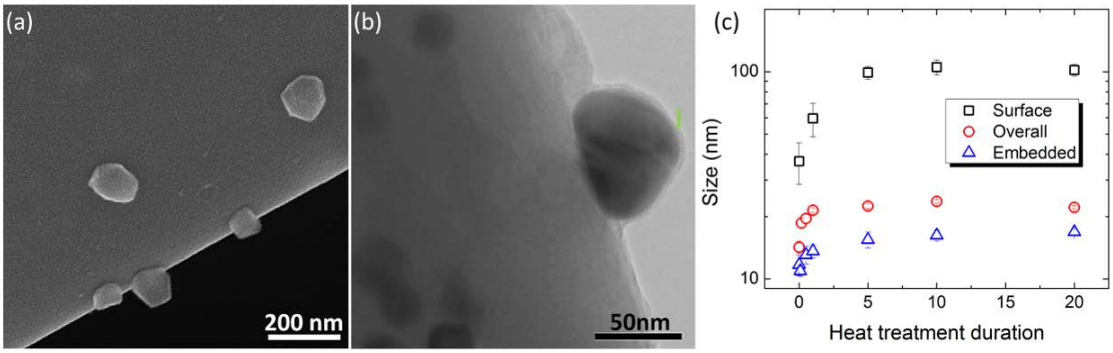

Figure. 4.4. SEM images showing (a) the formation of large particles on the surface. (b) An embedded particle close to the surface, covered with a thin layer of matrix material (as marked). (c) plot of surface, internal and overall particle size as a function of heat treatment duration. The size of internal particles was obtained from XRD after etching off the surface ones (see Appendix).

The cause of the NP stagnation should not be the interfacial energy. According to the classic theories, the equilibrium concentration (as shown in figure 4.1) is smaller for larger particles. Larger particle would have a greater driving force for growth, if the interfacial energy is the only cause of particle growth. We observed the opposite case that larger NP stopped growing while smaller ones precipitated out continuously at the initial stage. Then all the particles ceased in growth. The above observation confirms our postulation that interfacial energy is not the dominating mechanism. According to our

postulation, mechanical interactions between the matrix and nuclei is the driving mechanism leading to our observation.

Figure 4.4(b) shows the TEM image of a large particle precipitated close to the fiber's surface covered by a thin layer of matrix material. For this NP, the interfacial energy should be identical with those inside of the fiber. But the mechanical interaction between the particle and the matrix was weak when the particle is located near surface, and this NP was much larger than the internal ones. This is an evidence showing that with weak mechanical interactions, the interfacial energy drives the particle to grow into large size. We observed different particle size distributions that appeared on the surface and within the fiber (Figure 4.4(c)). The surface particles were more than five times greater than the internal particles, which in consistency with our findings in chapter 3. The above observation shows that in the absence of elastic interactions, surface particles can grow much larger.

4.3.2 Mechanical equilibrium at the interface

The problem of interactions of elastic nuclei with an elastic matrix stands at the core of materials science and solid mechanics [144]. The seminal works by Eshelby [144] put this problem at the forefront of materials science and mechanics and the appreciation of its importance is raised with the progress of nanotechnology offering different ways of making metal/ceramic, metal/metal or ceramic/ceramic nanocomposites. An important example is the analysis of stresses caused by the lattice mismatch in nanoparticles-quantum dots embedded in a matrix. These spontaneous stresses are of particular significance as the means to tailor the band-gap structures of the quantum dots in heterostructures of the

electronic devices [145]. With the recent nanotechnology developments, especially in semiconductor industry, it becomes clear that the interface separating the nanoparticle from the matrix significantly influences the stress field inside and outside the inclusion []. However, the theories overlooked the size dependence of the transformation strain. To fundamentally understand the process, theoretical analysis and experimental study of the misfit elastic strain of the Ni NP precipitated from a mullite fiber matrix is performed. The transformation strain is presumed caused by the volume dilatation from the matrix.

A. Formulation of the mathematical model

The volume misfit caused by composition change of solute can be appreciated as follows. According to the law of mass conservation, density of the matrix solution is given by:

$$\rho_m = \frac{M_m + M_{Ni}}{V_m + \Delta V} = \frac{M_m + M_{Ni}}{V_m}\left(1 - \frac{\Delta V}{V_m}\right) = \left(\rho_0 + M_W^{Ni} \cdot C_{Ni}\right)\left(1 - \frac{\Delta V}{V_m}\right)$$

$$\approx \rho_0\left(1 - \frac{\Delta V}{V_m}\right) + M_W^{Ni} \cdot C_{Ni} \tag{4.2}$$

Where M_m and V_m are the weight and volume of pure matrix material (mullite) without solute, ΔV is the volume of dilatation with respect to the reference state of zero concentration, ρ_0 the density of pure mullite, M_W^{Ni} the molecular weight of nickel, C_{Ni} the concentration of solute in the solution. In a dilute solution, it is assumed that the experimentally measured density depends linearly on concentration of the solute with a linear coefficient k:

$$\rho_m = \rho_0\left(1 - \frac{\Delta V}{V_m}\right) + M_W^{Ni} \cdot C_{Ni} = \rho_0(1 + kC_{Ni}) \tag{4.3}$$

By definition, the relation between volume change owing to the dopants concentration and the strain is given by:

$$\frac{\Delta V}{V_m} = \varepsilon_{rr} + \varepsilon_{\theta\theta} + \varepsilon_{\varphi\varphi} \tag{4.4}$$

where ε_{rr}, $\varepsilon_{\theta\theta}$ and $\varepsilon_{\varphi\varphi}$ ($\varepsilon_{\varphi\varphi}$=$\varepsilon_{\theta\theta}$ for the isotropic system) are radial and angular strains caused by addition of dopants into the mullite matrix. Combining Eq. (4.3) and (4.4), we obtain the concentration dependent misfit strain:

$$\varepsilon^* = \alpha C_{Ni} \tag{4.5}$$

where the concentration expansion coefficient α is given as:

$$\alpha = \frac{1}{3}\left(\frac{M_W^{Ni}}{\rho_0} - k\right) \tag{4.6}$$

Equation (4.5) can be used to identify the eigenstrain appearing right after precipitation of Ni NP as the relation between misfit strain and solute concentration has been discussed previously by Voorhees and Johnson [230]. Based on the system of mass conservation, the strain resulting from composition changes has a similar expression but with a second order term $(\alpha C_{Ni})^2$, which is in our case, small and neglected (as $\varepsilon^* \ll 1$) [230]. Eq. (4.5) is also similar to the form of the dilatational strain caused by thermal expansion mismatch. In our case, thermal expansion mismatch is typically on the order of 10^{-4} to 10^{-3} (the difference in thermal expansion coefficient is on the order of 10^{-6}). This transformational strain due to thermal mismatch is not large enough to induce the observed elastic strain of the particle, which is discussed later.

Assuming a fixed number of precipitated particles and neglecting the NP size distribution, the relation between compositional change ΔC (change in C_{Ni} before and after

precipitation), particle size a and number density of particles N (the number of precipitates per unit volume) is given as:

$$\Delta C = -\frac{a^3 N}{\Omega_a N_A} \tag{4.7}$$

where Ω_a is the atomic volume of the precipitates, N_A the Avogadro number. Combining Eq. (4.5) and (4.7), the misfit strain is then given as:

$$\varepsilon^* = -\alpha N a^3/(\Omega_a\, N_A) \tag{4.8}$$

According to chapter 3, the matrix material (mullite) was amorphous during NP precipitation [167]. Thus we can assume that the matrix material is mechanically isotropic. The precipitated phase (Ni) had a cubic crystal structure. It is a good approximation to assume that Ni NPs were mechanically isotropic, as well. We consider a spherically symmetric configuration with a central spherical core of radius *a*, representing the precipitated particle as shown in figure 4.5. The interface between the two phases is assumed to be coherent, which implies that the displacement field is continuous across the interface [230].

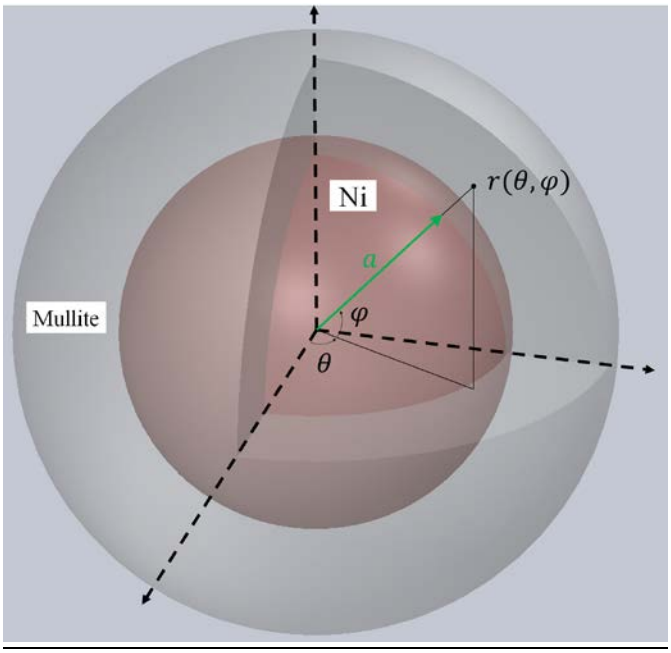

Figure. 4.5. Schematic diagram showing a spherical NP with diameter *a* precipitating in a concentric elastic spherical matrix

Our presumption is that there's no shear stress in either the particle or the matrix. For linear elastic materials under no external force, the differential equation for stress tensor $\boldsymbol{\sigma}$ is given by [220]:

$$\boldsymbol{\nabla} \cdot \boldsymbol{\sigma} = 0 \tag{4.9}$$

The above equation can be written in the spherical coordinate form. For the spherically symmetric configuration, the normal stresses σ_{rr} and $\sigma_{\varphi\varphi}$ in both particle and matrix simplifies to the following equation [220]:

$$\frac{d\sigma_{rr}}{dr} + \frac{2(\sigma_{rr}-\sigma_{\varphi\varphi})}{r} = 0 \tag{4.10}$$

The constitutive equations that relate the unknown stress and strain for elastic materials are given by the Hooke's law:

$$\begin{cases} \varepsilon_{rr} = \frac{1}{E}\left[\sigma_{rr} - 2\upsilon\sigma_{\varphi\varphi}\right] + \varepsilon^* \\ \varepsilon_{\varphi\varphi} = \frac{1}{E}\left[(1-\upsilon)\sigma_{\varphi\varphi} - \upsilon\sigma_{rr}\right] + \varepsilon^* \end{cases} \tag{4.11}$$

where ε_{rr} and $\varepsilon_{\varphi\varphi}$ represent the radial and angular strain; σ_{rr} and $\sigma_{\varphi\varphi}$ are radial and angular stress. *E* is the Young's modulus, and υ is Poisson ratio. For small displacement, it is possible to separate the elastic strain term (the first term on the right hand side) and transformation strain ε^* from the total strain [45]. The strain-displacement relations, by definition, are given as: $\varepsilon_{rr} = \frac{du}{dr}$ and $\varepsilon_{\varphi\varphi} = \frac{u}{r}$.

B. Solution to the mathematic model

Combining Eq. (10) and Eq. (11), the governing differential equation for the displacement field $u(r)$ is obtained [45]:

$$\frac{d^2u}{dr^2} + 2 \cdot \frac{1}{r}\frac{du}{dr} - 2 \cdot \frac{u}{r^2} = 0 \tag{4.12}$$

A general solution to Eq. (4.12) can be found. Note that *u*=*r* is an apparent solution to this differential equation. Let $u(r) = r \cdot f(r)$, Eq. (4.12) can be reduced into $r \cdot f'' + 4f' = 0$. Integrate twice, one can obtain $f = \frac{A}{r^3} + B$. Therefore a general solution to Eq. (4.12) has the following form: $u(r) = \frac{A}{r^2} + Br$, where *A* and *B* are both integration constants.

The interfacial and boundary conditions are given as follows. The displacement at zero coordinate (center of the sphere) is zero due to symmetry of the system. With our presumption of coherent interface, the displacement should be continuous at the interface. The external surface ($r \to \infty$) is not constrained and the elastic strain equals zero. The total

strain therefore equals the transformation strain. The boundary conditions are therefore given as (for $0 \leq r<a$, use 'p' as superscript; for $a \leq r < \infty$, using 'm' as superscript):

$$\begin{cases} u^p(0) = 0 \\ u^p(a) = u^m(a) = a\varepsilon^i \end{cases} \tag{4.13}$$

$$\frac{du^m}{dr}|_\infty = \varepsilon^* \tag{4.14}$$

where ε^i is the strain of the particle, ε^* the transformation strain. According to our assumption, transformation strain only presents in the matrix during the precipitation, since the matrix changes its composition and therefore the atomic volume of the matrix during precipitation. The interface and boundary conditions are applied to determine the integration constant *A* and *B*. A complete solution is given as:

$$u^p = \varepsilon^i \cdot r \tag{4.15}$$

and

$$u^m = \left(\varepsilon^i - \varepsilon^*\right) \cdot \frac{a^3}{r^2} + \varepsilon^* \cdot r \tag{4.16}$$

The corresponding solutions to strain and stress in the particle and matrix are given as:

$$\varepsilon_{rr}^p = \varepsilon_{\varphi\varphi}^p = \varepsilon_{\theta\theta}^p = \varepsilon^i \tag{4.17}$$

$$\sigma_{rr}^p = \sigma_{\varphi\varphi}^p = \sigma_{\theta\theta}^p = \frac{E^p}{1-2v^p}\varepsilon^i \tag{4.18}$$

and

$$\begin{cases} \varepsilon_{rr}^m = -2\left(\varepsilon^i - \varepsilon^*\right) \cdot \left(\frac{a}{r}\right)^3 + \varepsilon^* \\ \varepsilon_{\theta\theta}^m = \varepsilon_{\varphi\varphi}^m = \left(\varepsilon^i - \varepsilon^*\right) \cdot \left(\frac{a}{r}\right)^3 + \varepsilon^* \end{cases} \tag{4.19}$$

$$\begin{cases} \sigma_{rr}^{m} = -\frac{2E^m}{1+\upsilon^m} \cdot (\varepsilon^i - \varepsilon^*) \cdot \left(\frac{a}{r}\right)^3 \\ \sigma_{\theta\theta}^{m} = \sigma_{\varphi\varphi}^{m} = \frac{E^m}{1+\upsilon^m} \cdot (\varepsilon^i - \varepsilon^*) \cdot \left(\frac{a}{r}\right)^3 \end{cases} \tag{4.20}$$

According to the solutions, strain and stress in the precipitate are both constant. On the other hand, the strain and stress in the matrix are distributed over the space. The stress has maximum at the interface, and vanishes as $r \to \infty$. Meanwhile the strain approaches ε^* as r increases.

In the next step, mechanical equilibrium at the interface is applied to derive the expression for ε^i. Many of the important effects of curved surfaces/interfaces are attributed to the pressure difference caused by surface/interface energy. As for a spherical nanoparticle with radius *a*, the balance in stress is given by [45]:

$$\sigma_{rr}^{m} - \sigma_{rr}^{p}|_{r=a} = \frac{2\gamma}{a} \tag{4.21}$$

Where σ_{rr}^{m} and σ_{rr}^{p} are the radial stresses for the matrix and the particle respectively, γ is the interfacial free energy. In the first approximation, we consider γ independent of strain. Combining Eq. (4.17) to (4.21), we can conclude that the hydrostatic strain within an NP is:

$$\varepsilon^i = \left(\kappa^m \cdot \varepsilon^* - \frac{2\gamma}{a}\right) / (\kappa^m + \kappa^p) \tag{4.22}$$

where κ^m and κ^p are elastic parameters of the matrix and the particle given by: $\kappa^m = \frac{2E^m}{1+\upsilon^m}$ and $\kappa^p = \frac{E^p}{1-2\upsilon^p}$. E^m and E^p are respectively the elastic modulus of the matrix and particle. υ^m and υ^p are the Poisson's ratio accordingly. For our system, E^p and υ^p are assumed to be elastic constants of bulk nickel (200 GPa and 0.31). The matrix material is not standard as it corresponds to an aluminosilicate glass with mullite composition. The Elastic constant

of the glass was measured from tensile tests with a given value of 62GPa. The Poisson's ratio is assumed to be close to the value of bulk mullite (0.28). Through calculation we obtain $\kappa^p = 526$ GPa and $\kappa^m = 97$GPa.

And combining Eq. (4.8) the elastic strain in the particle can be derived as:

$$\varepsilon^i = \frac{-\alpha\kappa^m a^3 N/(\Omega_a N_A) - 2\gamma/a}{\kappa^p + \kappa^m} \tag{4.23}$$

Eq. (4.23) describes the dependence of strain in the precipitate on particle size a. Because there is no transformation strain in the precipitate, this strain is purely elastic. For small particle size, the elastic strain within the precipitate is dominated by the capillary term $2\gamma/a$. This corresponds to a NP having a residual spontaneous strain adapted from the fluid mechanics model of a drop with and interfacial Laplace-Young tension [44]. Such strain is compressive and the particle shrink in size. For large particle size, the dominating effect will be the transformation strain term ε^*, as it has a cubic dependence on a. The sign of α can be either positive or negative, depending on how the solute atoms incorporate into the lattice of the matrix and the resultant expansion or shrinkage of the unit cell. Therefore the transformation strain can be either positive or negative. If α is negative, the transformation strain of the matrix induces a tensile strain onto the precipitates for large particles.

C. Experimental results for the elastic state of Ni NPs

Figure 4.6 shows the d-spacing of nickel corresponding (111) lattice plane measured using XRD. We observed the trend of lattice parameter increase with particle size. The strain state of Ni transited from compressive with particle size around 11 nm, to tensile with the particle size greater than 12 nm.

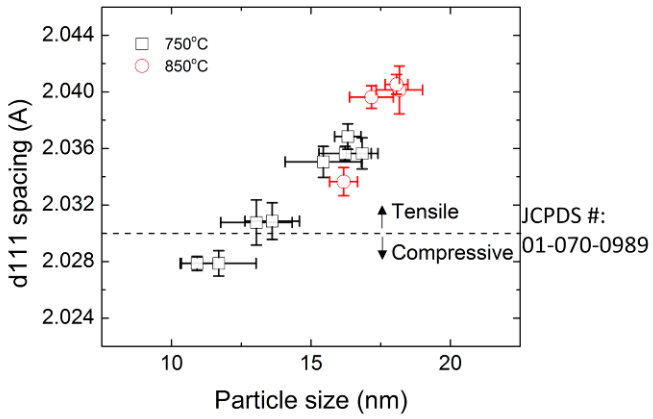

Figure. 4.6. Strain-size plot generated from XRD (The reference JCPDS d-spacing for the stress-free state was calculated from single crystal data which provides accurate information on lattice parameter).

A very interesting phenomenon was that we observed both compressive and tensile strains on the Ni NPs, depending on the NP sizes. The stresses had a very precise dependence on the NP sizes. This can be explained using Eq. (4.23). The elastic strain of the Ni NP has two contributors: the matrix dilatation and capillary compression. If a NP is not subjected to the stress caused by the matrix dilatation, the NP is always under mechanical compression. This type of stress has been experimentally reported by many studies [237, 238].

The model of a NP equipped with an interfacial layer having a residual spontaneous stress became popular as it is adapted from the fluid mechanics model of a drop with and interfacial Laplace-Young tension [44]. However, the Laplace-Young model assumes a positive interfacial energy suggesting that in equilibrium, a complex shaped object wants to minimize its surface area to take on a spherical shape. Thus, a solid nanoparticle tends to shrink in size [45, 46, 239]. The observed size dependence and sometimes the lattice expansion and not contraction is typically explained by the nanoparticle charging or

formation of a dipole surface layer which changes the interfacial energy from positive to negative [45, 240]. However, these arguments do not work with the metal nanoparticles: the surface energy of the metal nanoparticle is always positive [241]. Moreover, for a constant surface energy and elastic moduli, the radial displacement due to the interfacial energy should not depend on the particle size [45, 46]! This fact was first pointed by Rusanov [46] and then accepted by the materials scientists as the main challenge in the explanation of the size dependence of the nanoparticle strain.

D. Sensitivity of measurement with respect to interfacial energy γ

The observed d-spacing was converted into the elastic strain ε^i according to Eq. 4.1, which is shown in Figure 4.7. The elastic strain observed in the experiment, is typically on the order of 10^{-3} to 10^{-2}. According to Eq. (4.23), the transformation strain ε^* should be on the order of 10^{-2} to 10^{-1}, which is at least one order of magnitude greater than the dilatational strain caused by thermal mismatch. Furthermore, we found that the elastic strain caused by the misfit and transformation strain has a definite dependence on the NP sizes, and follows the analysis to Eq. (4. 23). Figure 4.7 (a) shows the curve fitting according to Eq. (4. 23). There are two adjustable parameters: $\frac{-\alpha\kappa^m N/(\Omega_a N_A)}{\kappa^p+\kappa^m}$ and $\frac{2\gamma}{\kappa^p+\kappa^m}$. It is difficult to find reference for the first parameter ($\frac{-\alpha\kappa^m N/(\Omega_a N_A)}{\kappa^p+\kappa^m}$) because of unknown α, the linear concentration expansion coefficient. Measuring α is difficult because the matrix material is amorphous and it's hard to measure the unit cell of the matrix solution. The number density N could be estimated from the experiment, but large error exists. As compared to the first one, the second parameter ($\frac{2\gamma}{\kappa^p+\kappa^m}$) has defined values. With

experimentally determined values of κ^m and κ^p, γ was obtained from the fitting. The best curve (R square > 0.95) was for γ = 4.30 N/m (2.85-5.75N/m). The typical value of interfacial energy between metals and oxides reported was around 1 to 2 N/m [71]. Our estimated interfacial stress is slightly greater than what was expected. This is possibly due to the increasing number density of NP. This causes an increase in the power index *m* of the size dependent strain ($\varepsilon^* \propto a^m$) contributed by matrix dilatation. For example, if the power index *m* increases from 3 to 6, the best curves correspond to interfacial energies of 3.13 (*m=4*) and 1.90 N/m (*m=6*), as shown in Figure 4.7(b). On the other hand, if the strain-size dependency ($\varepsilon(a)$) was only dominated by capillary pressure term $\frac{2\gamma}{a}$ and a transformation strain (ε^*) is not a function of *a*, the fitted curve is shown in Figure 4.7 (c). The generated interfacial energy was unrealistically large (22.6 N/m). The transformational strain was on the order of 10^{-2}, which cannot be explained by any feasible non-size-dependent dilatational strain (*i. e.* thermal mismatch strain). Therefore, the strain-size relation can be explained only by the size-dependent volume misfit, caused by the matrix dilatation.

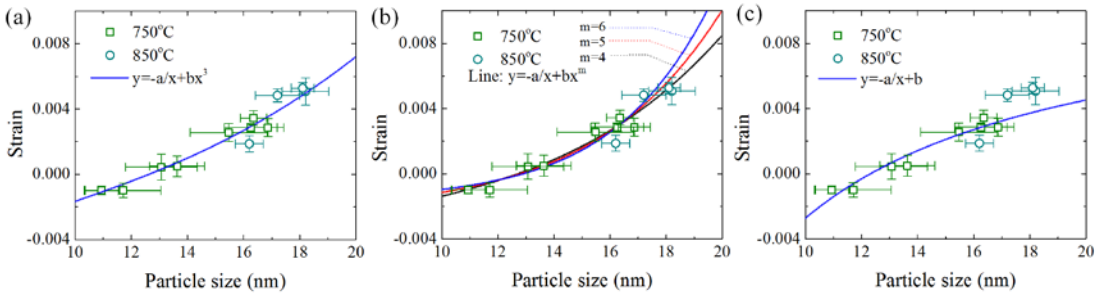

Figure 4.7. (a) Fitting curves using Eq. (4.23) with different values of interfacial stress; (b) It is possible to have a higher power index of misfit elastic strain on the particle size (c) Assuming the NP elastic stress was solely contributed by surface stress, the curve cannot fit the experimental data.

Su and Voorhees pointed that two particles of same radius and fixed morphology can be stable with respect to coarsening due to the energetic considerations [227]. However, we observed a multi-particle system with different particle sizes can be stable as well. The uniform and flat concentration in the matrix can be well explained by the mechanical model. That is to say, both small and large particles have the same equilibrium interfacial concentration, which levels with the far-field concentration. The concentration that is strongly coupled to the mechanical equilibrium at the interface, gives rise to the new phenomenon observed in ceramic-support metal NPs system. Such mechanism in NPs growth stagnation can be practically applied for stabilizing NPs at high temperatures.

4.4 Conclusion

In this chapter, we theoretically analyzed the misfit strain of the NP precipitated from a matrix material, caused by the dilatational transformation strain in the matrix. We used *in-situ* TEM to observe the precipitation process of nickel nanoparticles within a ceramic matrix solution containing supersaturated solute (Ni) atoms. We found an astounding phenomenon that NP stopped growing at certain size, while the smaller NPs continuously precipitated out closely around the stagnant NPs. Then the growth was stagnant for all the particles. We found that this misfit strain had a strong and high order dependence on the NP sizes during the precipitation. Depending on the NP sizes, the predicted strain could be compressive as well as tensile. We theoretically explained this phenomenon that the elastic strain confining mechanism was caused by the matrix dilatation. A continuum mechanics model was developed to demonstrate the relation between particle growth and elastic strain evolution, which evidenced with the XRD

results. The elastic strain increases as particle grow, which leads to the transition from the compressive state (contributed by interfacial stress) to the tensile state (contributed by dilatation). The misfit strain has strong dependence on the particle size. The power index was confirmed by matching reasonable values of interfacial energy. The resulting elastic strain is the dominating mechanism for the particle confinement.

CHAPTER V

DEVELOPMENT OF THE DEFECT-FREE MULLITE CERAMIC FILMS

5.1 Introduction

As for our central goal of processing dense and defect-free ceramic films embedded with magnetic nanofibers, the ceramic thin film itself needs to be crack-free. In the coating process, the condensation during drying and decomposition upon heat-treatment can greatly affect coating formation. The capillary and coherent forces during these processes are the driving forces for densification of coatings. On the other hand, the intrinsic stress caused by the shrinkage, if exceeds the material's limit, results in uncontrollable cracking and decohesion. It is difficult to prevent cracking due to the stress, especially for thick films [47, 48, 149-153]. The maximum film thickness of non-repetitive deposition above which the cracking occurs is often termed as "critical thickness" (τ_c). For sol-gel derived ceramic coatings, the τ_c value is typically below 100 nm [49, 50]. This value is insufficient for our application since it's smaller than the diameter of many fibers or rods (e.g. electrospun fibers in chapter 2 and 3). Many attempts have been made to increase the critical thickness, such as using additives with chelating ligands (*e.g.* acetylacetone), or high molecular weight solvents and/or organic polymers [149-153]. The polymers are soft and more ductile than ceramics. Such polymers as polyethylene glycol and polyvinylpyrrolidone (PVP), were used as the additives to prevent cracking [153, 154]. Elimination of cracks seems to be achievable using the hybrid sol-gel precursor with polymers. On the other hand, the factors that determine the crack resistance of the materials needs to be explored with more details. For example, many polymers decompose at intermediate temperatures of 200 to

400°C. What is the role of thermal stability of polymers when cracking occurs at those intermediate temperatures?

The purpose of this study is to explore the effect of polymer additives on the critical thickness of mullite films obtained from monophasic sol-gel precursors. It is desirable to have the dense, crack-free, thick and coherent mullite film for corrosion protection. A monophasic precursor has the advantage of low processing temperature and excellent single phase purity. It is interesting for ceramists to understand the low temperature processing of dense crack-free mullite film, using the monophasic precursor with the addition of polymers as structural modifiers.. In this chapter, we used the cracking onset temperatures and critical thickness to demonstrate the effects of polymer additives on preventing cracking.

5.2 Experimental procedure

Mullite films were processed from the same precursor. Sol MS7 from Table 2.1 was mixed with polyethylene oxide (PEO, M_w 1,000,000 Da, Sigma-Aldrich, MO, USA), polyvinyl alcohol (PVA, M_w 85,000-124,000 Da, Sigma-Aldrich, MO, USA), or polyvinylpyrrolidone (PVP, M_w 1,300,000 Da, Sigma-Aldrich, MO, USA) with different weight ratios in a mixed solvent containing 75 wt. % Ethanol and 25 wt. % H_2O using a high intensity ultrasonic processor (Vibra Cell VC 500, Sonics, CT, USA). The mullite yield of the solution was kept at 5 wt. % (for polymer weight < 50% of ceramic yield) and 2.5 wt. % (for polymer weight $\geqslant$ 50% of ceramic yield) in order to maintain an appropriate same viscosity of the solution. The film substrates (silicon wafer: 750μm in thickness, 2cm ×1cm×0.5mm single-side polished, purchased from UniversityWafer, Inc.) were cleaned

in acetone followed by plasma cleaning （pdc-32g, Harric Plasma, NY, USA） for 5 minutes. The obtained solution was used for dip-coating at ambient temperature with a relative humidity level of 50-60%. Different withdrawal velocities, ranging from 0.02 to 0.25 inch/second, were applied during dip-coating process, to obtain films with different thicknesses. The films were dried for 24 hours in desiccator at room temperature before heat treatment. The films were heated in air at 5 °C/min and sintered at 1000°C and 1200°C for 2 hours.

The film thickness measurement was carried out using atomic force microscopy (AFM, Dimension 3100 AFM, Veeco Inc, Plainview, NY, USA). Before the heat-treatment, a scratch through the film was applied to the film using a sharp blade. The thickness was determined by scanning the profile across the scratch and calculating the depth of the scratch. To determine the cracking onset temperature, the samples were heated to a targeted temperature, and then observed under an *in-situ* optical microscope, before they naturally cooled down to room temperature. The samples were marked as cracked or none-cracked depending on whether film cracks were observed. The temperature of the furnace was calibrated using a K-type thermocouple so that certain deviation in temperature reading is estimated (indicated by the error bar). The critical thickness is determined from the maximum thickness of crack-free film after heat-treatment at 1000°C.

5.3 Results

Figure 5.1 shows the TGA curves of the polymer additives used in this study. Different onset temperatures of decomposition were observed. Rapid mass loss in PEO was

observed from 200°C to 300°C. Steep weight loss in PVA was observed at 250 - 300°C followed by a mild loss rate at 300 - 500°C. PVP showed two stages in mass loss. The first stage was from room temperature to 100°C due to vaporization of absorbed moisture. The second stage was at 300 - 600°C, with steep mass loss at around 375°C.

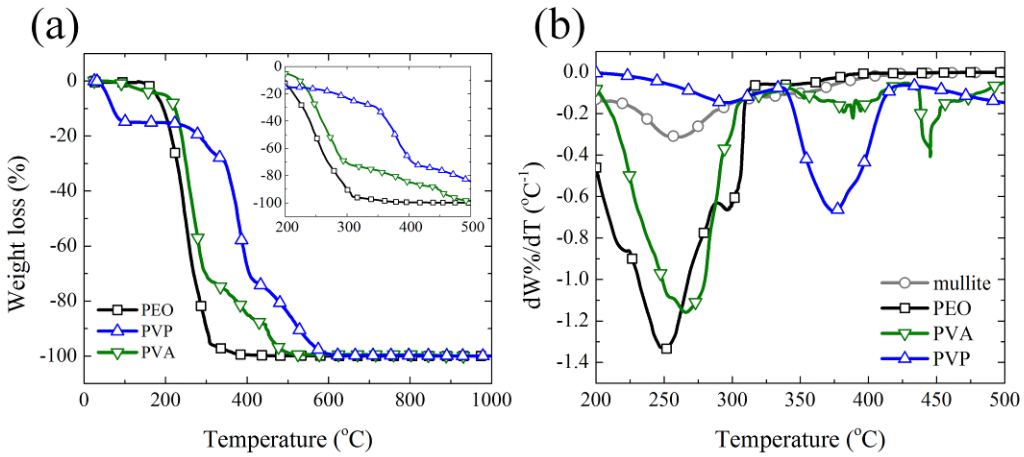

Figure 5.1. (a) TGA scans for PEO, PVP and PVA heat treated in air. (b) Weight loss rate (dW%/dT) of PEO, PVP, PVA and mullite.

The FTIR spectrum of mullite gel and mullite-polymer mixtures heat treated at low temperatures (80 - 500°C) is shown in Figure 5.2. The spectrum of pure mullite gel after drying at 80°C exhibited broad peaks at 2600-3700 cm^{-1} which was due to the OH stretching mode [190]. During the heating process, hydroxyl groups (bending mode, 1650 cm^{-1}) disappeared because of solvent evaporation, hydrolysis and condensation [242]. The strong peak located at around 1388 cm^{-1} was caused by the -NO3 vibration [191]. A weak peak at around 1170 cm^{-1} corresponds to the carbonaceous matters in the material [190]. During the initial stage of pyrolysis, the peaks corresponding to stretching of SiO4 tetrahedrons (1186, 1110 and 1050 cm^{-1}) and stretching of AlO4 tetrahedrons (960 and 830 cm^{-1}) have increased relatively comparing to the other two peaks at 1650 and 1388 cm^{-1}

[243]. The vibrations were diminished at higher temperature (500°C) due to the formation an amorphous aluminosilicate network [244]. The FTIR spectra of mullite-polymer hybrid gel (weight ratio: polymer: 50 wt. % of mullite yield) are shown in Figure 5.2 (b) - (d). The bands due to absorption of polymers overlap with the bands of mullite which results in broad peaks. The vibration band at 1710 cm^{-1} was observed in all of the hybrid gels after heat treatment at 300-400°C, which is assigned to the C=O stretching mode [244, 245]. Those peaks gradually vanished during the heating process at higher temperatures. The spectrum profiles of all the mullite-polymer mixtures are close to the mullite gel after firing at 500°C, which indicates the completion of thermal decomposition. This is in consistency with the TG analysis.

The XRD traces of mullite-PVP (50wt. %), mullite-PEO (50wt. %) and mullite-PVA (50wt. %) hybrid gel after heat treatment at 1000°C for 5 minutes are shown in Figure 5.3. These gels retain monophasic character and mullite was the only phase observed after heat treatment at 1000°C.

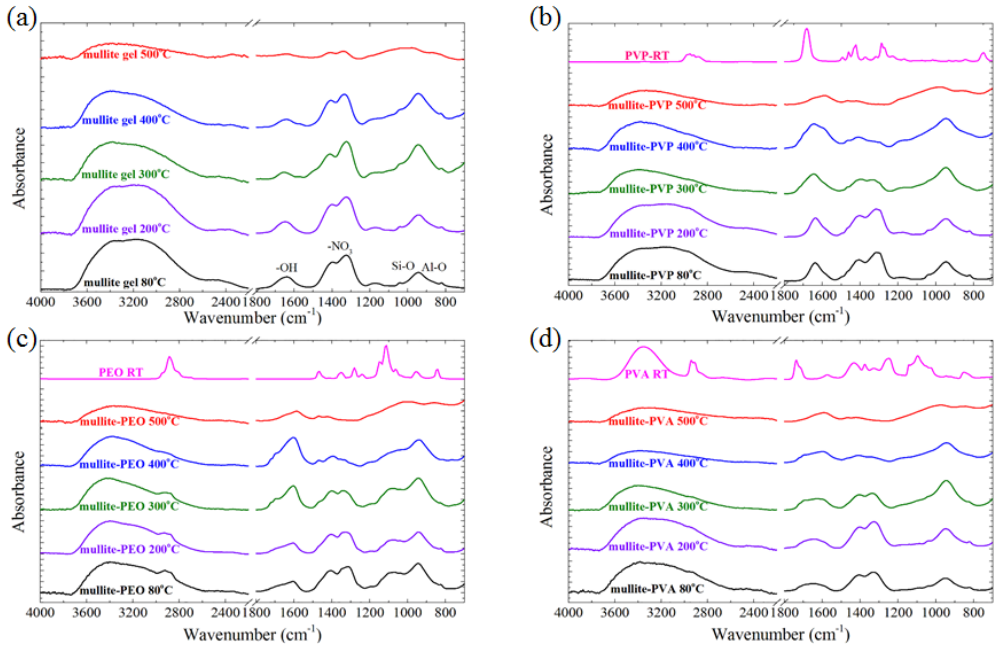

Figure 5.2. FTIR spectrum of (a) mullite, (b) mullite-PVP , (c) mullite-PEO and (d) mullite-PVA hybrid gel after heat treatment at 80(drying), 200, 300, 400 and 500°C. The polymer contents are 50 wt. % of mullite yield.

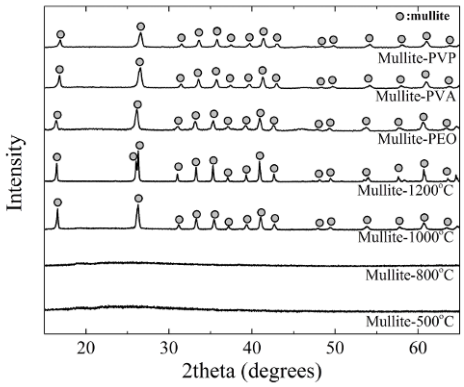

Figure 5.3. XRD patterns of mullite gel and mullite-polymer hybrid gels after firing at different temperatures. The mullite-polymer hybrid gels were heat treated at 1000°C.

In pure mullite samples with the as-dip-coated gel film of 1 μm thickness, cracking occurred after dried at room temperature which resulted in isolated fragments on the

surface, which is shown in Figure 5.4 (a). After heat-treatment at 1000°C, the isolated segments shrink extensively, as shown in Figure 5.4 (b). The free in-plane shrinkage leads to significant crack opening. Figure 5.4 (c) shows the mullite-PEO (5 wt. % PEO of mullite yield) hybrid film with the same gel film thickness of ~1 μm after firing at 1000°C. The film did not crack at room temperature before firing. Significant less crack density and gap were observed. Figure 5.4 (d) shows the elimination of cracks in thinner films with thicknesses of 600nm (measured before heating, with ~ 40% reduction in thickness after calcining). The crack spacing was also reduced. Figure 5.4 (e), (f) and (g) show the surface images of crack-free mullite-PEO, -PVP and -PVA (polymer addition amount as 50wt. % of mullite yield) thin films after heat treatment at 1000°C. High resolution SEM images of the corresponding films were also shown in the internal frames. Smooth surfaces were observed in both sole mullite gel films and hybrid films. The grain size grew to ~ 10 nm after the films were heated treated at 1000°C.

We presume that the final films obtained at 1000°C were dense or close to dense. In chapter 2, we measured the mechanical performance of the mullite fibers obtained using the same precursor, and heat-treated at 1000°C. The strengths and moduli the mullite fibers were exceptional. We assume that if the films in this study had the same shrinkage as the mullite fibers, the films were dense or close to dense. Some indirect evidence also showed that the films obtained were dense. For instance, the SEM images show that there were no pores on both surface and cross-section. However, direct density measurement on films is difficult to be performed.

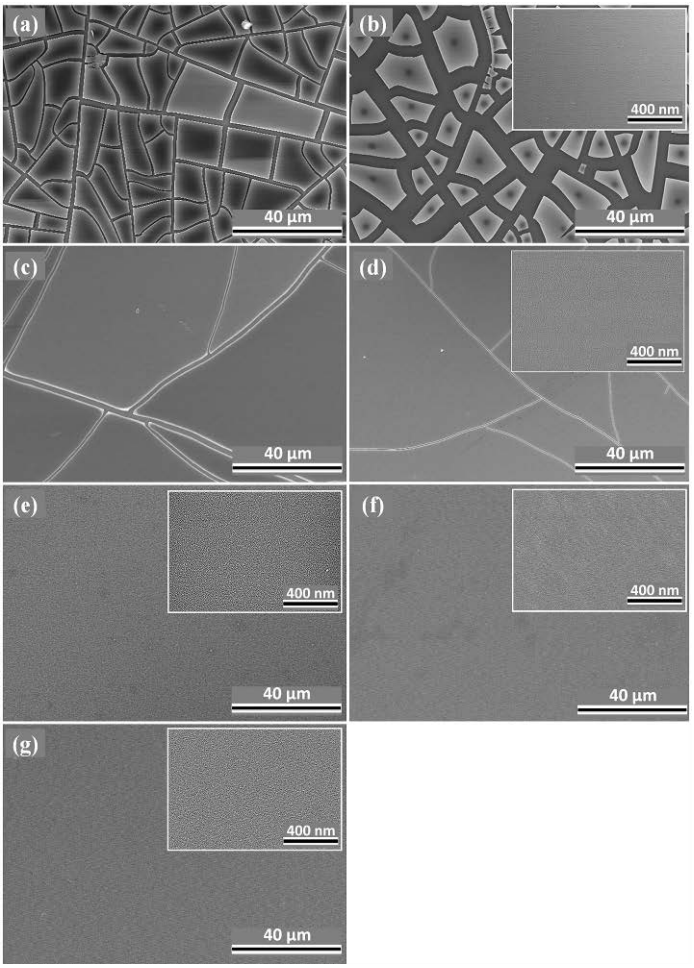

Figure 5.4. SEM images showing the microstructure of the mullite gel and hybrid films: (a) cracked mullite gel film (~1µm**) (b) cracked mullite thin film (~1µm**), (c) cracked mullite-PEO (5%*) thin film (~ 1µm**), (d) cracked mullite-PEO (5%*) thin film (~ 600 nm**), (e) crack-free mullite-PEO (50%*) thin film (~ 250 nm), (f) crack-free mullite-PVP (50%*) thin film (~450 nm) (g) crack-free mullite-PVA (50%*) thin film (~ 300 nm). (*: The percentage of polymers is determined by the polymer weight divided by the mullite yield. **: The thickness values are characterized as the gel film thickness before heat treatment. The high resolution images of materials' surface were shown in the internal frames.

Figure 5.5 shows the SEM images of mullite films (thickness ~ 200 nm) without addition of polymers after heat treatment at 500, 1000, and 1200°C. The surfaces of both the films before and after heat-treatment are smooth. Mullite with fine grain size was observed after

sintering at 1000°C. Significant grain growth occurs after sintering at 1200°C for 2 hours. An average grain size of ~120 nm was estimated from the SEM micrographs.

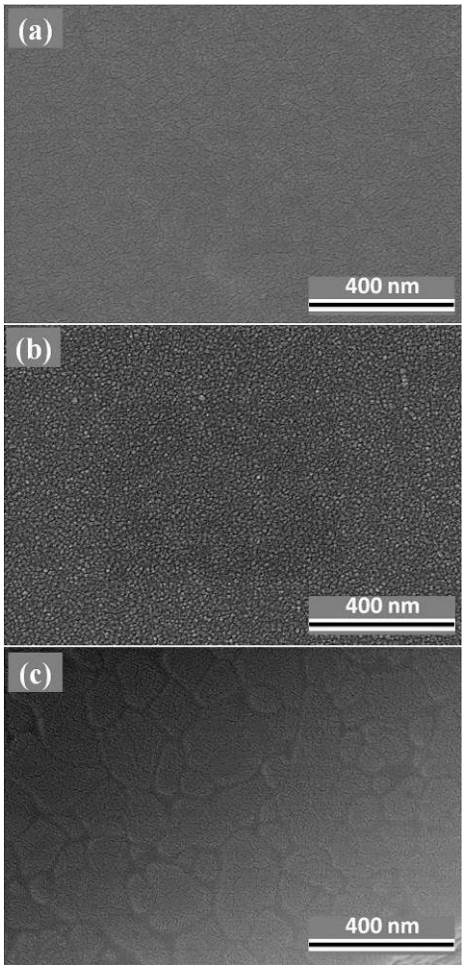

Figure 5.5. Surface micrographs of mullite thin films (thickness ~ 200 nm) (a) fired at 500°C (b) after firing at 1000 °C (C) after firing at 1200 °C for 2 hours.

The relationship between the initial film (or gel film) thickness and the cracking onset temperature observed during heating is shown in Figure 5.6 (a). Here we choose PEO and PVP for study because the thermal behavior of these two polymers are significantly different from each other. Cracking was typically observed at relatively low temperatures (below 400°C). No further cracking at higher temperatures was observed if the films did

not crack at 500°C. Thick films tended to crack at low temperatures. The addition of polymers improves the cracking onset temperatures and the final thickness of crack-free films. The cracking onset temperature-thickness profile of mullite-PEO hybrid film resembles that of the mullite-PVP films at low temperatures. However, the latter one has remarkably increased crack-free thickness at temperatures above 300°C.

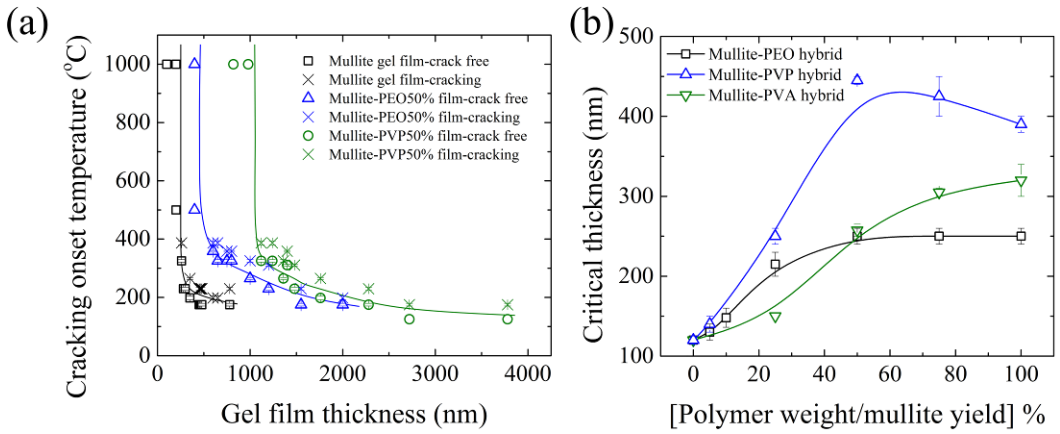

Figure 5.6. (a) Cracking onset temperature in mullite gel, mullite-PEO 50% and mullite-PVP 50% hybrid film (PEO: 50 wt. % of mullite yield and PVP: 50 wt. % of mullite yield) versus the gel film thickness*. (b) Effect of polymer content on the critical thickness** of the hybrid films. (*: the thickness value is determined before firing; **: the thickness value is determined after firing).

The measured critical thickness of the films after firing versus polymer content is shown in Figure 5.6 (b). The critical thickness for pure mullite films was only 120 nm. With addition of polymers, τ_c increases significantly. However, it does not increase monotonically with continuous increase of polymer content. The τ_c values reached a plateau with polymer content at around 50 wt. % for PEO-doped films, and at around 100 wt. % for PVA-doped mullite films. Slight decreases in τ_c were observed in PVP samples with polymer loading higher than 50 wt. %.The largest critical thickness obtained was 450 nm for the mullite-PVP film.

5.4 Discussion

In our study, no further cracking was observed at temperatures above 400°C, indicating that thermal mismatch between the ceramic film and substrate did not significantly contribute to cracking. The cracking was mainly caused by the solvent evaporation during drying, the decomposition of polymer of organic component, and the densification during heat-treatment, all of which lead to film densification [148]. After the decomposition was complete and mullite phase was formed, thermal expansion coefficient of mullite and substrate (silicon) are both on the order of 10^{-6} °C^{-1} [246, 247]. The strain caused by the thermal mismatch is on the order of 10^{-4} at high temperatures, which is much smaller than the strain induced by the volumetric shrinkage due to solvent evaporation, sol-gel polycondensation and organic decomposition. During drying the stress relaxation can be achieved by the viscous flow of polymers and the suppression of sol-gel polycondensation reaction. Adding polymer to the solution can help suppress cracking during drying. During firing, continuous densification process occurred due to the polycondensation reaction. After hydrolysis the main condensation reactions in mullite can be described as the following [242]:

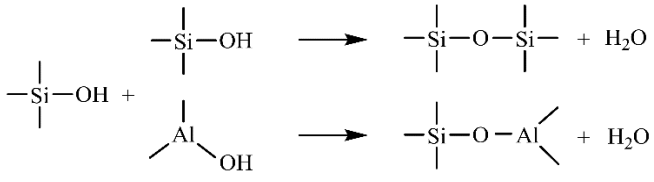

and,

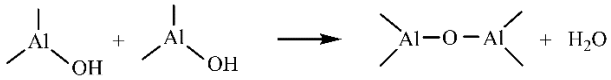

The carboxyl group can react directly with the aluminosilicate sol to form a hybrid structure of metal-organic structure through the following chemical reaction [248]:

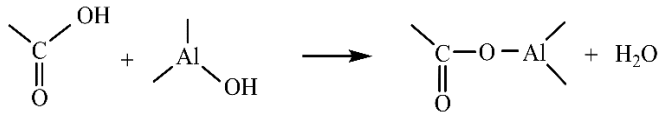

and,

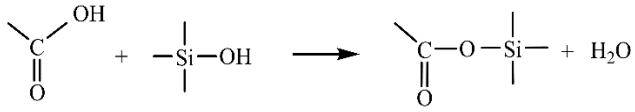

The polycondensation of mullite gel was delayed because of the chemical reactions between metal hydroxyl groups and organic ligands of the polymers [244]. Such organic ligands as carboxyl groups already presented in PVP, but not in PEO and PVA. These carboxyl groups were formed during oxidation at elevated temperatures in the samples with PEO and PVA additives [244, 249]. In Figure 5.2, the FTIR results showed the formation of C=O bonding at around 300 - 400°C in PEO and PVA. However, PVP has better thermal stability at this temperature (Figure 5.1), making it more effective in suppressing sol-gel polycondensation reactions than the other polymers. Additionally, metal ions would coordinate with N or O ions in PVP [250]. As the organic components of the gel and polymer decomposed, the solid became rather elastic than viscous, and thus internal stress built up within the film. Large tensile stress, when exceeded the material's limit, caused the failure of the film. At high temperatures, the intrinsic stresses relaxed due to diffusion.

Cracking at room temperature during drying can be effectively inhibited, even with addition of small amount of polymers. For instance, with the addition of 5 wt. % PEO of the mullite yield, the hybrid films were crack free during drying for the gel film thickness

up to 2.5 μm. Further increasing in polymer contents gave rise to even better cracking-resistant performance until an optimal concentration was reached. Although initially adding polymer resulted in greater critical thickness, an excessive amount of polymer could decrease the critical thickness, as shown in Figure 5.6 (b). The reason is that majority of the gel volume was replaced by polymers, resulted in discontinuous oxide matrix after decomposition. The excessive porosity resulted in large intrinsic stress during densification driven by the capillary force.

The cracking onset temperatures for mullite and mullite-polymer films shown in Figure 5.6 (a) indicates that cracking mainly occurred at low temperatures (< 400°C) and even at room temperature. The FTIR spectrum shown in Figure 5.2 confirms that changes in chemistry due to pyrolysis were mainly observed at temperature below 500°C. It has been suggested that a stress-relaxation polymer is effective in suppressing the stress evolution as long as it remains in films, but not effective when it is decomposed [148]. Therefore the thermal stability of the polymers greatly affects the critical thickness of the hybrid films. A greater critical thickness was found in mullite-PVP hybrid films, with a same polymer content. This can be explained by the fact that PVP is thermally more stable than PEO and PVA, which is revealed by the TGA result. In Figure 5.6 (a), the cracking onset profile of mullite-PEO resembles that of the mullite-PVP films at temperatures below 200°C. The addition of PEO significantly improves the cracking onset thickness, especially at lower heat treatment temperatures. Large deviation in the curves was, however, observed at temperatures above 250 °C. This is in coincidence with thermal decomposition temperature of PEO, which is between 200 and 300°C. While PVP is thermally stable up

to 300°C. The difference in cracking onset temperature and thickness could therefore be explained by the difference in thermal stability of the polymers.

The critical thickness achieved in this study is compared with the reports in di-phasic mullite gel systems [74, 155]. The processing of mullite thin films using sol-gel technique is summarized in Table 5.1. In the di-phasic systems, relatively large critical thicknesses of above 1 μm, or even 3-5 μm, were obtained for mullite films [155,158]. However, the film was coated on an uneven porous substrate, which is significantly different from our approach. In monophasic system, which is reported in this work, critical thickness can be improved by incorporating polymer additives. However, the critical thickness value was comparably less than the obtained in diphasic systems. A significantly larger residual mass in diphasic gel system could be the reason. The weight loss in diphasic gel systems was about 17-26%, was, however, above 50% in monophasic system. In addition, condensation reactions in monophasic gel systems are more prominent, which generates large elastic stress during drying and firing [74]. Nevertheless, there are attractive advantages of using monophasic precursor over diphasic precursor. The first is the elimination of intermediate phases, such as γ-Al_2O_3 and spinel as stated in chapter 2. The second is due to the low crystallization and sintering temperature, ensuring good grain size control. Enormous grain growth was often observed in diphasic precursor derived mullite during sintering at elevated temperatures, giving rise to the formation of mirometer sized grains [155,158]. The large grain size may profoundly affect the mechanical properties of the films as it reaches the magnitude of the film thickness [251]. On the other hand, nanocrytalline thin films are demanded for a lot of applications [252]. Especially for the

generation of composite thin films embedded with nanorods, a nanocrystalline thin film with grain size smaller than the nanorods dimension is desired, to avoid segregation of the nanorods at the grain boundaries of the film matrix. The thickness of crack-free thin films can be further improved by repetitive deposition.

Table 5.1. Mullite films prepared from monophasic and diphasic precursors ([a]: some cracking observed at the edge of the substrate; [b]: the film was coated on a porous substrate)

Precursor type	Starting materials	Weight loss	Critical thickness		Intermediate Phase	Grain size	Sintering temperature
			Without polymer	With polymer			
diphasic [155]	TEOS +boehmite	17%	<1 μm	1-2μm[a]	Yes	0.5-5μm	1280°C
diphasic [158]	TEOS +AN	26%	3-5 μm[b]	NA	Yes	3-5 μm	1300°C
monophasic (this work)	AIP+AN +TEOS	56%	0.12 μm	0.46 μm	No	< 120 nm	1000-1200°C

5.5 Conclusion

In this chapter, we used mullite films prepared from the monophasic sol-gel precursors as an example system to study the effects of polymer additives on the film's critical thickness. The critical thickness was improved with addition of polymers, such as PVP, PEO, and PVA. These polymers had optimal concentrations for improving the critical thickness of the mullite films. PVP has been demonstrated as the most effective crack-preventing agent among these polymers. This was due to the combinatory effects of PVP's capabilities of forming a hybrid gel precursor that slowed down the sol-gel polycondensation reactions, relaxing the stresses during heat-treatment, and preventing cracking over a wide thermal decomposition temperature range. If the polymer decomposes within a narrow temperature region, it has limited capability of stress relaxation. The crack-

free, dense and smooth, phase-pure mullite films with thickness of about 450 nm were achieved at low firing temperature of 1000°C.

CHAPTER VI

PROCESS NANO- AND SUBMICROMETER MAGNETIC FIBERS AND RODS OF CONTROLLED ORIENTATIONS

6.1 Introduction

Aligning magnetic nanorods or nanofibers is one of the state-of-art technologies for advanced nanocomposites [159, 160, 161]. As stated in chapter 1, the macroscopic orientation of nanorods and nanofibers remains great challenges. In this chapter, we present two methods of processing nano- and submicrometer magnetic fibers or rods of controlled orientations. Two types of magnetic fibers or rods were used. They are SiC-Fe_3O_4 rods (short fibers) and mullite-nickel nanocomposite fibers (continuous fibers).

SiC nanorods demonstrate outstanding semiconducting, optical, field emission, thermal and mechanical properties for applications in high-power, high-frequency and high-temperature [253, 254]. Substantial improvements in room and high temperature fracture toughness have been reported in many SiC-nanorod-reinforced ceramics, such as alumina, ZrB_2 and mullite [255-258]. SiC nanorods with similar thermal expansion properties, are indicated to improve the toughness of mullite at high temperature [257, 258]. Preparation of mullite-SiC nanocomposites has been reported in the literature [259-262]. Nevertheless, processing ceramic thin films embedded with aligned magnetic nanorods have not been achieved. Hereby as the first report, we demonstrate the alignment of magnetically functionalized SiC nanorods obtained from magnetic assembly. Magnetic nanofibers or nanorods can be aligned in polymer solutions under externally applied magnetic fields [13, 23]. When the motion of nanorods are constrained two dimensionally

(e.g. in a thin film), the criterion for alignment can be derived from theoretical approaches [23]. The distribution function theory explains the alignment of ferromagnetic nanorods in solidifying polymer films [87]. However, the criterion for aligning superparamagnetic nanorods remains unclear. A theoretical model is developed here to explain the orientational distributions of superparamagnetic nanorods under different magnetic field.

In the second approach, we demonstrate the orientation of mullite-nickel nanofibers achieved using electrospinning. The finely dispersed nickel NPs loaded within the aligned nanofibers are especially attractive as Faraday rotators and microwave absorbers [12-14]. The orientation of electrospun fibers is difficult to achieve because the fibers are light and wavered by small external forces. A small perturbation in the processing parameters could result in significantly different order of orientations. To be specific, many experimental parameters shall be optimized in order to achieve the orientation. This often requires a short collection distance, a field-assisted alignment setup (Figure 1.3), low feeding rate and applied voltage. The environmental parameters, such as relative humidity and temperature, should be accurately controlled. Uncontrolled environmental parameters often results in non-reproducible results.

6.2 Experimental procedure

6.2.1 Thin film embedded with magnetic short fibers

The experimental protocol for preparation of mullite films embedded with SiC-Fe_3O_4 nanorods is schematically shown in figure 6.1. SiC nanorods were coated with Fe_3O_4 nanoparticles on the surface. The SEM image of a single magnetic nanorod is shown in figure 6.2 (image provided by Dr. Luzinov's group, Department of Materials Science and

Engineering, Clemson, SC [263]). Those magnetic nanorods were dispersed in a methanol-polyethylene oxide (PEO, M_w = 1,000,000 g/mol, Sigma Aldrich, St. Louis, MO) solution at 2 wt. %. The dispersion was provided by Dr. Luzinov's group [263]. In the first step, SiC-Fe_3O_4 nanorods were deposited on a substrate from the methanol-PEO solution. The polymer thin films were fabricated using the dip coating method. The silicon wafers were cut into 1×4cm rectangles. The wafers were cleaned following the same procedure in section 5.2. The silicon wafers were dip coated at a speed of 5.4 mm/sec. Next, the dip coated wafer was immediately transferred and dried in a glass vial between two parallel neodymium magnets (K&J Magnetics, Pipersville, PA). The nanorods were oriented under the static magnetic field during the solidification of the liquid films. After drying, the obtained samples were heat treated to 750°C at 0.5°C/min in air in order to remove the polymer films. Before deposition of ceramic gel films, the samples were treated by plasma cleaning (pdc-32g, Harric Plasma, NY, USA) for 5 minutes. Integration of mullite films was processed by dip-coating the sol-gel derived solution containing 2.5 wt. % mullite yield and 1.25 wt. % PVP (as described in chapter 5). Different withdrawal velocities from 0.17 to 5.4 mm/sec to obtain ceramic films with different thickness. The films were dried for 24 hours in desiccator at room temperature before heat treatment. The films were heated in argon at 5 °C/min and calcined at 1000°C for 2 hours. Repetitive depositions were applied in order to generate the multilayered structure. The direction of applied magnetic field was reconfigured (e. g. rotation by 90°) to generate different orientations within each layer.

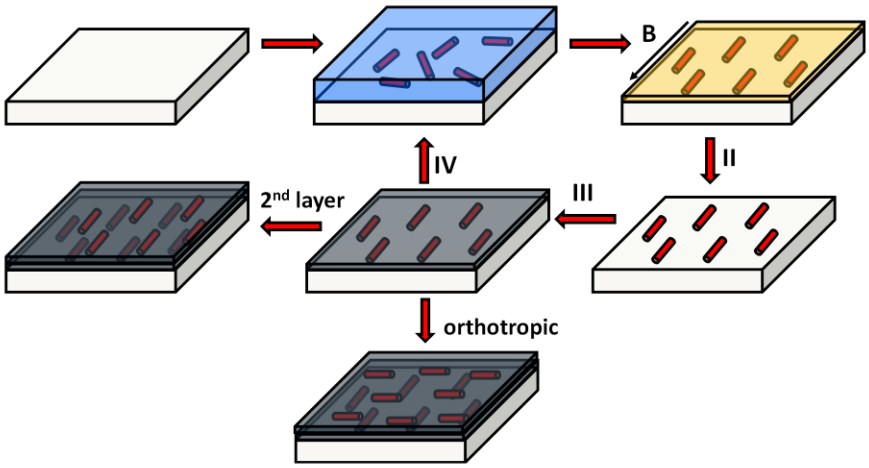

Figure 6.1. Schematically showing the experimental approach

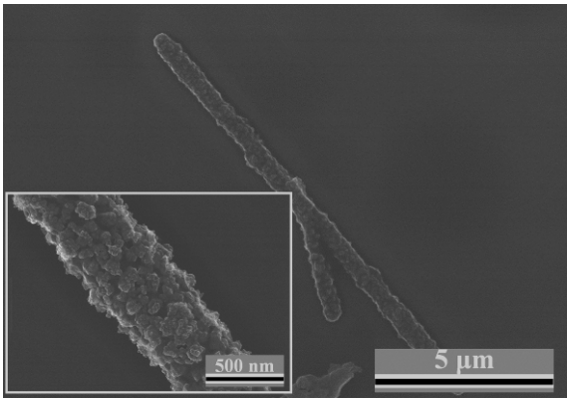

Figure 6.2. SEM image of a silicon carbide nanorod decorated with Fe_3O_4 magnetic nanoparticles

6.2.2 Thin film embedded with magnetic long fibers

The developed experimental protocol is schematically shown in Figure 6.3. The configuration of e-spinning setup was developed in ref. [113]. Following chapter 3, fibers were electrospun from the solution containing 5wt. % Ni (of mullite yield) and collected by four parallel aluminum plates. The aluminum plates were grounded with a small gap (2cm) between them. The orientation was improved with the specific plates' geometry due

to the opposite directions of electric field near the plates [113]. As a result, the charged fibers align perpendicular to the plates. The aligned fibers were collected on silicon wafers. This step can be repeated to create different orientations within each layer of collection (Figure 6.3 (b)). The obtained samples were further heat treated in reduced atmosphere for the magnetic functionalization, according to the procedure developed in chapter 3. The obtained samples were treated by plasma cleanser (following the same procedure in chapter 5) before the deposition of ceramic gel films. Then the specimens were dip-coated from the same sol-gel derived solution in section 6.2.1. The obtained films were heated in argon at 5 °C/min and calcined at 1000°C for 2 hours.

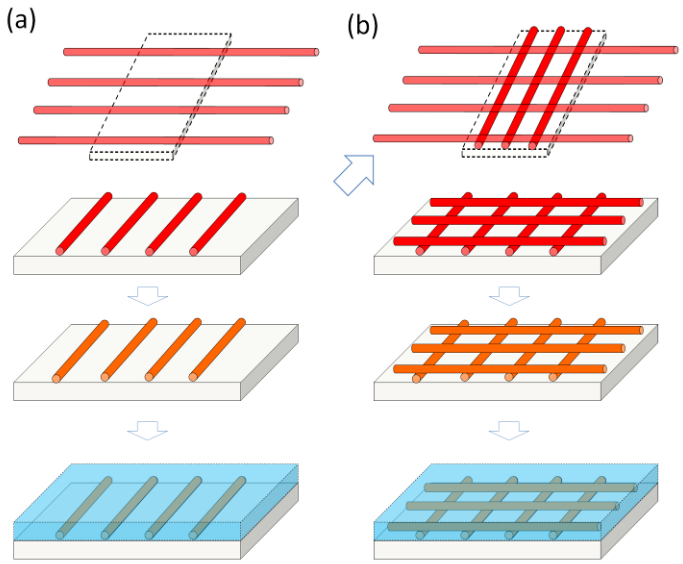

Figure 6.3. Schematically showing the workflow for processing single layer composite thin film with nanofiber oriented in (a) one direction and (b) two orthogonal directions. (The setup for electrospinning is shown in figure 1.3).

6.2.3 Characterization

The materials microstructure were characterized by optical microscope, SEM and AFM. Experimental histograms (orientation) were constructed by counting the number of

nanorods present in sectors of 10° and normalizing it by the total number of nanorods. Orientation angles for more than 500 nanorods were counted for generating each diagram. The generated distribution function was fitted to theoretical calculation according to the same method described in ref. [160]. Magnetic properties of the free-standing nanocomposite membranes were measured by using the Alternating Gradient Magnetometer (AGM 2900, Princeton Measurements Inc., NJ, USA) at room temperature. Direct magnetic measurement on the films coated on substrates is difficult due to the limited amount of magnetic material. Free-standing membrane was obtained by depositing composite thin films on a decomposable substrate (graphite). The substrate was removed by heating in air.

6.3 Results and discussion

6.3.1 Orientation of superparamagnetic nanorods in films with constant viscosity

Modeling kinetics of ferromagnetic nanorods orientation in drying or curing polymer coatings has shown that the nanorod alignment can be achieved [87, 160, 161]. For the first time, a theoretical model developed in this work explains the orientational distributions of superparamagnetic nanorods under different magnetic field. In the first place, nanorods were assumed to be confined within the plane of the liquid layer. During the rotational alignment of the magnetic nanorods subjected to an applied magnetic field, a torque defined by the cross-product of magnetization and magnetic field was applied to the superparamagnetic nanorods, which overcomes viscous drag from the polymer solution. We define φ the angle between nanorod orientation and the direction of the

applied magnetic field. The governing equation describing the superparamagnetic nanorod rotation in the Newtonian fluids is given by [264-267]:

$$\dot{\varphi} = \omega_c \sin 2\varphi \tag{6.1}$$

where the characteristic frequency ω_c is a constant associated with the nanorod properties and rheological behavior of the solution, given by [266, 267]:

$$\omega_c = \frac{[3\ln(l/d) - A]d^2}{2\eta\mu_0 l^2} \cdot \frac{\chi^2}{2+\chi} B^2 \tag{6.2}$$

where d and l are respectively the diameter and length of the nanorod, η the solution viscosity, χ the susceptibility of the nanorod, μ_0 the vacuum permeability, B the magnetic field and $A \approx 2.4$ [266, 267]. Introduce the distribution function $F(\varphi, t)$, whose definition is given as: $dN(\varphi, t) = N_0 F(\varphi, t) d\varphi$. Where N_0 is the total number of rods. The evolution of distribution function satisfies the conservation of total number of nanorods [87, 160, 161]:

$$N_0 \frac{\partial F}{\partial t} + \frac{\partial}{\partial \varphi} \cdot \left(N_0 F \cdot \frac{d\varphi}{dt} \right) = 0 \tag{6.3}$$

The governing equation for the distribution function is then obtained [268, 269]:

$$\frac{\partial F(\varphi,t)}{\partial t} - \frac{\partial}{\partial \varphi}[F(\varphi, t)\omega_c \sin 2\varphi] = 0 \tag{6.4}$$

The above equation can be solved using the method of characteristics [270]. The following solution is obtained:

$$F(\varphi, t) = \frac{1}{2\pi} \cdot \frac{2C}{(C^2-1)\cos 2\varphi + (C^2+1)} \tag{6.5}$$

where $C(\mathrm{t}) = \exp(-2\omega_c t)$. The solution is verified through integration of $F(\varphi, t)$ from 0 to 2π which yields 1. It's convenient to use probability function $P(\varphi, t)$ to find the nanorods positioned within a narrow angle $[\varphi - \Delta\varphi, \varphi + \Delta\varphi]$:

$$P(\varphi, \Delta\varphi, t) = \int_{\varphi-\Delta\varphi}^{\varphi+\Delta\varphi} F(\varphi', t) \cdot d\varphi' = \frac{1}{2\pi} \arctan\left[\frac{\tan\varphi'}{C(t)}\right] |_{\varphi-\Delta\varphi}^{\varphi+\Delta\varphi} \quad (6.6)$$

The initial random orientation corresponds to $P(\varphi, 0) = \Delta\varphi/2\,\pi$ and as time goes to infinity $P(0, \Delta\varphi, \infty) = 1$ (meaning that all rods can be aligned).

6.3.2 Orientation of superparamagnetic nanorods in solidifying films

We show one example of the distribution function of nanorods in solidifying films, whose rheological equation of state is time-dependent. The time-dependent viscosity of many drying systems is described by the following equation [271]:

$$\eta(t) = \eta_0 \exp(t/\tau_0) \quad (6.7)$$

where η_0 is the initial viscosity, τ_0 the characteristic time of polymerization. Introducing $U = U_0 \cdot \exp\left(\frac{t}{\tau_0}\right)$, Eq. (6.1) is rewritten into:

$$\frac{d\varphi}{dU} = -\frac{\sin 2\varphi}{U^2} \quad (6.8)$$

where $U_0 = \frac{\mu_0 \eta_0 l^2}{d^2} \cdot \frac{2+\chi}{\chi^2} \cdot \frac{1}{\tau_0 B^2 [3\ln(l/d) - A]} = \frac{\tau_\eta}{\tau_0}$. τ_η is the characteristic time needed for a nanorod to find its equilibrium configuration in a liquid with constant viscosity η_0. In our experiment, τ_η was adjusted by altering the magnetic field strength.

Integration of Eq. (6.8) yields:

$$\tan\varphi = \tan\varphi_0 \cdot \exp\left(\frac{1}{U} - \frac{1}{U_0}\right) \quad (6.9)$$

As $U \to \infty$, $\tan\varphi = \tan\varphi_0 \cdot \exp\left(-\frac{1}{U_0}\right) = \tan\varphi_0 \cdot \exp\left(-\frac{\tau_0}{\tau_\eta}\right)$, illustrates the effect of different time scales. When $\tau_0 \gg \tau_\eta$, the nanorod will align to the direction of the applied magnetic field, and when $\tau_0 \ll \tau_\eta$, the nanorod stays 'frozen'. As for

ferromagnetic nanorods, the dimensionless equation for the rotation of single nanorod is slightly different, which is given by [87]:

$$\frac{d\varphi\prime}{dU} = -\frac{\sin\varphi\prime}{U^2} \tag{6.10}$$

And the solution to φ' for a ferromagnetic nanorod is given by [87]:

$$\tan\frac{\varphi\prime}{2} = \tan\frac{\varphi\prime_0}{2} \cdot \exp\left(\frac{1}{U} - \frac{1}{U_0}\right) \tag{6.11}$$

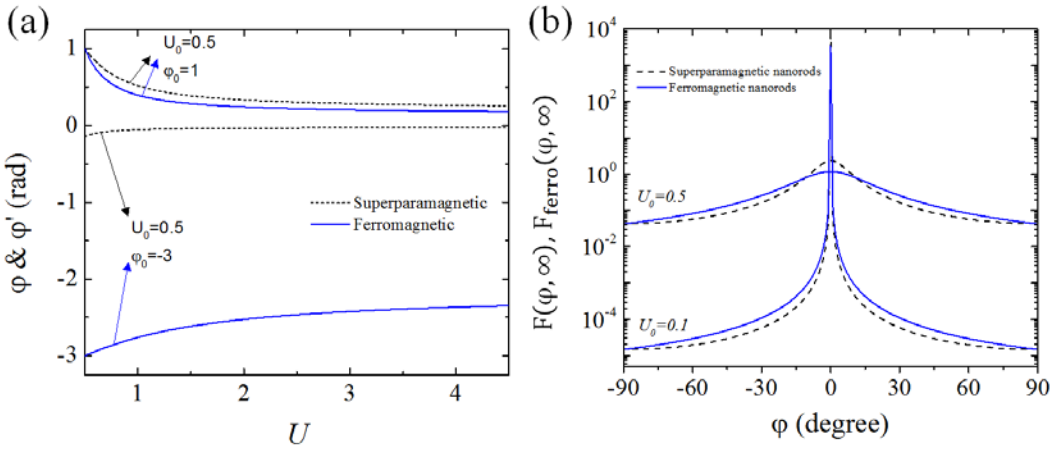

Figure 6.4 Plot of (a) different dynamic regimes of nanorods rotation and (b) distribution functions $F(\varphi, \infty)$ for ferromagnetic and superparamagnetic nanorods for different parameters U_0. Initial values for φ_0 and U_0 are given.

Figure 6.4(a) shows the comparison between Eq. (6.9) and Eq. (6.11) with different initial values of φ_0 and U_0. When φ_0 is less than $\pi/2$, the ferromagnetic nanorod orients more readily with the progression of U than the superparamagnetic nanorod with the same given values of U_0. However, when φ_0 is between $\pi/2$ and π, the opposite scenario was observed. This is due to a smaller periodicity in the superparamagnetic solution (π) as compared to the ferromagnetic solution (2π). That is, the superparamagnetic rod rotates toward $\varphi = \pi$ instead of $\varphi = 0$ with an initial orientation between $\pi/2$ and π. As for the

ferromagnetic nanorod, it always rotates toward $\varphi = 0$, the direction of the applied magnetic field.

The corresponding distribution function F for superparamagnetic nanorods can be solved using the same method from Eq. (6.4) [87]:

$$F(\varphi, t) = \frac{1}{2\pi} \cdot \frac{2C'}{\left(C'^2 - 1\right)\cos 2\varphi + \left(C'^2 + 1\right)} \tag{6.12}$$

where $C'(\mathrm{t}) = \exp\left[-\frac{1}{U_0}\left(1 - \exp\left(-\frac{t}{\tau_0}\right)\right)\right]$. When $t \to \infty$, the distribution function for a solidified film is given as:

$$F(\varphi, \infty) = \frac{1}{2\pi} \cdot \frac{1}{\cosh(1/U_0) - \sinh(1/U_0)\cos 2\varphi} \tag{6.13}$$

The corresponding probability function is given as:

$$P(\varphi, \Delta\varphi, \infty) = \int_{\varphi-\Delta\varphi}^{\varphi+\Delta\varphi} F(\varphi', t) \cdot d\varphi' = \frac{1}{2\pi} \arctan\left[\tan\varphi' \cdot \exp\left(\frac{1}{U_0}\right)\right] \Big|_{\varphi-\Delta\varphi}^{\varphi+\Delta\varphi} \tag{6.14}$$

The probability function at $t \to \infty$ is affected by U_0, which is determined by the property of the nanorods, the characteristic time of drying and the strength of the magnetic field. The set of equations (6.7-6.9, 6.12-6.14) is an example of the nanorods alignment in a solidifying film. For the films with different kinetics of viscosity evolution, the corresponding solution in Eq. (6.8) changes and one can obtain different expressions for U_0.

The equilibrium distribution function $F_{ferro}(\varphi, \infty)$ for ferromagnetic nanorods is given by [87]:

$$F_{ferro}(\varphi, \infty) = \frac{1}{2\pi} \cdot \frac{1}{\cosh(1/U_0) - \sinh(1/U_0)\cos\varphi} \tag{6.15}$$

Here U_0 is also defined as $\frac{\tau_\eta}{\tau_0}$. The characteristic time τ_η has a slightly different dependence on the magnetic properties of the nanorods and rheological properties of the liquid. The corresponding probability function for ferromagnetic nanorods is given by [87]:

$$P_{ferro}(\varphi, \Delta\varphi, \infty) = \frac{1}{\pi}\arctan\left[\tan\frac{\varphi'}{2}\cdot\exp\left(\frac{1}{U_0}\right)\right]\Big|_{\varphi-\Delta\varphi}^{\varphi+\Delta\varphi} \tag{6.16}$$

Figure 6.4(b) shows the plots of the distribution function $F(\varphi, \infty)$ and $F_{ferro}(\varphi, \infty)$ with different values of U_0. Function $F(\varphi, \infty)$ (Eq. (6.13)) has a periodicity of π. The orientations of nanorods with $\varphi = \pi$ and $\varphi = 0$ are essentially identical. Therefore due to its symmetry at $\varphi = 0$, function $F(\varphi, \infty)$ is doubled when comparing with $F_{ferro}(\varphi, \infty)$. Comparing to that of the ferromagnetic nanorods, the distribution function of superparamagnetic nanorods has a narrower profile and slightly greater peak value ($F_{ferro}(0, \infty)$ and $F(0, \infty)$), which indicates more nanorods can be captured by the field. The peak value of the function decreases as U_0 increases. When U_0 goes to infinity, the peak values of both functions asymptotically reach $1/2\pi$.

6.3.3 Aligned SiC-Fe_3O_4 short fibers

In the above theory, nanorods were assumed to remain isolated with no physical interactions between the nanorods. This requires that the nanorods are well-separated in the drying solution. In our experiment, the smallest average distance between inclusions, 41±20μm, is 4 times larger than the average length of the particulates, making the particulate to particulate interactions an unlikely source for disorientation. During solidification of the liquid films, the SiC-Fe_3O_4 nanorods were rotated into the direction of

the field creating orientation. Figure 6.5 shows the orientational distribution of the SiC-Fe_3O_4 nanorods after the polymer removal. With a magnetic field strength of 216 Gauss, the composite with initially 0.16%vol of SiC-Fe_3O_4 nanorods has higher orientation with 77% of material oriented within 10° of the direction of the field. The composite with 0.58%vol of SiC-Fe_3O_4 nanorods had 67% of the material oriented within 10° of the direction of the field. The orientation was less significant as a weaker magnetic field (37 Gauss) was applied. Less than 40% of nanorods oriented within 10° of the direction of the field for both concentrations. When the magnetic field is 6 Gauss, the orientation of the nanorods was almost random. Overall, the nanorods assembly obtained from initially lower volume fraction in polymer solution demonstrates a slightly better alignment. Eq. (6.14) was used to fit the experimental data with adjustable parameter: $\exp\left(-\frac{1}{U_0}\right)$. The results are shown in figure 6.5. A smaller value of $\exp\left(-\frac{1}{U_0}\right)$ was found for samples obtained at larger magnetic field. This is in good agreement with the theory according to the definition: $U_0 = \frac{\mu_0 \eta_0 l^2}{d^2} \cdot \frac{2+\chi}{\chi^2} \cdot \frac{1}{\tau_0 B^2 [3\ln(l/d) - A]}$ – as B increases, $\exp\left(-\frac{1}{U_0}\right)$ decreases.

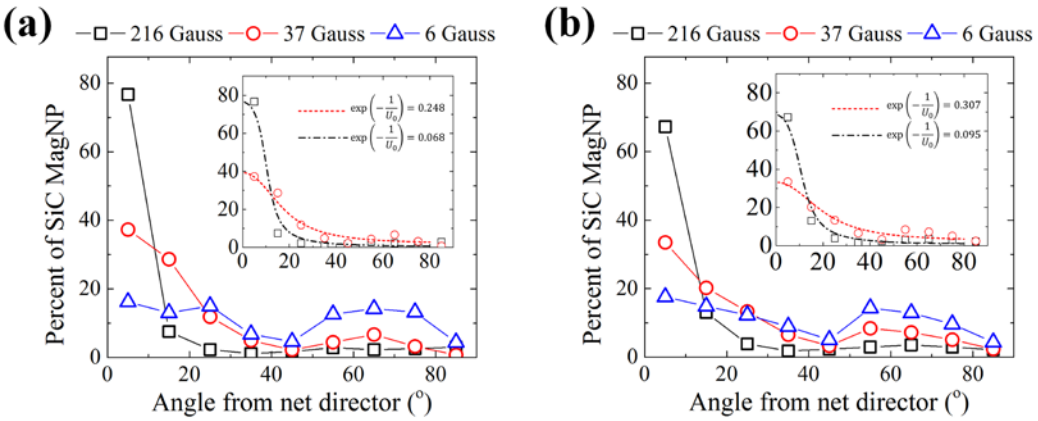

Figure 6.5. The distribution of orientation of SiC-Fe_3O_4 rods after PEO removal. (a) low concentration and (b) high concentration. The internal frames show the curve fitting according to Eq. (6.12)

The SiC-Fe_3O_4 nanorods remained separated during polymer removal, ceramic gel film deposition and gel to ceramic film conversion. Figure 6.6 shows the orientational distribution of nanorods during each of those steps. Overall, the most significant alignment was in the initial polymer films. The changes in the percentage (ΔP) of nanorods within each 10° segment with respect to the initial distribution in polymer films are shown in figure 6.6 (c-d). For the majority of nanorods, ΔP is less than 5%. This deviation initially appeared after the polymer removal, which is possibly due to the settlement of nanorods during the polymer decomposition. A slow heating process to remove the polymer is desired to better retain the orientation. The orientation remains almost still after the gel film deposition and gel to ceramic conversion, which indicates less motion of the nanorods after they were sintered to the substrate. In principle, orientational differences between those processing stages are quite small.

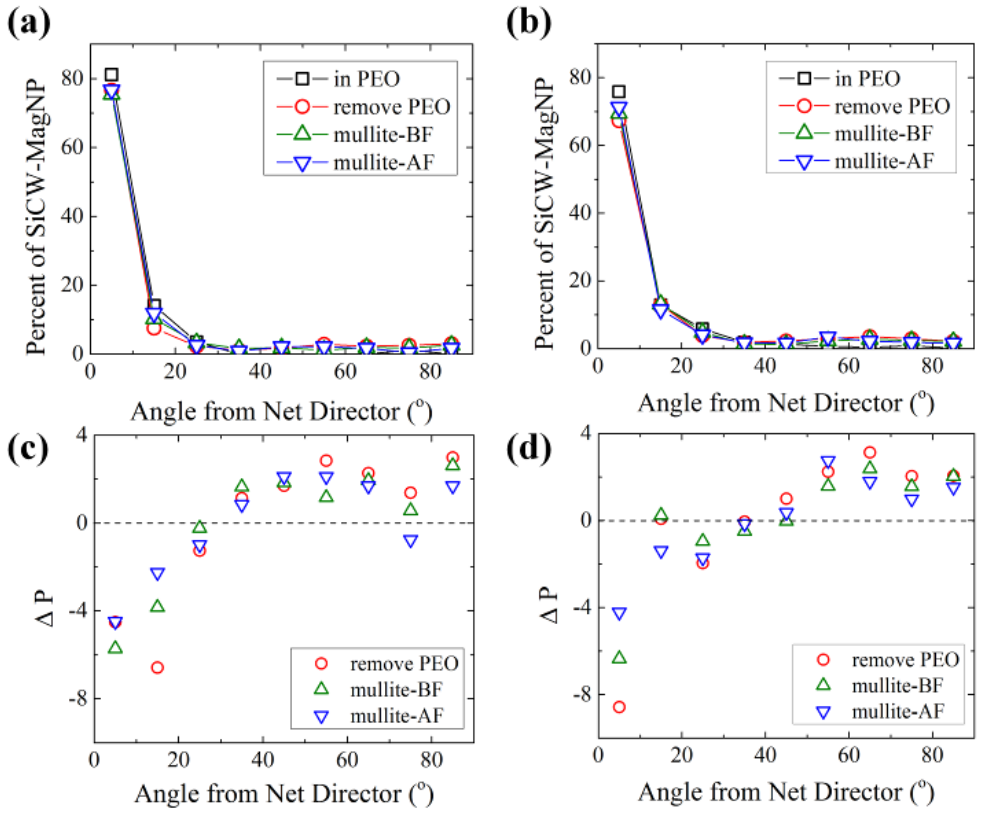

Figure 6.6. The orientational distribution of SiC-Fe_3O_4 nanorods of (a) low and (b) high concentration. (c) (low concentration) and (d) (high concentration) show the change in probability of the nanorods with respect to the initial functions in PEO.

Figure 6.7 shows the SEM images of single-layered mullite film embedded with SiC-Fe_3O_4 nanorods. The embedded SiC-Fe_3O_4 nanorods were well-separated and aligned. No significant nanorods segregation was observed. Layer-by-layer (LBL) assembly method offers the opportunity to create 3D nanocomposites through repetition of the 2D assembly [272, 273]. Controlling nanorods orientation within each layer is of particular interests for many applications. For example, an orthotropic lattice structure is often desired for effective mechanical reinforcement in all directions [67]. Figure 6.8 (a) shows the SEM image of a 2-layer mullite-SiC-Fe_3O_4 film with orthotropic structure. Figure 6.8

(b) shows the corresponding orientational distribution. The orientation of the major populations of SiC-Fe_3O_4 nanorods within each layer is perpendicular to the other.

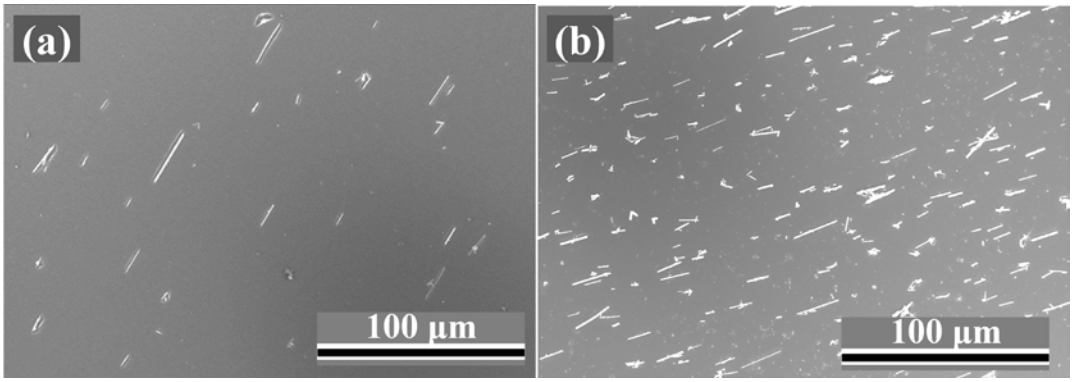

Figure 6.7. SEM images showing the top view of (a) low concentration and (b) high concentration.

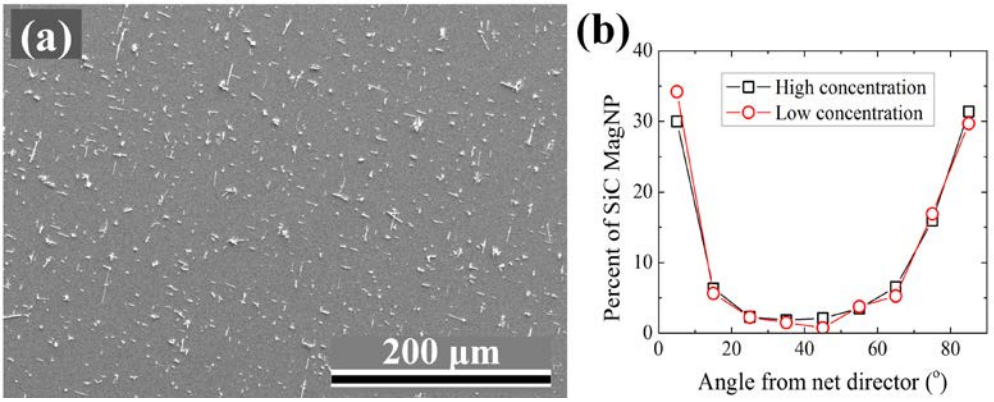

Figure 6.8. (a) SEM image showing the 2 layer mullite-SiC-Fe3O4 film with orthogonal nanorod orientations. (b) The orientational distribution of the 2-layer mullite-SiC-Fe3O4 thin film

Figure 6.9 shows the magnetization-field (*M-H*) plot of the free standing mullite-SiC-Fe_3O_4 membranes. It shows that the ceramic thin film composites are superparamagnetic. The magnetization of the material is normalized by the total mass of the composite. For

superparamagnetic materials, the magnetic moment m follows the Langevin dependence [274]:

$$m = m_0 \left[\coth(\kappa B) - \frac{1}{\kappa B}\right] \tag{6.15}$$

where B is the magnitude of the external magnetic field, $m_0 = N\mu$, and $\kappa = \mu/(k_B T)$, μ is the magnetic moment of a single magnetic domain, N the total number of domains in the composite, k_B is the Boltzmann constant and T is the absolute temperature. The magnetic Fe_3O_4 nanoparticles in the film composite contribute to this superparamagnetism. From the fitting, the composite membranes have saturation magnetization of around 0.41 Am^2/kg, which is about two to three orders of magnitude smaller than the typical values reported for superparamagnetic Fe_3O_4 nanoparticles [275-277]. The reveals that the concentration of magnetic materials within the free-standing membrane should be on the order of 0.1-1 wt.%. This concentration can be further controlled by altering the ratio between thicknesses of the polymer films and ceramic gel films. From the Langevin fitting, the magnetic moment of each domain is on the order of 4.7×10^{-20} Am^2.

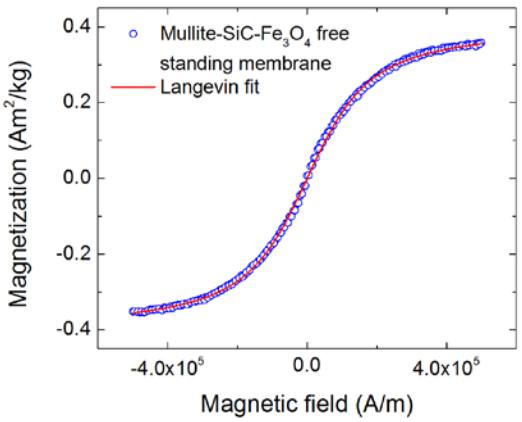

Figure 6.9. *M-H* curve of free-standing mullite-SiC-Fe_3O_4 membrane

6.3.2 Aligned mullite-nickel nanocomposite long fibers

Figure 6.10 shows the aligned fiber on the silicon substrate. Ni nanoparticles of size ~ 50 nm were observed on the surface of the individual fibers. The alignment was mainly contributed by to two factors. One is the mechanical stretching caused by the rotating collector. The second one is the opposite directions of electric field near the plates. When the jet hits one electrode, the tip of the jet are neutralized and the electric force pulls the rest of the jet towards another plate [113]. As a result, the charged fibers align perpendicular to the plates [113]. Integration of ceramic films with ordered ceramic fibers results in an organized 2D structure with fibers 'piping' underneath. Figure 6.11 (a-c) proves that the orientation of fibers (angles formed by the fibers) did not change significantly during the processing stages. Figure 6.11 (d) shows the AFM image of the thin film's surface with embedded nanofibers. The roughness of the ceramic film itself is very low comparing to the protrusions formed by the embedded fibers. The roughness of the composite film is therefore determined by the vertical height of the surface protrusions induced by the fibers.

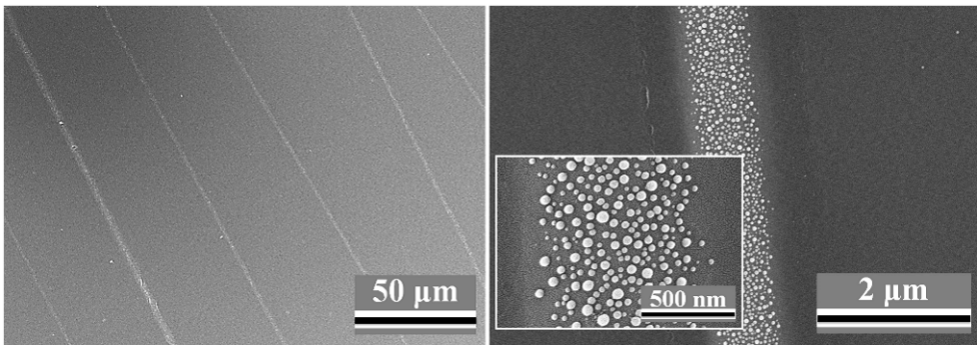

Figure 6.10. SEM images showing the microstructure of aligned fibers modified with magnetic nanoparticles.

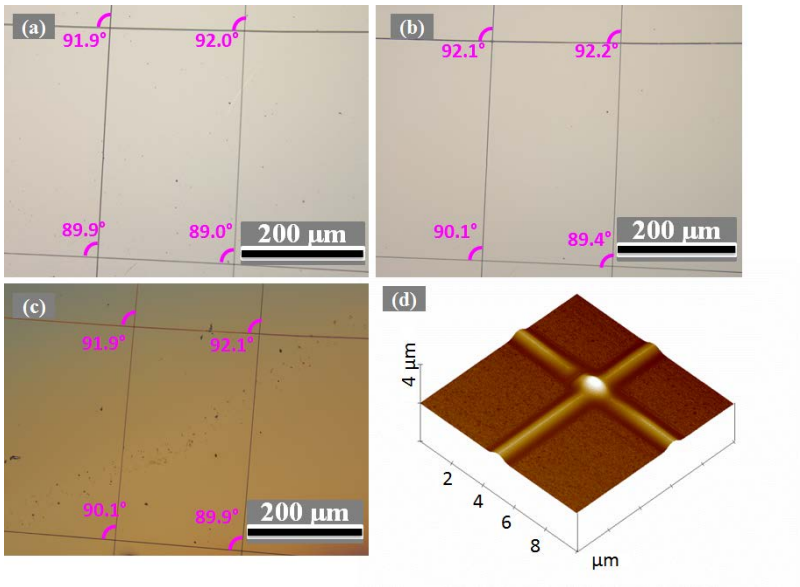

Figure 6.11. Optical micrographs showing the nanofiber fishnet structure obtained after (a) electrospinning (b) heat treatment and (c) integration of mullite film followed by heat treatment in Argon at 1000°C. (d) The topographic image of a cross knot measured by AFM.

6.4 Conclusion

In this chapter, we demonstrate two methods of processing ceramic thin films embedded with oriented fibers. In the first method, magnetic short fibers (SiC-Fe_3O_4 rods) were dispersed in a polymer solution to form a polymer thin film composite under applied magnetic field. The polymer was then removed by heat treatment. In the second method, pre-aligned magnetic long fibers (mullite-nickel) were obtained via electrospinning. Mullite thin films were integrated onto both fibers. The film integration process did not significantly alter the fiber structure and the orientations were retained in both methods. The magnetic measurement performed on mullite-SiC-Fe_3O_4 free standing composite membranes proves the magnetic functionality of the composite films. Based on our

observation, we conclude that both of these two approaches (electrospinning and magnetic assembly) can be for processing ceramic thin film with retained orientations of the embedded fibers. The thin film evolution with the presence of fibers will be investigated in detail in the next chapter.

CHAPTER VII

EFFECT OF NANOROD INCLUSION OF THE THIN FILM INTEGRITY DERIVED FROM THE SOL-GEL

7.1 Introduction

One of the greatest challenges of sol-gel thin films is the macroscopic cracking caused by the intrinsic stress, which has been described in chapter 5. Another challenge remains in the integrity of thin films deposited on substrates with fibers or rods. Presence of fibers affects the local equilibrium where the film conforms on the fiber inclusions, giving rise to many unique phenomena such as the topographic evolution and cracking of thin films. However, the driving mechanism to those phenomena was not clear. In this chapter, detailed investigations are given to fundamentally understand the topographic evolution of sol-gel composite thin film and the cracking problem with the nanofiber or nanorod inclusions.

In previous studies, the micrometer thick film formation on substrates with features in micrometer scale (e. g. holes, trenches or wedges) was governed by the Stokes flow of liquids and kinetics of planarization [52-58]. The capillary pressure, which is the driving force for the planarization process, is determined by the radii of curvature of the meniscus [52-58]. In the case of nanometer and submicrometer fibers coated with thin films of similar scale, the radii of curvature is much smaller compared with the micrometer sized features [52-58], and the body forces exerted by viscous drag did not contribute. Our experimental results indicate that for thin films, the degree of leveling (or planarization) is typically very small. For the film with thickness in nanoscale, the contribution of disjoining

pressure becomes significant and shall be considered in our model [278-280]. The driving force for planarization is balanced by the disjoining pressure, which is the repulsive interactions between the solid-liquid and liquid-vapor interfaces determined by the layer thickness. In this case, it is possible to generate the equilibrium thickness profile with these two governing mechanisms. Equilibrium shape of the liquid layer on the nanorods or nanofibers is determined by the Derjaguin equation [279, 281, 282]:

$$P_{cap} = \sigma^v \kappa - \Pi(h), \quad \sigma^v > 0 \tag{7.1}$$

where P_{cap} is the pressure difference in the liquid and gas, $P_{cap} = P_{liquid} - P_{gas}$, σ^v the liquid-vapor surface tension, κ the curvature and $\Pi(h)$ the disjoining pressure, a function of layer thickness *h*. It is assumed that the disjoining pressure is dominated by the Lifshitz-van der Waals forces [279, 283]. The disjoining pressure has the following form: $\Pi(h) = A/h^3$, where *A* is the Hamaker-Lifshitz constant, which is typically on the order of 10^{-21}-10^{-19} J [278].

Figure 7.1 schematically shows the configuration of liquid film on substrate with a cylinder-shape inclusion. The systems of coordinate are also shown in the figure. Since the aspect ratio of the cylinder-shape inclusion (fiber) is typically much greater than 10, the problem is simplified as a 2D configuration with *Polar* coordinate whose origin is concentric with the cross-section of the cylinder. And *Cartesian* coordinates are used in the cross-section plane far away from the fiber. Under stationary state, the pressure difference P_{cap} is assumed constant everywhere within the film. The curvatures are known as:

$$\kappa_c = \frac{(R+H_c)^2+2H_c'^2-H_c''(R+H_c)}{\left[H_c'^2+(R+H_c)^2\right]^{3/2}} \tag{7.2}$$

and,

$$\kappa_p = -\frac{H_p''}{\left(1+H_p'^2\right)^{3/2}} \tag{7.3}$$

H_c, H_p and R are respectively the film thicknesses (of center and plane solutions) and radius of the cylinder, which are defined in Figure 7.1. $H_c(\theta)$ is a function of angle θ in the *Polar* coordinate, and $H_p(x)$ is a function of *x*. In our particular system, a thin layer of liquid film of tens of nanometers formed on top of the nanorod/nanofiber. The local curvature is assumed to be governed by the curvature of the nanorod ($\kappa_{c0} \approx \frac{1}{R}$). The following equation was used to approximate the relation between thickness on top of the rod (H_{c0}) and far away from the rod ($H_{p\infty}$):

$$\frac{\sigma_v}{R} - \frac{A}{H_{c0}^3} = -\frac{A}{H_{p\infty}^3} \tag{7.4}$$

Introducing dimensionless parameter $X = \frac{x}{R}$, $h_c(X) = \frac{H_c}{R}$, $h_p(\theta) = \frac{H_p}{R}$ and $\bar{A} = \frac{A}{R^2\sigma^v}$, Eq. (7.1) was transformed into the dimensionless form:

$$\begin{cases} -\frac{\bar{A}}{h_{p,\infty}^3} = \frac{2h'^2_c - h''_c(1+h_c)+(1+h_c)^2}{\left(h'^2_c+(1+h_c)^2\right)^{3/2}} - \frac{\bar{A}}{h_c^3}, \\ -\frac{\bar{A}}{h_{p,\infty}^3} = -\frac{h''_p}{\left(1+h'^2_p\right)^{3/2}} - \frac{\bar{A}}{h_p^3} \end{cases} \tag{7.5}$$

Eq. (7.4) can be transformed to the following form:

$$h_{c0} = h_{p\infty} \cdot \left(1 + \frac{h_{p\infty}^3}{\bar{A}}\right)^{-1/3} \tag{7.6}$$

7.2 Experimental procedure

7.2.1 Materials preparation

The SiC whiskers with round cross-sections were used as the cylindrical film inclusion. Films with different thicknesses were processed according to the procedure described in chapter 5. The microstructure of the film was examined using atomic force microscopy (AFM, Dimension 3100 AFM, Veeco Inc, Plainview, NY, USA) and scanning electron microscope (SEM, Hitachi S4800**,** Hitachi, Ltd., Tokyo, Japan). Before the heat-treatment, a scratch through the film was applied to the film using a sharp blade. The thickness was determined by scanning the profile across the scratch and measuring the depth of the scratch. The surface profile of the composite films was generated from the AFM measurement. The diameters of the fibers were measured from the SEM micrographs. Samples were marked as cracked or crack-free with the observation under the SEM.

7.2.2 Numerical method

The solutions to h_p and $h_c$were solved numerically. For the plane solution (h_p), a trivial solution, h_p=*const* is found. It also has another solution of which asymptotic expansion could be obtained as follows. Introduce the $\delta u << h_{p,\infty}$ at infinity,

$$h_p = h_{p,\infty} + \delta u \tag{7.7}$$

With the given boundary condition: $h_p'(X \to \infty) = 0$, substitute Eq. (7.7) into Eq. (7.5) and we obtain:

$$h_p(X \to +\infty) = h_{p,\infty} + C\exp(-\lambda X), \quad \lambda^2 = \frac{3\bar{A}_p}{h_{p,\infty}^4} \tag{7.8}$$

where C is an unknown integration constant. For the coordinate system set up in our problem, the sign of C should be positive. Eq. (7.8) specifies the initial values for $h_{p,\infty}$ and

$h'_{p,\infty}$ for the numerical calculations. The initial point (X_0) to start the integration is defined as $X_0 = '\infty'$. In other words, solution to h_p with given initial values can shift along the x-axis. Due to the symmetric condition at the center ($\theta = 0$), initial value for $h'_c(\theta = 0)$ is given by $h'_c(\theta) = 0$. The initial value for $h_c(\theta = 0)$ is given by h_{c0} in Eq. (7.6). The non-linear second-order differential equation is solved by using '*ode23*' function in *Matlab*. Solution for $h_c(\theta)$ is then transferred into the Cartesian coordinate ($h_c^{new}(X)$, corresponding to the height of the film surface) according to the geometric relations.

To find the solution to Eq. (7.5), we apply the following condition at the interface. The obtained solutions to $h_c^{new}(X)$ and $h_p(X)$ must match with the same coordinate and slope. Therefore the following conditions must be satisfied at the interface.

$$\begin{cases} h_c^{new}(X_1) = h_p(X_1) \\ h_c^{new\prime}(X_1) = h_p{}'(X_1) \end{cases} \tag{A2.5}$$

where X_1 corresponds to the point where these two solution matches. The matching condition is determined by the least square method with two adjustable parameters X_0 (definition of 'infinity') and X_1.

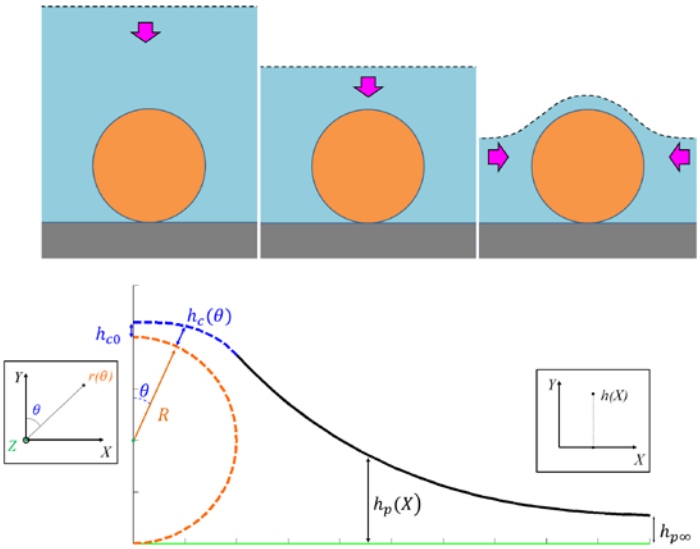

Figure 7.1. Top: schematically showing the drying process of liquid film and formation of meniscus on top of the nanorod. Bottom: definition of the variables in the thin film leveling model

7.3 Results and discussion

7.3.1 Microstructure of the film with nanofibers and nanorods

The high resolution SEM images of the crack-free composite films are shown in Figure 7.2. By varying the film thickness (*t*) with the similar fiber diameter (*D*), different microstructures were observed. When the applied film is very thin (Figure 7.2 (a & d), with film thickness ~ 50 nm), the surface shows the trace of the embedded Ni nanoparticles. This is due to that the thin film is conformal to the surface of the fiber with nanoparticles. When the film thickness increases, the surface projections of the nanoparticles become vague (Figure 7.2 (b & e), with film thickness ~ 100nm), and eventually disappear (Figure 7.2 (c & f), with film thickness ~ 200nm).

Similar microstructure was observed in mullite-SiC-Fe3O4 composite thin films. The magnified SEM images of the films with embedded nanorod are shown in figure 7.3. The

SiC-Fe_3O_4 nanorod was distinguished from the thin film matrix when the film thickness (60 nm) is small compared to the dimension of the rod, as shown in figure 7.3 (a). The grainy feature on the rod's surface corresponds to the presence of Fe_3O_4 NPs. With a slightly thicker ceramic film (140 nm), the contour of the nanorod becomes less distinct from the film matrix, which is shown in Figure 7.3 (b). The grainy feature on the rod was masked by the ceramic film on the top. The result indicates that nanorods could be embedded completely, with the application of thicker films. The microstructure of such thick films (~500 nm) with embedded nanorods is shown in figure 7.3 (c-d). An interesting feature of such thin film composites is the surface protrusion observed due to the presence of the nanorod. It was observed that surface protrusions can be gradually eliminated with the deposition of mullite films of greater thickness. The detailed mechanisms will be discussed in the next section. Figure 7.3 (d) shows the cross-section view of an embedded SiC-Fe3O4 nanorod in the mullite film. The thickness evolution of the film close to the nanorod position was evidenced.

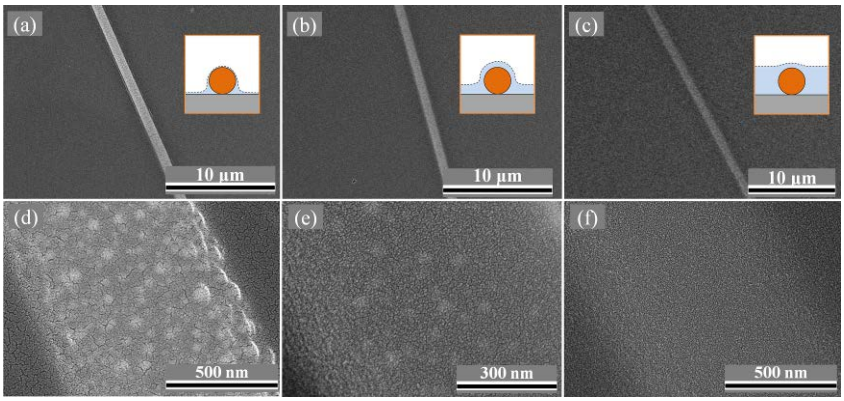

Figure 7.2. SEM image showing the thin films on mullite fibers embedded with Ni nanoparticles

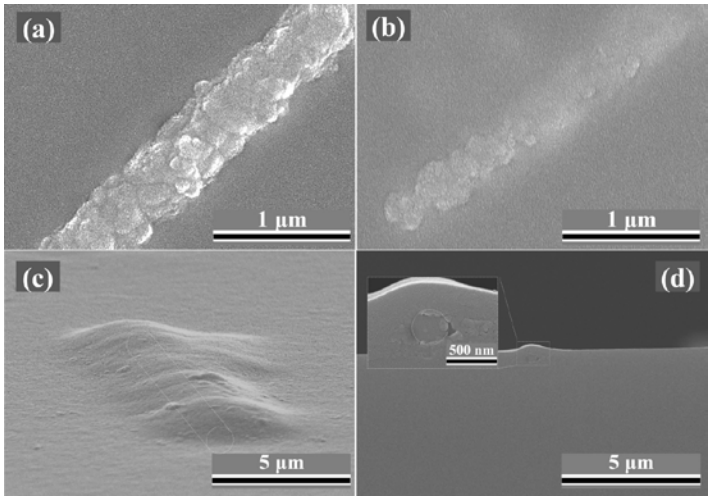

Figure 7.3. SEM images showing the coatings on SiC-Fe3O4 nanorods. Film thickness (a) 60nm, (b) 140 nm, (c) & (d) 500nm

7.3.2 Thickness evolution and crack formation

The final film thickness (t) without any inclusion, fiber diameter (D) and τ_c are important as it determines whether microscopic cracking occurs around the embedded fibers. First of all, the film thickness must be smaller than the critical thickness, otherwise cracking occurred no matter whether there were cylindrical inclusions. If $t < \tau_c$, then there were two scenarios of interests: thin film with large rods (type 1, $D > t$) and with small rods (type 2, $t > D$). Figure 7.4 shows the surface profile of the thin film with fibers for both cases. The gel films remained crack-free before heat treatment.

When $t > D$, no cracking was observed after heat treatment. The film is relatively flat with small protrusion caused by the nano-inclusion. The presence of the small protrusions can be explained by the following scenario. For the liquid film, the surface remains flat at early stages upon drying. The surface of the film gradually falls down during solvent evaporation (as shown in Figure 7.1). Meanwhile, the concentration of solute and

solution viscosity increases exponentially with time [242]. Large viscosity arises from drying which restrains the lateral flow. Upon further solvent evaporation, the film shrinks by the same volume fraction of residual solvent on top of and aside from the nanorod. One would expect different absolute shrinkage in height at the different locations. This creates the non-stationary film profile with a small meniscus formed on the surface. The final profile should be the intermediate condition between the stationary (flat surface) and the case with completely no lateral flow (shown in Figure 7.4 (a), calculated by assuming a constant ratio of film shrinkage (90%) estimated from the beginning solution).

If $D > t$, the cracking phenomenon was complicated. Cracking was observed in certain samples after heat treatment, but not in others. If cracking was observed, the cracks were always at the edge of the inclusion where the thin film surface started to bend up towards the top of the inclusion (Figure 7.4 (b), the red curve). No cracking was observed when the film was sufficiently thin (Figure 7.4 (b), the blue curve). Cracking can also be prevented with enhanced critical thickness τ_c. As shown in figure 7.4 (c) (blue curve), the film remains crack-free even with a slightly greater thickness comparing to the one in 7.4 (b) (red curve). Figure 7.5 shows microstructure of the cracked film with the fiber. The microscopic cracking was typically observed at the edge, along the longitudinal direction of the fiber/rod.

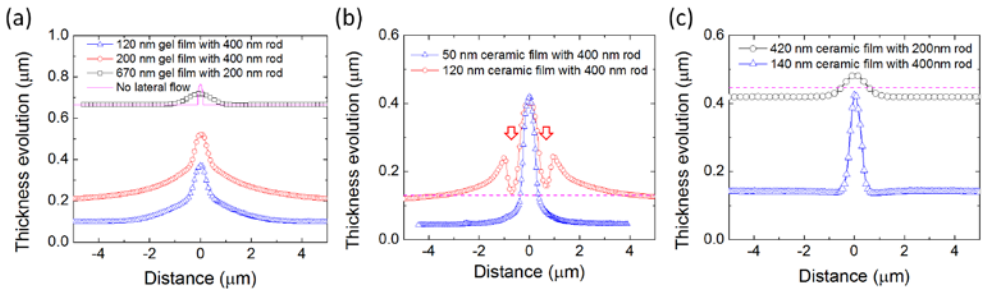

Figure 7.4. Surface profile of (a) as-deposited gel film and (b & c) the ceramic film after calcination. (b) and (c) are with different critical thickness, shown by the dashed line. The cracks were marked by the arrows.

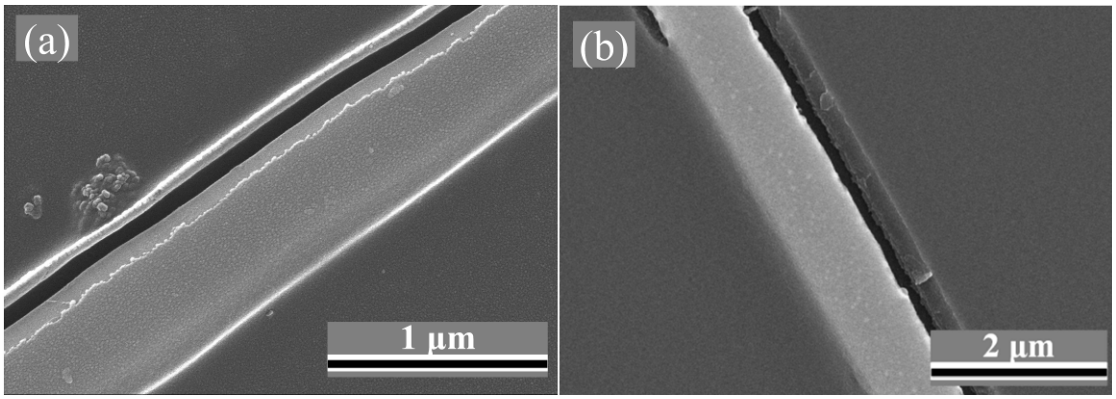

Figure 7.5. Cracking of thin film in the vicinity of the (a) SiC and (b) mullite-nickel fiber.

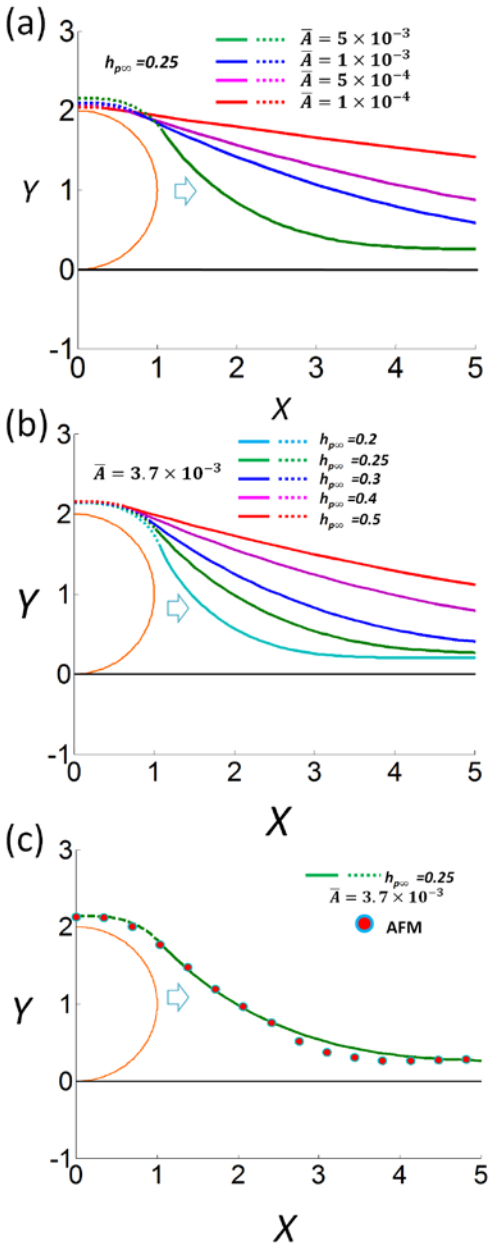

Figure 7.6. Profile generated comparing to conformal films, the coordinates are normalized by the fiber radius *R*. (a): Solutions for the same $h_{p\infty}$=0.25 and different values of $\bar{A}$. (b): Solutions for the same $\bar{A} = 0.0037$ with different values of $h_{p\infty}$. (c): The generated curve matches the experiment for small $h_{p\infty}$. The arrows sketch the position of the necking area.

Figure 7.6 shows the profile of the films predicted using Eq. (7.5) using the boundary conditions described above. With the same normalized film thickness $h_{p\infty}$ = 0.25,

the stationary profile became more flattered as $\bar{A}$ decreases (Figure 7.6(a)), where $\bar{A}$ is proportional to the strength of the interaction between the two surfaces of a thin film and consequent disjoining pressure. The disjoining pressure term is balanced by capillary pressure caused by the surface tension, otherwise the solution will continue to flow until the pressure is equilibrated throughout the film. A strong disjoining pressure must cause a large curvature at the necking area (Figure 7.6), and ***vice versa***. With the same input of $\bar{A}$, the film also flattened as the film thickness increases (Figure 7.6 (b)). This is in good agreement with our experimental observation that the films tend to be flat with greater thickness. This phenomenon is caused by the thick film and consequent small disjoining pressure, and small balancing curvature. With the estimated values of $\bar{A}$, we generate numerical solutions and compare to the experimental results. Figure 7.6 (c) shows the generated profile matches well with the type 1 film with $h_{p\infty}$ = 0.25 and $\bar{A} = 0.0037$. The cylindrical inclusion radius is on the order of 10^{-7} m, surface tension of liquid is on the order of 10^{-2} N/m. The estimated value of A is on the order of 10^{-19} to 10^{-18} J, which is realistic and reasonable. The solution for thick films (e. g. $h_{p\infty} > 0.5$) does not match well with the experimental film profile on the top of the fiber. However the simulated profile matches well at the necking area and far away from the rod.

The numerical results match well with the thin film of ~60 nm thick. This modeling has certain limitations in predicting the surface profile of thick films with thickness above 100 nm. Specifically, the calculated surface profile does not match experimental result on the top of the inclusion. This mismatch is caused by the large film thickness. The disjoining pressure decreases dramatically with increasing film thickness. When the disjoining

pressure was sufficiently small, the lateral flux driven under the disjoining pressure and the balancing capillary pressure was too small and not able to equilibrate the pressure throughout the film during drying. The assumption of the modeling is no longer valid. This scenario is similar to the condition in type 2 film. Upon drying, meniscus forms and stationary profile cannot be established by lateral flux due to the high viscosity at this stage.

Crack develops in material possibly due to a stress concentration. For the reason that the films are thin and the surface steepness is typically small, we use the thin film approximation that only considers the effect of the in-plane stress. The non-uniform capillary pressure is distributed and balanced by the in-plane tensile stress:

$$\nabla_x \sigma_\tau = -\nabla_x P_c \tag{7.7}$$

The term σ_τ describes the stress contributed by the non-uniformity of the capillary pressure. For thin films that are conformal, the stationary state established in figure 7.6 indicates that P_c is uniform and $\nabla_x \sigma_\tau$ equals zero. The film is therefore subjected to a uniform stress which is defined by $\sigma_\tau(x \to \infty)$, the intrinsic stress within the planar films without fibers. The non-static profiles of the thick films lead to a gradient of stress, which leads to the concentration of stress near the fiber. However, the magnitude of this stress concentration is small. For example, the curvature observed in the experiment was on the order of ~ 10^6 m^{-1} (as shown in figure 7.4), the estimated capillary pressure contributed by curvature will be on the order of 0.1 MPa, which is significantly less than the elastic properties of the gel matrix [70]. The disjoining pressure should not be a dominating factor as well, because cracking is typically observed in thick films (as shown in figure 7.4) where disjoining pressure term is small. And cracking occurs more easily in thicker films, which

cannot be explained by disjoining pressure as it is more dominant in thin films. Therefore this stress concentration should not be the dominating mechanism.

In chapter 5, it has been shown that macroscopic cracking occurs as the film thickness is greater than the critical thickness [148, 149, 152]. When an inclusion is embedded within a film, it seems like the dominating effect should be the film thickness vs. critical thickness in the vicinity of the fiber. The mechanism is schematically shown in figure 7.7. In both modeling and experiment we showed the existence of a fiber caused the leveling of the film around it. This planarization effect is dominant in relatively thicker films (among the type 1 films). The film near the fiber has a thickness greater than the critical value. In our study, cracking was only observed when rod's diameter is greater than the critical thickness of the film. Qualitatively, the cracks were observed at the greatest evolved film thickness caused by leveling, whose values were above the critical thickness. The microscopic cracking can be prohibited by improving the critical thickness of the film, or reducing the rod diameter to film thickness.

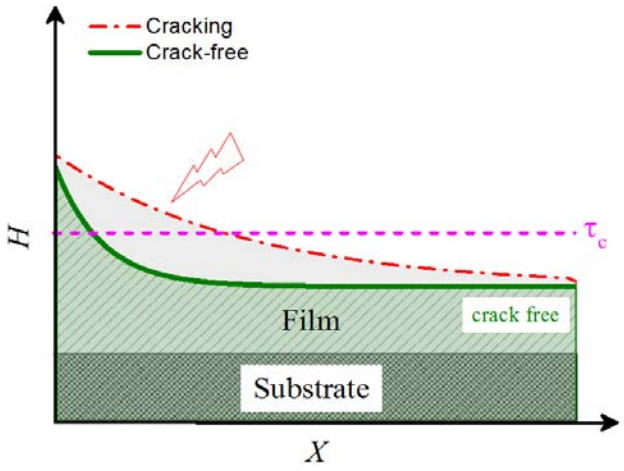

Figure 7.7 Schematically showing the occurrence of cracking determined by the film thickness evolution near the fiber.

7.4 Conclusion

To summarize, the conditions for the initiation of microscopic cracking were illustrated. No cracking was observed in films with small fiber diameters ($\tau_c > t > D$). Microscopic cracking was observed in films with intermediate thickness and large fiber diameter ($D > \tau_c > t$) and especially in non-conformal films. Thickness profile of the conformal films satisfies the stationary equation for capillary pressure distributions governed by curvature and disjoining pressure. The profile of non-conformal films deviates from the stationary curves. However, the stress contributed by non-uniform capillary pressure is small. Microscopic cracking is governed by the thickness evolution near the nanorod and the critical thickness. Microscopic cracking can be reduced and eventually eliminated by reducing the film thickness or improve the critical thickness of the film.

APPENDICES

Supportive experimental results

The SEM micrographs of fiber composites before and after chemical etching process are shown in figure A1. Before etching, the number density of nanoparticles appeared on the surface of the fiber is on the order of 10 per unit fiber length (micrometer). After etching, no particles were observed on the surface of the fiber. The surface of the etched fibers appears to be smooth, indicating the complete removal of surface particles.

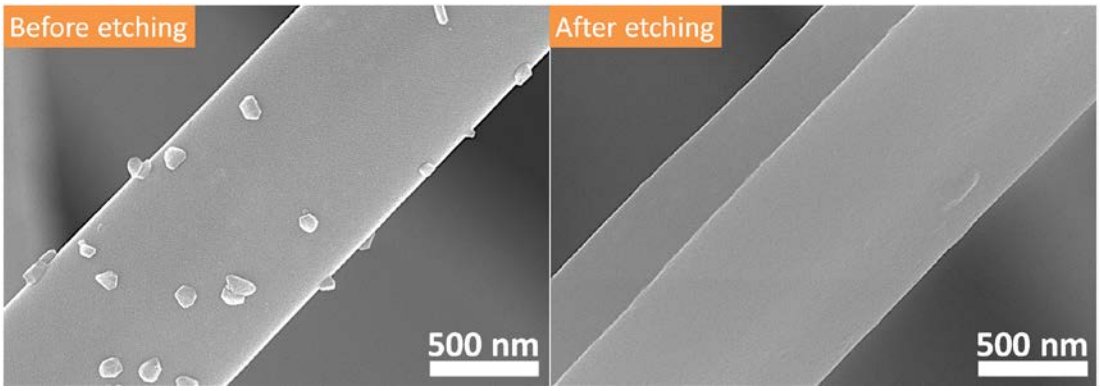

Figure A1: SEM micrographs showing the removal of surface nanoparticles after the etching process

References

[1] Öchsner, A., da Silva, L. F., & Altenbach, H. (2012). Advanced Structured Materials. Springer press.

[2] Gu, Z., Yang, Y., Li, K., Tao, X., Eres, G., Howe, J. Y., ... & Pan, Z. (2011). Aligned carbon nanotube-reinforced silicon carbide composites produced by chemical vapor infiltration. *Carbon*, *49*(7), 2475-2482.

[3] Peigney, A. (2003). Composite materials: tougher ceramics with nanotubes.*Nature materials*, *2*(1), 15-16.

[4] Xia, Z., Riester, L., Curtin, W. A., Li, H., Sheldon, B. W., Liang, J., ... & Xu, J. M. (2004). Direct observation of toughening mechanisms in carbon nanotube ceramic matrix composites. *Acta Materialia*, *52*(4), 931-944.

[5] Wu, J. M., Zhang, T. W., Zeng, Y. W., Hayakawa, S., Tsuru, K., & Osaka, A. (2005). Large-scale preparation of ordered titania nanorods with enhanced photocatalytic activity. *Langmuir*, *21*(15), 6995-7002.

[6] Gao, P. X., Ding, Y., & Wang, Z. L. (2003). Crystallographic orientation-aligned ZnO nanorods grown by a tin catalyst. *Nano Letters*, *3*(9), 1315-1320.

[7] Lu, Q., Gao, F., Komarneni, S., & Mallouk, T. E. (2004). Ordered SBA-15 nanorod arrays inside a porous alumina membrane. *Journal of the American Chemical Society*, *126*(28), 8650-8651.

[8] Wang, H. S., Lin, L. H., Chen, S. Y., Wang, Y. L., & Wei, K. H. (2009). Ordered polythiophene/fullerene composite core shell nanorod arrays for solar cell applications. *Nanotechnology*, *20*(7), 075201.

[9] Chou, T. W. (2005). *Microstructural design of fiber composites*. Cambridge University Press.

[10] Whitney, T. M., Searson, P. C., Jiang, J. S., & Chien, C. L. (1993). Fabrication and magnetic properties of arrays of metallic nanowires.*Science*, *261*(5126), 1316-1319.

[11] Wernsdorfer, W., Doudin, B., Mailly, D., Hasselbach, K., Benoit, A., Meier, J., ... & Barbara, B. P. R. L. (1996). Nucleation of magnetization reversal in individual nanosized nickel wires. *Physical review letters*, *77*(9), 1873.

[12] Fosa, G., BĂdescu, R., & CĂlugĂru, G. (2004). On the time evolution of transmittivity in magnetic fluids. *Czechoslovak journal of physics*, *54*(9), 989-996.

[13] Tokarev, A., Gu, Y., Zakharchenko, A., Trotsenko, O., Luzinov, I., Kornev, K. G., & Minko, S. (2014). Reconfigurable Anisotropic Coatings via Magnetic Field-Directed Assembly and Translocation of Locking Magnetic Chains.*Advanced Functional Materials*, *24*(30), 4738-4745.

[14] Wen-Xiao, F., Zhen-Hui, H., Xue-Qing, X., & Hui, S. (2005). Aligned structures of Fe3O4 nanoparticles in a curable polymer carrier induced by a magnetic field. *Chinese Physics Letters*, *22*(9), 2386.

[15] Ferk, G., Krajnc, P., Hamler, A., Mertelj, A., Cebollada, F., Drofenik, M., & Lisjak, D. (2015). Monolithic Magneto-Optical Nanocomposites of Barium Hexaferrite Platelets in PMMA. *Scientific reports*, *5*.

[16] Marson, R. L., Kuanr, B. K., Mishra, S. R., Camley, R. E., & Celinski, Z. (2007). Nickel nanowires for planer microwave circuit applications and characterization. *JOURNAL OF VACUUM SCIENCE AND TECHNOLOGY B MICROELECTRONICS AND NANOMETER STRUCTURES*, *25*(6), 2619.

[17] Kartopu, G., Yalçın, O., Kazan, S., & Aktaş, B. (2009). Preparation and FMR analysis of Co nanowires in alumina templates. *Journal of Magnetism and Magnetic Materials*, *321*(9), 1142-1147.

[18] Kuanr, B. K., Marson, R., Mishra, S. R., Kuanr, A. V., Camley, R. E., & Celinski, Z. J. (2009). Gigahertz frequency tunable noise suppressor using nickel nanorod arrays and Permalloy films. *Journal of Applied Physics*,*105*(7), 07A520.

[19] Carignan, L. P., Yelon, A., Menard, D., & Caloz, C. (2011). Ferromagnetic nanowire metamaterials: Theory and applications. *Microwave Theory and Techniques, IEEE Transactions on*, *59*(10), 2568-2586.

[20] Kuanr, B. K., Veerakumar, V., Marson, R., Mishra, S. R., Camley, R. E., & Celinski, Z. (2009). Nonreciprocal microwave devices based on magnetic nanowires. *Appl. Phys. Lett*, *94*(20), 202505.

[21] Kou, X., Fan, X., Zhu, H., & Xiao, J. Q. (2009). Tunable ferromagnetic resonance in NiFe nanowires with strong magnetostatic interaction. *Applied Physics Letters*, *94*(11), 2509.

[22] Medina, J. D. L. T., Piraux, L., & Encinas, A. (2010). Tunable zero field ferromagnetic resonance in arrays of bistable magnetic nanowires. *Applied Physics Letters*, *96*(4), 042504.

[23] Gu, Y. (2014). Composite Films with Magnetic Nanorods: Fundamentals, Processing and Applications. PhD thesis.

[24] Kittel, C. (1998). Fifty years of ferromagnetic single-domain theory. *Journal of Geophysical Research: Solid Earth*, *103*(B12), 30533-30536.

[25] Landau, L. D., Bell, J. S., Kearsley, M. J., Pitaevskii, L. P., Lifshitz, E. M., & Sykes, J. B. (1984). *Electrodynamics of continuous media* (Vol. 8). elsevier.

[26] Sellmyer, D. J., Zheng, M., & Skomski, R. (2001). Magnetism of Fe, Co and Ni nanowires in self-assembled arrays. *Journal of Physics: Condensed Matter*, *13*(25), R433.

[27] Huang, H., Liu, C. H., Wu, Y., & Fan, S. (2005). Aligned carbon nanotube composite films for thermal management. *Advanced materials*, *17*(13), 1652-1656.

[28] X. Wang, Micro/nano Mechanical Characterization of One-dimensional Nanomaterials and Biomaterials (ProQuest, 2008).

[29] G. Motz and R. K. Bordia, Handbook of Textile Fibre Structure: Natural, Regenerated, Inorganic and Specialist Fibres **2**, 378 (2009).

[30] Yajima, S., OKAMURA, K., HAYASHI, J., & OMORI, M. (1976). Synthesis of continuous SiC fibers with high tensile strength. *Journal of the American Ceramic Society*, *59*(7-8), 324-327.

[31] Charlet, K., Jernot, J. P., Gomina, M., Bizet, L., & Bréard, J. (2010). Mechanical properties of flax fibers and of the derived unidirectional composites. *Journal of Composite Materials*, *44*(24), 2887-2896.

[32] Curtin, W. A., Netravali, A. N., & Park, J. M. (1994). Strength distribution of Carborundum polycrystalline SiC fibres as derived from the single-fibre-composite test. *Journal of materials science, 29*(18), 4718-4728.

[33] Wang, Y., & Xia, Y. (1998). The effects of strain rate on the mechanical behaviour of kevlar fibre bundles: an experimental and theoretical study.*Composites Part A: Applied Science and Manufacturing*, *29*(11), 1411-1415.

[34] Oulton, R.F., Sorger, V.J., Zentgraf, T., Ma, R.M., Gladden, C., Dai, L., Bartal, G., and Zhang, X. (2009). Plasmon lasers at deep subwavelength scale. Nature *461*, 629-632.

[35] Sehested, J. (2006). Four challenges for nickel steam-reforming catalysts. *Catalysis Today*, *111*(1), 103-110.

[36] Joo, S. H., Park, J. Y., Tsung, C. K., Yamada, Y., Yang, P., & Somorjai, G. A. (2009). Thermally stable Pt/mesoporous silica core–shell nanocatalysts for high-temperature reactions. *Nature materials*, *8*(2), 126-131.

[37] Arnal, P. M., Comotti, M., & Schüth, F. (2006). High-Temperature-Stable Catalysts by Hollow Sphere Encapsulation. *Angewandte Chemie*, *118*(48), 8404-8407.

[38] Joo, S. H., Park, J. Y., Tsung, C. K., Yamada, Y., Yang, P., & Somorjai, G. A. (2009). Thermally stable Pt/mesoporous silica core–shell nanocatalysts for high-temperature reactions. *Nature materials*, *8*(2), 126-131.

[39] Arnal, P. M., Comotti, M., & Schüth, F. (2006). High-Temperature-Stable Catalysts by Hollow Sphere Encapsulation. *Angewandte Chemie*, *118*(48), 8404-8407.

[40] Bartholomew, C. H. (2001). Mechanisms of catalyst deactivation. *Applied Catalysis A: General*, *212*(1), 17-60.

[41] Datye, A. K., Xu, Q., Kharas, K. C., & McCarty, J. M. (2006). Particle size distributions in heterogeneous catalysts: What do they tell us about the sintering mechanism?. *Catalysis today*, *111*(1), 59-67.

[42] Campbell, C. T., Parker, S. C., & Starr, D. E. (2002). The effect of size-dependent nanoparticle energetics on catalyst sintering. *Science*, *298*(5594), 811-814.

[43] Harris, P. J. F. (1995). Growth and structure of supported metal catalyst particles. *International materials reviews*, *40*(3), 97-115.

[44] Adamson, A.W., Gast, A.P., and NetLibrary Inc. (1997). Physical chemistry of surfaces. 6th Edition. (New York: Wiley), pp. xxi, 784 p.

[45] Fischer, F.D., Waitz, T., Vollath, D., and Simha, N.K. (2008). On the role of surface energy and surface stress in phase-transforming nanoparticles. Progress in Materials Science *53*, 481-527.

[46] Rusanov, A.I. (2005). Surface thermodynamics revisited. Surface Science Reports *58*, 111-239.

[47] Kozuka, H., Takenaka, S., Tokita, H., Hirano, T., Higashi, Y., & Hamatani, T. (2003). Stress and cracks in gel-derived ceramic coatings and thick film formation. *Journal of sol-gel science and technology*, *26*(1-3), 681-686.

[48] Atkinson, A., & Guppy, R. M. (1991). Mechanical stability of sol-gel films.*Journal of materials science*, *26*(14), 3869-3873.

[49] Brinker, C. J., Hurd, A. J., Schunk, P. R., Frye, G. C., & Ashley, C. S. (1992). Review of sol-gel thin film formation. *Journal of Non-Crystalline Solids*, *147*, 424-436.

[50] Chen, S. Y., & Chen, I. W. (1995). Cracking during Pyrolysis of Oxide Thin Films-Phenomenology, Mechanisms, and Mechanics. *Journal of the American Ceramic Society*, *78*(11), 2929-2939.

[51] Xia, Z. C., & Hutchinson, J. W. (2000). Crack patterns in thin films. *Journal of the Mechanics and Physics of Solids*, *48*(6), 1107-1131.

[52] Stillwagon, L. E., & Larson, R. G. (1988). Fundamentals of topographic substrate leveling. *Journal of applied physics*, *63*(11), 5251-5258.

[53] Stillwagon, L. E., Larson, R. G., & Taylor, G. N. (1987). Planarization of substrate topography by spin coating. *Journal of the Electrochemical Society*, *134*(8), 2030-2037.

[54] Peurrung, L. M., & Graves, D. B. (1991). Film thickness profiles over topography in spin coating. *Journal of the electrochemical society*, *138*(7), 2115-2124.

[55] Decré, M. M., & Baret, J. C. (2003). Gravity-driven flows of viscous liquids over two-dimensional topographies. *Journal of Fluid Mechanics*, *487*, 147-166.

[56] Stillwagon, L. E., & Larson, R. G. (1990). Leveling of thin films over uneven substrates during spin coating. *Physics of Fluids A: Fluid Dynamics (1989-1993)*, *2*(11), 1937-1944.

[57] Peurrung, L. M., & Graves, D. B. (1993). Spin coating over topography.*Semiconductor Manufacturing, IEEE Transactions on*, *6*(1), 72-76.

[58] Pozrikidis, C., & Thoroddsen, S. T. (1991). The deformation of a liquid film flowing down an inclined plane wall over a small particle arrested on the wall.*Physics of Fluids A: Fluid Dynamics (1989-1993)*, *3*(11), 2546-2558.

[59] An, J. W., You, D. H., & Lim, D. S. (2003). Tribological properties of hot-pressed alumina–CNT composites. *Wear*, *255*(1), 677-681.

[60] Liu, Y., & Gao, L. (2005). A study of the electrical properties of carbon nanotube-NiFe 2 O 4 composites: effect of the surface treatment of the carbon nanotubes. *Carbon*, *43*(1), 47-52.

[61] Wu, J. J., & Liu, S. C. (2002). Low-temperature growth of well-aligned ZnO nanorods by chemical vapor deposition. *Advanced Materials*, *14*(3), 215.

[62] Limmer, S. J., Seraji, S., Wu, Y., Chou, T. P., Nguyen, C., & Cao, G. Z. (2002). Template-based growth of various oxide nanorods by sol-gel electrophoresis. *Advanced Functional Materials*, *12*(1), 59-64.

[63] Takahashi, K., Limmer, S. J., Wang, Y., & Cao, G. (2004). Synthesis and electrochemical properties of single-crystal V2O5 nanorod arrays by template-based electrodeposition. *The Journal of Physical Chemistry B,108*(28), 9795-9800.

[64] Sun, Y., Fuge, G. M., & Ashfold, M. N. (2004). Growth of aligned ZnO nanorod arrays by catalyst-free pulsed laser deposition methods. *Chemical Physics Letters*, *396*(1), 21-26.

[65] Wang, J. X., Sun, X. W., Yang, Y., Huang, H., Lee, Y. C., Tan, O. K., & Vayssieres, L. (2006). Hydrothermally grown oriented ZnO nanorod arrays for gas sensing applications. *Nanotechnology*, *17*(19), 4995.

[66] Levin, I., Li, J., Slutsker, J., & Roytburd, A. L. (2006). Design of Self-Assembled Multiferroic Nanostructures in Epitaxial Films. *Advanced Materials*, *18*(15), 2044-2047.

[69] Gu, Y., & Kornev, K. G. (2013). Alignment of magnetic nanorods in solidifying films. *Particle & Particle Systems Characterization*, *30*(11), 958-963.

[70] Brinker, C. J., & Scherer, G. W. (2013). *Sol-gel science: the physics and chemistry of sol-gel processing*. Academic press.

[71] Chen, Z., Zhang, Z., Tsai, C. C., Kornev, K., Luzinov, I., Fang, M., & Peng, F. (2015). Electrospun mullite fibers from the sol–gel precursor. *Journal of Sol-Gel Science and Technology*, *74*(1), 208-219.

[72] Kickelbick, G., & Martucci, A. (2014). *Sol-Gel Nanocomposites*. M. Guglielmi (Ed.). Springer.

[73] Chakravorty, A. K. (1994). Effect of pH on 980°C spinel phase-mullite formation of Al2O3-SiO2 gels. *Journal of materials science*, *29*(6), 1558-1568.

[74] Cividanes, L. S., Campos, T. M., Rodrigues, L. A., Brunelli, D. D., & Thim, G. P. (2010). Review of mullite synthesis routes by sol–gel method. *Journal of Sol-Gel Science and Technology*, *55*(1), 111-125.

[75] Aksay, I. A., Dabbs, D. M., & Sarikaya, M. (1991). Mullite for structural, electronic, and optical applications. Journal of the American Ceramic Society, 74(10), 2343-2358.

[76] Kriven, W. M., Palko, J. W., Sinogeikin, S., Bass, J. D., Sayir, A., Brunauer, G., ... & Schneider, J. (1999). High temperature single crystal properties of mullite. Journal of the European Ceramic Society, 19(13), 2529-2541.

[77] Dokko, P. C., Pask, J. A., & Mazdiyasni, K. S. (1977). High-Temperature Mechanical Properties of Mullite Under Compression. Journal of the American Ceramic Society, 60(3-4), 150-155.

[78] Miller, R. A. (1997). Thermal barrier coatings for aircraft engines: history and directions. Journal of thermal spray technology, 6(1), 35-42.

[79] Lee, K. N. (2000). Current status of environmental barrier coatings for Si-based ceramics. Surface and Coatings Technology, 133, 1-7.[80] Schneider, H., & Okada, K. (1994). Mullite and mullite ceramics. *John Wiley & Sons*.

[81] Rodeghiero, E. D., Tse, O. K., Chisaki, J., & Giannelis, E. P. (1995). Synthesis and properties of Ni-α-Al 2 O 3 composites via sol-gel. *Materials Science and Engineering: A*, *195*, 151-161.

[82] Wang, H., Sekino, T., Niihara, K., & Fu, Z. (2009). Preparation of mullite-based iron magnetic nanocomposite powders by reduction of solid solution.*Journal of materials science*, *44*(10), 2489-2496.

[83] Baur, J., & Silverman, E. (2007). Challenges and opportunities in multifunctional nanocomposite structures for aerospace applications. *MRS bulletin*, *32*(04), 328-334.

[84] Trotsenko, O., Tokarev, A., Gruzd, A., Enright, T., & Minko, S. (2015). Magnetic field assisted assembly of highly ordered percolated nanostructures and their application for transparent conductive thin films. *Nanoscale*, *7*(16), 7155-7161.

[85] Libanori, R., Erb, R. M., & Studart, A. R. (2013). Mechanics of platelet-reinforced composites assembled using mechanical and magnetic stimuli.*ACS applied materials & interfaces*, *5*(21), 10794-10805.

[86] Li, S., Lin, M. M., Toprak, M. S., Kim, D. K., & Muhammed, M. (2010). Nanocomposites of polymer and inorganic nanoparticles for optical and magnetic applications. *Nano reviews*, *1*.

[87] Gu, Y., & Kornev, K. G. (2013). Alignment of magnetic nanorods in solidifying films. *Particle & Particle Systems Characterization*, *30*(11), 958-963.

[88] Teo, W. E., & Ramakrishna, S. (2006). A review on electrospinning design and nanofibre assemblies. *Nanotechnology*, *17*(14), R89.

[89] Li, D., McCann, J. T., Xia, Y., & Marquez, M. (2006). Electrospinning: a simple and versatile technique for producing ceramic nanofibers and nanotubes. *Journal of the American Ceramic Society*, *89*(6), 1861-1869.

[90] Ramaseshan, R., Sundarrajan, S., Jose, R., & Ramakrishna, S. (2007). Nanostructured ceramics by electrospinning. *Journal of Applied Physics*,*102*(11), 111101.

[91] Lin, D., Wu, H., Zhang, R., & Pan, W. (2009). Enhanced photocatalysis of electrospun Ag− ZnO heterostructured nanofibers. *Chemistry of Materials*,*21*(15), 3479-3484.

[92] Yu, P. C., Yang, R. J., Tsai, Y. Y., Sigmund, W., & Yen, F. S. (2011). Growth mechanism of single-crystal α-Al 2 O 3 nanofibers fabricated by electrospinning techniques. *Journal of the European Ceramic Society*, *31*(5), 723-731.

[93] Kim, I. D., Rothschild, A., Lee, B. H., Kim, D. Y., Jo, S. M., & Tuller, H. L. (2006). Ultrasensitive chemiresistors based on electrospun TiO2 nanofibers.*Nano Letters*, *6*(9), 2009-2013.

[94] Chen, Z., & Peng, F. (2014). Normal and Abnormal Grain Growths in BaTiO3 Fibers. *Journal of the American Ceramic Society*, *97*(9), 2755-2761.

[95] Zhu, Y., Zhang, J. C., Zhai, J., & Jiang, L. (2006). Preparation of superhydrophilic α-Fe 2 O 3 nanofibers with tunable magnetic properties.*Thin Solid Films*, *510*(1), 271-274.

[96] Cherian, C. T., Sundaramurthy, J., Reddy, M. V., Suresh Kumar, P., Mani, K., Pliszka, D., ... & Chowdari, B. V. R. (2013). Morphologically robust NiFe2O4 nanofibers as high capacity Li-ion battery anode material. *ACS applied materials & interfaces*, *5*(20), 9957-9963.

[97] Dong, G., Xiao, X., Chi, Y., Qian, B., Liu, X., Ma, Z., ... & Qiu, J. (2010). Size-dependent polarized photoluminescence from Y 3 Al 5 O 12: Eu3+ single crystalline nanofiber prepared by electrospinning. *Journal of Materials Chemistry*, *20*(8), 1587-1593.

[98] Wu, H., Sun, Y., Lin, D., Zhang, R., Zhang, C., & Pan, W. (2009). GaN nanofibers based on electrospinning: facile synthesis, controlled assembly, precise doping, and application as high performance UV photodetector.*Advanced Materials*, *21*(2), 227-231.

[99] Hao, Y. J., Jin, G. Q., Han, X. D., & Guo, X. Y. (2006). Synthesis and characterization of bamboo-like SiC nanofibers. *Materials Letters*, *60*(11), 1334-1337.

[100] Ghelich, R., Aghdam, R. M., Torknik, F. S., Jahannama, M. R., & Keyanpour-Rad, M. (2015). Carbothermal reduction synthesis of ZrB 2 nanofibers via pre-oxidized electrospun zirconium n-propoxide. *Ceramics International*, *41*(5), 6905-6911.

[101] Wu, H., Pan, W., Lin, D., & Li, H. (2012). Electrospinning of ceramic nanofibers: fabrication, assembly and applications. *Journal of Advanced Ceramics*, *1*(1), 2-23.

[102] Subbiah, T., Bhat, G. S., Tock, R. W., Parameswaran, S., & Ramkumar, S. S. (2005). Electrospinning of nanofibers. *Journal of Applied Polymer Science*, *96*(2), 557-569.

[103] Sigmund, W., Yuh, J., Park, H., Maneeratana, V., Pyrgiotakis, G., Daga, A., ... & Nino, J. C. (2006). Processing and structure relationships in electrospinning of ceramic fiber systems. *Journal of the American Ceramic Society*, *89*(2), 395-407.

[104] Pongsorrarith, V., Srisitthiratkul, C., Laohhasurayotin, K., & Intasanta, N. (2012). Solution-and air-recoverable photocatalytic nanofibers by facile and cost-effective electrospinning and co-precipitation processes. *Materials Letters*, *67*(1), 1-4.

[105] Kim, G. D., Lee, D. A., Lee, H. I., & Yoon, S. J. (1993). A study on the development of mullitent fibers using the sol-gel process. *Materials Science and Engineering: A*, *167*(1), 171-178.

[106] Al-Assafi, S., Cruse, T., Simmons, J. H., Brennan, A. B., & Sacks, M. D. (1994). Sol-Gel Processing of Continuous Mullite Fibers. In *Proceedings of the 18th Annual Conference on Composites and Advanced Ceramic Materials-B: Ceramic Engineering and Science Proceedings, Volume 15, Issue 5* (pp. 1060-1067). John Wiley & Sons, Inc..

[107] Song, K. C. (1998). Preparation of mullite fibers from aluminum isopropoxide–aluminum nitrate–tetraethylorthosilicate solutions by sol–gel method. *Materials Letters*, *35*(5), 290-296.

[108] Chen, Z., Zhang, Z., Tsai, C. C., Kornev, K., Luzinov, I., Fang, M., & Peng, F. (2015). Electrospun mullite fibers from the sol–gel precursor. *Journal of Sol-Gel Science and Technology*, *74*(1), 208-219.

[109] Pan, H., Li, L., Hu, L., & Cui, X. (2006). Continuous aligned polymer fibers produced by a modified electrospinning method. *Polymer*, *47*(14), 4901-4904.

[110] Dalton, P. D., Klee, D., & Möller, M. (2005). Electrospinning with dual collection rings. *Polymer*, *46*(3), 611-614.

[111] Bornat A. Production of electrostatically spun products. US Patent 4689186. 1987.

[112] Theron, A., Zussman, E., & Yarin, A. L. (2001). Electrostatic field-assisted alignment of electrospun nanofibres. *Nanotechnology*, *12*(3), 384.

[113] Tsai, C. C., Mikes, P., Andrukh, T., White, E., Monaenkova, D., Burtovyy, O., ... & Kornev, K. G. (2011). Nanoporous artificial proboscis for probing minute amount of liquids. *Nanoscale*, *3*(11), 4685-4695.

[114] Brinker, C. J., Frye, G. C., Hurd, A. J., & Ashley, C. S. (1991). Fundamentals of sol-gel dip coating. *Thin Solid Films*, *201*(1), 97-108.

[115] Viazzi, C., Bonino, J. P., & Ansart, F. (2006). Synthesis by sol-gel route and characterization of Yttria Stabilized Zirconia coatings for thermal barrier applications. *Surface and Coatings Technology*, *201*(7), 3889-3893.

[116] Kanzaki, S., Tabata, H., Kumazawa, T., & Ohta, S. (1985). Sintering and mechanical properties of stoichiometric mullite. Journal of the American Ceramic Society, 68(1), C-6.

[117] Chawla, K. K., Xu, Z. R., & Ha, J. S. (1996). Processing, structure, and properties of mullite fiber/mullite matrix composites. *Journal of the European Ceramic Society*, *16*(2), 293-299.

[118] Schneider, H., Schreuer, J., & Hildmann, B. (2008). Structure and properties of mullite—a review. *Journal of the European Ceramic Society*,*28*(2), 329-344.

[119] Merrill, G. B., & Morrison, J. A. (2000). *U.S. Patent No. 6,013,592*. Washington, DC: U.S. Patent and Trademark Office.

[120] Yogo, T., & Aksay, I. A. (1994). Synthesis of mullite fibre from an aluminosiloxane precursor. *Journal of Materials Chemistry*, *4*(2), 353-359.

[121] Formo, E., Lee, E., Campbell, D., & Xia, Y. (2008). Functionalization of electrospun TiO2 nanofibers with Pt nanoparticles and nanowires for catalytic applications. *Nano Letters*, *8*(2), 668-672.

[122] De Jong, K. P., & Geus, J. W. (2000). Carbon nanofibers: catalytic synthesis and applications. *Catalysis Reviews*, *42*(4), 481-510.

[123] Chronakis, I. S. (2005). Novel nanocomposites and nanoceramics based on polymer nanofibers using electrospinning process—a review. *Journal of Materials Processing Technology*, *167*(2), 283-293.

[124] Li, D., & Xia, Y. (2004). Electrospinning of nanofibers: reinventing the wheel?. *Advanced materials*, *16*(14), 1151-1170.

[125] Dai, Y., Liu, W., Formo, E., Sun, Y., & Xia, Y. (2011). Ceramic nanofibers fabricated by electrospinning and their applications in catalysis, environmental science, and energy technology. *Polymers for Advanced Technologies*, *22*(3), 326-338.

[126] Sekino, T., & Niihara, K. (1995). Microstructural characteristics and mechanical properties for Al 2 O 3/metal nanocomposities. *Nanostructured materials*, *6*(5), 663-666.

[127] Das, A., Raffi, M., Megaridis, C., Fragouli, D., Innocenti, C., & Athanassiou, A. (2015). Magnetite (Fe3O4)-filled carbon nanofibers as electro-conducting/superparamagnetic nanohybrids and their multifunctional polymer composites. *Journal of Nanoparticle Research*, *17*(1), 1-14.

[128] Kondo, H., Sekino, T., Tanaka, N., Nakayama, T., Kusunose, T., & Niihara, K. (2005). Mechanical and Magnetic Properties of Novel Yttria-Stabilized Tetragonal Zirconia/Ni

Nanocomposite Prepared by the Modified Internal Reduction Method. *Journal of the American Ceramic Society*, *88*(6), 1468-1473.

[129] Moya, J. S., Lopez-Esteban, S., & Pecharromán, C. (2007). The challenge of ceramic/metal microcomposites and nanocomposites. *Progress in materials science*, *52*(7), 1017-1090.

[130] Nawa, M., Sekino, T., & Niihara, K. (1994). Fabrication and mechanical behaviour of Al2O3/Mo nanocomposites. *Journal of Materials Science*,*29*(12), 3185-3192.

[131] Takahashi, H., Sunagawa, Y., Myagmarjav, S., Yamamoto, K., Sato, N., & Muramatsu, A. (2003). Reductive deposition of Ni-Zn nanoparticles selectively on TiO2 fine particles in the liquid phase. *Materials Transactions*,*44*(11), 2414-2416.

[132] Yoshinaga, M., Takahashi, H., Yamamoto, K., Muramatsu, A., & Morikawa, T. (2007). Formation of metallic Ni nanoparticles on titania surfaces by chemical vapor reductive deposition method. *Journal of colloid and interface science*, *309*(1), 149-154.

[133] Palgrave, R. G., & Parkin, I. P. (2006). Aerosol assisted chemical vapor deposition using nanoparticle precursors: a route to nanocomposite thin films. *Journal of the American Chemical Society*, *128*(5), 1587-1597.

[134] Barnes, J. P., Petford-Long, A. K., Doole, R. C., Serna, R., Gonzalo, J., Suarez-Garcia, A., ... & Hole, D. (2002). Structural studies of Ag nanocrystals embedded in amorphous Al2O3 grown by pulsed laser deposition.*Nanotechnology*, *13*(4), 465.

[135] Krompiec, S., Mrowiec-Białoń, J., Skutil, K., Dukowicz, A., Pająk, L., & Jarzębski, A. B. (2003). Nickel–alumina composite aerogel catalysts with a high nickel load: a novel fast

sol–gel synthesis procedure and screening of catalytic properties. *Journal of non-crystalline solids*, *315*(3), 297-303.

[136] Hernández-Torres, J., & Mendoza-Galván, A. (2005). Optical properties of sol–gel SiO 2 films containing nickel. *Thin Solid Films*, *472*(1), 130-135.

[137] Awano, M., Sando, M., & Niihara, K. (1998). Synthesis of nanocomposite ceramics for magnetic remote sensing and actuating. *Key Engineering Materials*, *161*, 485-488.

[138] White, J. T., Reimanis, I. E., Tong, J., O'Brien, J. R., & Morrissey, A. (2012). Internal Reduction of Ni2+ in ZrO2 Stabilized with 10 mol% Y2O3 Examined with VSM and SQUID Magnetometry. *Journal of the American Ceramic Society*, *95*(12), 4008-4014.

[139] Sekino, T., Nakajima, T., Ueda, S., & Niihara, K. (1997). Reduction and Sintering of a Nickel–Dispersed-Alumina Composite and Its Properties. *Journal of the American Ceramic Society*, *80*(5), 1139-1148.

[140] Oulton, R.F., Sorger, V.J., Zentgraf, T., Ma, R.M., Gladden, C., Dai, L., Bartal, G., and Zhang, X. (2009). Plasmon lasers at deep subwavelength scale. Nature *461*, 629-632.

[141] Sehested, J. (2006). Four challenges for nickel steam-reforming catalysts. *Catalysis Today*, *111*(1), 103-110.

[142] Guerrero-Martínez, A., Pérez-Juste, J., & Liz-Marzán, L. M. (2010). Recent progress on silica coating of nanoparticles and related nanomaterials. *Advanced materials*, *22*(11), 1182-1195.

[143] Zhang, N., Liu, S., & Xu, Y. J. (2012). Recent progress on metal core@ semiconductor shell nanocomposites as a promising type of photocatalyst. *Nanoscale*, *4*(7), 2227-2238.

[144] Eshelby, J.D. (1956). The Continuum Theory of Lattice Defects. Solid State Physics-Advances in Research and Applications *3*, 79-144.

[145] Bimberg, D., Grundmann, M., and Ledentsov, M.N. (1999). Quantum Dot Heterostructures. , (Chichester: John Wiley & Sons).

[146] Lim, C.W., Li, Z.R., and He, L.H. (2006). Size dependent, non-uniform elastic field inside a nano-scale spherical inclusion due to interface stress. International Journal of Solids and Structures *43*, 5055-5065.

[147] Yang, F.Q. (2004). Size-dependent effective modulus of elastic composite materials: Spherical nanocavities at dilute concentrations. Journal of Applied Physics *95*, 3516-3520.

[148] Kozuka, H. (2006). Stress evolution on gel-to-ceramic thin film conversion.*Journal of sol-gel science and technology*, *40*(2-3), 287-297.

[149] Kozuka, H., & Takenaka, S. (2002). Single-Step Deposition of Gel-Derived Lead Zirconate Titanate Films: Critical Thickness and Gel Film to Ceramic Film Conversion. *Journal of the American Ceramic Society*, *85*(11), 2696-2702.

[150] Jing, C., Zhao, X., & Zhang, Y. (2007). Sol–gel fabrication of compact, crack-free alumina film. *Materials research bulletin*, *42*(4), 600-608.

[151] Schmidt, H., Rinn, G., Naβ, R., & Sporn, D. (1988). Film preparation by inorganic-organic sol-gel synthesis. In *MRS Proceedings* (Vol. 121, p. 743). Cambridge University Press.

[152] Kozuka, H., & Kajimura, M. (2000). Single-Step Dip Coating of Crack-Free BaTiO3 Films> 1 μm Thick: Effect of Poly (vinylpyrrolidone) on Critical Thickness. *Journal of the American Ceramic Society*, *83*(5), 1056-1062.

[153] Du, Z. H., & Ma, J. (2006). The effect of PVP on the critical thickness and properties of PLZT ceramic films. *Journal of electroceramics*, *16*(4), 565-569.

[154] Kozuka, H., Kajimura, M., Hirano, T., & Katayama, K. (2000). Crack-free, thick ceramic coating films via non-repetitive dip-coating using polyvinylpyrrolidone as stress-relaxing agent. *Journal of Sol-Gel Science and Technology*, *19*(1-3), 205-209.

[155] Chen, Y. Y., & Wei, W. C. J. (2001). Formation of mullite thin film via a sol-gel process with polyvinylpyrrolidone additive. *Journal of the European Ceramic Society*, *21*(14), 2535-2540.

[156] Wang, N., Yang, X. Z., Li, J. B., Lin, H., & Chi, B. (2004, December). Fabrication and characterization of porous mullite coating on porous silicon carbide support. In *Key Engineering Materials* (Vol. 280, pp. 1301-1304).

[157] Ansar, S. A., Bhattacharya, S., Dutta, S., Ghosh, S. S., & Mukhopadhyay, S. (2010). Development of mullite and spinel coatings on graphite for improved water-wettability and oxidation resistance. *Ceramics International*, *36*(6), 1837-1844.

[158] Jayasankar, M., Anilkumar, G. M., Smitha, V. S., Mukundan, P., Madhusoodana, C. D., & Warrier, K. G. K. (2011). Low temperature needle like mullite grain formation in sol–gel precursors coated on SiC porous substrates. *Thin Solid Films*, *519*(22), 7672-7676.

[159] Teo, W. E., & Ramakrishna, S. (2009). Electrospun nanofibers as a platform for multifunctional, hierarchically organized nanocomposite. *Composites Science and Technology*, *69*(11), 1804-1817.

[160] Gu, Y., & Kornev, K. G. (2016). Ferromagnetic Nanorods in Applications to Control of the In-Plane Anisotropy of Composite Films and for In Situ Characterization of the Film Rheology. *Advanced Functional Materials*.

[161] Gu, Y., Burtovyy, R., Townsend, J., Owens, J. R., Luzinov, I., & Kornev, K. G. (2013). Collective alignment of nanorods in thin Newtonian films. *Soft Matter*, *9*(35), 8532-8539.

[162] Gupta, M. K., Kulkarni, D. D., Geryak, R., Naik, S., & Tsukruk, V. V. (2012). A robust and facile approach to assembling mobile and highly-open unfrustrated triangular lattices from ferromagnetic nanorods. *Nano letters*,*13*(1), 36-42.

[163] Murphy, C. J., & Orendorff, C. J. (2005). Alignment of gold nanorods in polymer composites and on polymer surfaces. *Advanced Materials*, *17*(18), 2173-2177.

[164] Gupta, S., Zhang, Q., Emrick, T., & Russell, T. P. (2006). "Self-corralling" nanorods under an applied electric field. *Nano letters*, *6*(9), 2066-2069.

[165] Li, D., Wang, Y., & Xia, Y. (2003). Electrospinning of polymeric and ceramic nanofibers as uniaxially aligned arrays. *Nano letters*, *3*(8), 1167-1171.

[166] Dzenis, Y. A. (2004). Spinning continuous fibers for nanotechnology.

[167] Chen, Z., Gu, Y., Aprelev, P., Kornev, K., Luzinov, I., Chen, J., & Peng, F. (2016). Mullite–Nickel Magnetic Nanocomposite Fibers Obtained from Electrospinning Followed by Thermal Reduction. *Journal of the American Ceramic Society*.

[168] Zheludkevich, M. L., Serra, R., Montemor, M. F., Yasakau, K. A., Salvado, I. M., & Ferreira, M. G. S. (2005). Nanostructured sol–gel coatings doped with cerium nitrate as pre-treatments for AA2024-T3: corrosion protection performance. *Electrochimica Acta*, *51*(2), 208-217.

[169] Myers, T. G. (1998). Thin films with high surface tension. *Siam Review*,*40*(3), 441-462.

[170] Gaskell, P. H., Jimack, P. K., Sellier, M., & Thompson, H. M. (2006). Flow of evaporating, gravity-driven thin liquid films over topography. *Physics of Fluids (1994-present)*, *18*(1), 013601.

[171] Khayat, R. E., & Welke, S. R. (2001). Influence of inertia, gravity, and substrate topography on the two-dimensional transient coating flow of a thin Newtonian fluid film. *Physics of Fluids (1994-present)*, *13*(2), 355-367.

[172] Gramlich, C. M., Kalliadasis, S., Homsy, G. M., & Messer, C. (2002). Optimal leveling of flow over one-dimensional topography by Marangoni stresses. *Physics of Fluids (1994-present)*, *14*(6), 1841-1850.

[173] Saprykin, S., Koopmans, R. J., & Kalliadasis, S. (2007). Free-surface thin-film flows over topography: influence of inertia and viscoelasticity. *Journal of Fluid Mechanics*, *578*, 271-293.

[174] Kalliadasis, S., Bielarz, C., & Homsy, G. M. (2000). Steady free-surface thin film flows over topography. *Physics of Fluids (1994-present)*, *12*(8), 1889-1898.

[175] Wu, J., Lin, H., Li, J. B., Zhan, X. B., & Li, J. F. (2009). Fabrication and characterization of electrospun mullite nanofibers. *Materials Letters*, *63*(27), 2309-2312.

[176] Mohammad Ali Zadeh, M., Keyanpour-Rad, M., & Ebadzadeh, T. (2013). Synthesis of mullite nanofibres by electrospinning of solutions containing different proportions of polyvinyl butyral. *Ceramics International*, *39*(8), 9079-9084.

[177] Mohammad Alizadeh, M., Keyanpour-Rad, M., & Ebadzadeh, T. (2013). Effect of viscosity of polyvinyl alcohol solution on morphology of the electrospun mullite nanofibres. *Ceramics International*.

[178] X. Wang, Micro/nano Mechanical Characterization of One-dimensional Nanomaterials and Biomaterials (ProQuest, 2008).

[179] G. Motz and R. K. Bordia, Handbook of Textile Fibre Structure: Natural, Regenerated, Inorganic and Specialist Fibres **2**, 378 (2009).

[180] Yajima, S., OKAMURA, K., HAYASHI, J., & OMORI, M. (1976). Synthesis of continuous SiC fibers with high tensile strength. *Journal of the American Ceramic Society*, *59*(7-8), 324-327.

[181] Charlet, K., Jernot, J. P., Gomina, M., Bizet, L., & Bréard, J. (2010). Mechanical properties of flax fibers and of the derived unidirectional composites. *Journal of Composite Materials*, *44*(24), 2887-2896.

[182] Curtin, W. A., Netravali, A. N., & Park, J. M. (1994). Strength distribution of Carborundum polycrystalline SiC fibres as derived from the single-fibre-composite test. *Journal of materials science*, *29*(18), 4718-4728.

[183] Wang, Y., & Xia, Y. (1998). The effects of strain rate on the mechanical behaviour of kevlar fibre bundles: an experimental and theoretical study.*Composites Part A: Applied Science and Manufacturing*, *29*(11), 1411-1415.

[184] Lee, S. H., Tekmen, C., & Sigmund, W. M. (2005). Three-point bending of electrospun TiO 2 nanofibers. *Materials Science and Engineering: A*, *398*(1), 77-81.

[185] Inai, R., Kotaki, M., & Ramakrishna, S. (2005). Structure and properties of electrospun PLLA single nanofibres. *Nanotechnology*, *16*(2), 208.

[186] Tan, E. P. S., Goh, C. N., Sow, C. H., & Lim, C. T. (2005). Tensile test of a single nanofiber using an atomic force microscope tip. *Applied Physics Letters*, *86*(7), 073115.

[187] Bellan, L. M., Kameoka, J., & Craighead, H. G. (2005). Measurement of the Young's moduli of individual polyethylene oxide and glass nanofibres.*Nanotechnology*, *16*(8), 1095.

[188] Gu, Y., & Kornev, K. G. (2014). Attachment/detachment hysteresis of fiber-based magnetic grabbers. *Soft matter*, *10*(16), 2816-2824.

[189] Chen, Z., Gu, Y., Zhang, Z., Kornev, K. G., Luzinov, I., & Peng, F. (2015). Measuring flexural rigidity of mullite microfibers using magnetic droplets.*Journal of Applied Physics*, *117*(21), 214304.

[190] Chen, X., & Gu, L. (2009). Sol–gel dry spinning of mullite fibers from AN/TEOS/AIP system. *Materials Research Bulletin*, *44*(4), 865-873.

[191] Okada, K., Yasohama, S., Hayashi, S., & Yasumori, A. (1998). Sol–gel synthesis of mullite long fibres from water solvent systems. *Journal of the european ceramic society*, *18*(13), 1879-1884.

[192] Selvaraj, U., Komarneni, S., & Roy, R. (1993). Structural Differences in Mullite Xerogels from Different Precursors Characterized by ^{27}Al and ^{29}Si MASNMR. *Journal of Solid State Chemistry*, *106*(1), 73-82.

[193] Cassidy, D. J., Woolfrey, J. L., Bartlett, J. R., & Ben-Nissan, B. (1997). The effect of precursor chemistry on the crystallisation and densification of sol-gel derived mullite gels and powders. *Journal of Sol-Gel Science and Technology*,*10*(1), 19-30.

[194] Ban, T., Hayashi, S., Yasumori, A., & Okada, K. (1996). Characterization of low temperature mullitization. *Journal of the European Ceramic Society*, *16*(2), 127-132.

[195] L. D. Landau, E. M. Lifshitz, A. M. Kosevich, and L. P. Pitaevskii, Theory of Elasticity (Pergamon Press, 1986).

[196] Hench, L. L., & West, J. K. (1990). The sol-gel process. *Chemical Reviews*,*90*(1), 33-72.

[197] Blaine, R. L., & Kissinger, H. E. (2012). Homer Kissinger and the Kissinger equation. *Thermochimica acta*, *540*, 1-6.

[198] Kissinger, H. E. (1957). Reaction kinetics in differential thermal analysis.*Analytical chemistry*, *29*(11), 1702-1706.

[199] Okada, K., Kaneda, J. I., Kameshima, Y., Yasumori, A., & Takei, T. (2003). Crystallization kinetics of mullite from polymeric Al_2O_3–SiO_2 xerogels. *Materials Letters*, *57*(21), 3155-3159.

[200] Douy, A. (2006). Crystallisation of amorphous spray-dried precursors in the Al_2O_3–SiO_2 system. *Journal of the European Ceramic Society*, *26*(8), 1447-1454.

[201] Okada, K. (2008). Activation energy of mullitization from various starting materials. *Journal of the European Ceramic Society*, *28*(2), 377-382.

[202] LI, C. S., ZHANG, Y. J., & ZHANG, J. D. (2009). Polycrystalline Mullite Fibers Prepared by Sol-Gel Method. *Journal of Inorganic Materials*, *4*, 044.

[203] Chatterjee, M., Naskar, M. K., Chakrabarty, P. K., & Ganguli, D. (2002). Mullite fibre mats by a sol-gel spinning technique. *Journal of sol-gel science and technology*, *25*(2), 169-174.

[204] Schmücker, M., Flucht, F., & Schneider, H. (1996). High temperature behaviour of polycrystalline aluminosilicate fibres with mullite bulk composition. I. Microstructure and strength properties. *Journal of the European Ceramic Society*, *16*(2), 281-285.

[205] Salem, D. R. (2001). *Structure formation in polymeric fibers*. Hanser Verlag.

[206] Casula, M. F., Corrias, A., Falqui, A., Serin, V., Gatteschi, D., Sangregorio, C., ... & Battaglin, G. (2003). Characterization of FeCo-SiO2 nanocomposite films prepared by sol-gel dip coating. *Chemistry of materials*, *15*(11), 2201-2207.

[207] Ikeda, K., Kobayashi, K., & Fujimoto, M. (2002). Multilayer nanogranular magnetic thin films for GHz applications. *Journal of applied physics*, *92*, 5395-5400.

[208] Carles, V., Laurent, C., Brieu, M., & Rousset, A. (1999). Synthesis and characterization of Fe/Co/Ni alloys-MgO nanocomposite powders. *Journal of Materials Chemistry*, *9*(4), 1003-1009.

[209] Patterson, A. L. (1939). The Scherrer formula for X-ray particle size determination. *Physical review*, *56*(10), 978.

[210] Tkalcec, E., Kurajica, S., & Schmauch, J. (2007). Crystallization of amorphous Al_2O_3–SiO_2 precursors doped with nickel. *Journal of Non-Crystalline Solids*, *353*(30), 2837-2844.

[211] Okada, K., & ŌTSUKA, N. (1986). Characterization of the Spinel Phase from SiO2-Al2O3 Xerogels and the Formation Process of Mullite. *Journal of the American Ceramic Society*, *69*(9), 652-656.

[212] Brindley, G. W., & Nakahira, M. (1959). The Kaolinite-Mullite Reaction Series: III, The High-Temperature Phases. *Journal of the American Ceramic Society*, *42*(7), 319-324.

[213] Areán, C. O., & Viñuela, J. D. (1985). Structural study of copper-nickel aluminate (Cu x Ni 1− x Al 2 O 4) spinels. *Journal of Solid State Chemistry*,*60*(1), 1-5.

[214] Choi-Yim, H., & Johnson, W. L. (1997). Bulk metallic glass matrix composites. *Applied physics letters*, *71*(26), 3808-3810.

[215] J. Thermal Anal. 13, 1978 Page 5. AUGIS, BENNETT: AVRAMI PARAMETERS FOR HETEROGENEOUS REACTIONS.

[216] Hwang, J. H., Dravid, V. P., Teng, M. H., Host, J. J., Elliott, B. R., Johnson, D. L., & Mason, T. O. (1997). Magnetic properties of graphitically encapsulated nickel nanocrystals. *Journal of materials research*, *12*(04), 1076-1082.

[217] Wagner, W., Wiedenmann, A., Petry, W., Geibel, A., & Gleiter, H. (1991). Magnetic microstructure of nanostructured Fe, studied by small angle neutron scattering. *Journal of materials research*, *6*(11), 2305-2311.

[218] Host, J. J., Block, J. A., Parvin, K., Dravid, V. P., Alpers, J. L., Sezen, T., & LaDuca, R. (1998). Effect of annealing on the structure and magnetic properties of graphite encapsulated nickel and cobalt nanocrystals. *Journal of applied physics*, *83*(2), 793-801.

[219] Everman, R. L., & Cooper, R. F. (2003). Internal Reduction of an Iron-Doped Magnesium Aluminosilicate Melt. *Journal of the American Ceramic Society*, *86*(3), 487-494.

[220] Song, S. J., Liu, F., & Zhang, Z. H. (2014). Analysis of elastic–plastic accommodation due to volume misfit upon solid-state phase transformation. *Acta Materialia*, *64*, 266-281.

[221] Cheekatamarla, P. K., & Finnerty, C. M. (2006). Reforming catalysts for hydrogen generation in fuel cell applications. *Journal of Power Sources*, *160*(1), 490-499.

[222] Kolmakov, A., Chen, X., & Moskovits, M. (2008). Functionalizing nanowires with catalytic nanoparticles for gas sensing application. *Journal of nanoscience and nanotechnology*, *8*(1), 111-121.

[223] Zouhdi, S., Sihvola, A., and Vinogradov, A.P. eds. (2009). Metamaterials and Plasmonics: Fundamentals, Modelling, Applications (Netherlands Springer).

[224] Datye, A. K., Xu, Q., Kharas, K. C., & McCarty, J. M. (2006). Particle size distributions in heterogeneous catalysts: What do they tell us about the sintering mechanism?. *Catalysis today*, *111*(1), 59-67.

[225] Campbell, C. T., Parker, S. C., & Starr, D. E. (2002). The effect of size-dependent nanoparticle energetics on catalyst sintering. *Science*, *298*(5594), 811-814.

[226] Harris, P. J. F. (1995). Growth and structure of supported metal catalyst particles. *International materials reviews*, *40*(3), 97-115.

[227] Su, C. H., & Voorhees, P. W. (1996). The dynamics of precipitate evolution in elastically stressed solids—I. Inverse coarsening. *Acta materialia*,*44*(5), 1987-1999.

[228] Schmidt, I. (2001). Microstructural evolution in two-phase solids: morphological stability of near-periodic particle arrangements.*Computational materials science*, *22*(3), 333-344.

[229] Perez, D., & Lewis, L. J. (2007). Effect of elastic interactions on coarsening in elastically inhomogeneous multiphase systems. *Physical Review E*,*75*(4), 041602.

[230] Voorhees, P. W., & Johnson, W. C. (1986). Interfacial equilibrium during a first-order phase transformation in solids. *The Journal of chemical physics*, *84*(9), 5108-5121.

[231] Matos, J., Ono, L. K., Behafarid, F., Croy, J. R., Mostafa, S., DeLaRiva, A. T., ... & Cuenya, B. R. (2012). In situ coarsening study of inverse micelle-prepared Pt nanoparticles supported on γ-Al 2 O 3: pretreatment and environmental effects. *Physical Chemistry Chemical Physics*, *14*(32), 11457-11467.

[232] Howard, A., Mitchell, C. E. J., & Egdell, R. G. (2002). Real time STM observation of Ostwald ripening of Pd nanoparticles on TiO 2 (110) at elevated temperature. *Surface science*, *515*(2), L504-L508.

[233] Stone, P., Poulston, S., Bennett, R. A., & Bowker, M. (1998). Scanning tunnelling microscopy investigation of sintering in a model supported catalyst: nanoscale Pd on TiO 2 (110). *Chemical Communications*, (13), 1369-1370.

[234] Lifshitz, I. M., & Slyozov, V. V. (1961). The kinetics of precipitation from supersaturated solid solutions. *Journal of physics and chemistry of solids*,*19*(1-2), 35-50.

[235] Lim, C.W., Li, Z.R., and He, L.H. (2006). Size dependent, non-uniform elastic field inside a nano-scale spherical inclusion due to interface stress. International Journal of Solids and Structures *43*, 5055-5065.

[236] Yang, F.Q. (2004). Size-dependent effective modulus of elastic composite materials: Spherical nanocavities at dilute concentrations. Journal of Applied Physics *95*, 3516-3520.

[237] Fischer, F. D., Berveiller, M., Tanaka, K., & Oberaigner, E. R. (1994). Continuum mechanical aspects of phase transformations in solids. *Archive of Applied Mechanics*, *64*(2), 54-85.

[238] Fischer, F. D., & Oberaigner, E. R. (2001). A micromechanical model of phase boundary movement during solid–solid phase transformations. *Archive of Applied Mechanics*, *71*(2-3), 193-205.

[239] Dingreville, R., Qu, J.M., and Cherkaoui, M. (2005). Surface free energy and its effect on the elastic behavior of nano-sized particles, wires and films. Journal of the Mechanics and Physics of Solids *53*, 1827-1854.

[240] Goniakowski, J., Finocchi, F., and Noguera, C. (2008). Polarity of oxide surfaces and nanostructures. Reports on Progress in Physics *71*.

[241] Linford, R.G. (1972). Surface energy of solids. Chemical Society Reviews *1*, 445-464.

[242] Gu, Y., Chen, Z., Borodinov, N., Luzinov, I., Peng, F., & Kornev, K. G. (2014). Kinetics of evaporation and gel formation in thin films of ceramic precursors.*Langmuir*, *30*(48), 14638-14647.

[243] Beran, A., Voll, D., & Schneider, H. (2001). Dehydration and structural development of mullite precursors: an FTIR spectroscopic study. *Journal of the European Ceramic Society*, *21*(14), 2479-2485.

[244] Leivo, J., Lindén, M., Rosenholm, J. M., Ritola, M., Teixeira, C. V., Levänen, E., & Mäntylä, T. A. (2008). Evolution of aluminosilicate structure and mullite crystallization from homogeneous nanoparticulate sol–gel precursor with organic additives. *Journal of the European Ceramic Society*, *28*(9), 1749-1762.

[245] Mansur, H. S., Sadahira, C. M., Souza, A. N., & Mansur, A. A. (2008). FTIR spectroscopy characterization of poly (vinyl alcohol) hydrogel with different hydrolysis

degree and chemically crosslinked with glutaraldehyde. *Materials Science and Engineering: C*, *28*(4), 539-548.

[246] Schneider, H., & Eberhard, E. (1990). Thermal expansion of mullite. *Journal of the American Ceramic Society*, *73*(7), 2073-2076.

[247] Maissel, L. (1960). Thermal expansion of silicon. *Journal of Applied Physics*,*31*(1), 211-211.

[248] Zhang, Y., Ding, Y., Gao, J., & Yang, J. (2009). Mullite fibres prepared by sol–gel method using polyvinyl butyral. *Journal of the European Ceramic Society*, *29*(6), 1101-1107.

[249] Kasuya, R., Isobe, T., Kuma, H., & Katano, J. (2005). Photoluminescence enhancement of PEG-modified YAG: Ce3+ nanocrystal phosphor prepared by glycothermal method. *The Journal of Physical Chemistry B*,*109*(47), 22126-22130.

[250] Wang, H., Qiao, X., Chen, J., Wang, X., & Ding, S. (2005). Mechanisms of PVP in the preparation of silver nanoparticles. *Materials Chemistry and Physics*, *94*(2), 449-453.

[251] Thompson, C. V. (1990). Grain growth in thin films. *Annual Review of Materials Science*, *20*(1), 245-268.

[252] Koch, C. C. (2006). *Nanostructured materials: processing, properties and applications*. William Andrew.

[253] Yang, G. Z., Cui, H., Sun, Y., Gong, L., Chen, J., Jiang, D., & Wang, C. X. (2009). Simple catalyst-free method to the synthesis of β-SiC nanowires and their field emission properties. *The Journal of Physical Chemistry C*, *113*(36), 15969-15973.

[254] Shi, W., Zheng, Y., Peng, H., Wang, N., Lee, C. S., & Lee, S. T. (2000). Laser ablation synthesis and optical characterization of silicon carbide nanowires. *Journal of the American Ceramic Society*, *83*(12), 3228-3230.

[255] Becher, P. F., HSUEH, C. H., Angelini, P., & Tiegs, T. N. (1988). Toughening Behavior in Whisker-Reinforced Ceramic Matrix Composites.*Journal of the American Ceramic Society*, *71*(12), 1050-1061.

[256] Guicciardi, S., Silvestroni, L., Nygren, M., & Sciti, D. (2010). Microstructure and Toughening Mechanisms in Spark Plasma-Sintered ZrB2 Ceramics Reinforced by SiC Whiskers or SiC-Chopped Fibers. *Journal of the American Ceramic Society*, *93*(8), 2384-2391.

[257] Gao, L., Jin, X., Kawaoka, H., Sekino, T., & Niihara, K. (2002). Microstructure and mechanical properties of SiC–mullite nanocomposite prepared by spark plasma sintering. *Materials Science and Engineering: A*,*334*(1), 262-266.

[258] Riedel, R., Toma, L., Fasel, C., & Miehe, G. (2009). Polymer-derived mullite–SiC-based nanocomposites. *Journal of the European Ceramic Society*,*29*(14), 3079-3090.

[259] Gustafsson, S., Falk, L. K., Pitchford, J. E., Clegg, W. J., Lidén, E., & Carlström, E. (2009). Development of microstructure during creep of polycrystalline mullite and a nanocomposite mullite/5vol.% SiC. *Journal of the European Ceramic Society*, *29*(4), 539-550.

[260] Sorarù, G. D., Kleebe, H. J., Ceccato, R., & Pederiva, L. (2000). Development of mullite-SiC nanocomposites by pyrolysis of filled polymethylsiloxane gels. *Journal of the European Ceramic Society*, *20*(14), 2509-2517.

[261] Warrier, K. G. K., Kumar, G. A., & Ananthakumar, S. (2001). Densification and mechanical properties of mullite-SiC nanocomposites synthesized through sol-gel coated precursors. *Bulletin of Materials Science*, *24*(2), 191-195.

[262] Warrier, K. G. K., & Anilkumar, G. M. (2001). Densification of mullite–SiC nanocomposite sol–gel precursors by pressureless sintering. *Materials chemistry and physics*, *67*(1), 263-266.

[263] Townsend, James; Burtovyy, Dr. Ruslan; Kornez, Dr. Konstantin; and Luzinov, Dr. Igor, "Magnetically Responsive Silicon Carbide Whiskers for Enhanced Nanocomposite Materials" (2015). *Graduate Research and Discovery Symposium (GRADS)*. Paper 141.

[264] Letellier, D., Sandre, O., Ménager, C., Cabuil, V., & Lavergne, M. (1997). Magnetic tubules. *Materials Science and Engineering: C*, *5*(2), 153-162.

[265] Fresnais, J., Berret, J. F., Frka-Petesic, B., Sandre, O., & Perzynski, R. (2008). Electrostatic Co-Assembly of Iron Oxide Nanoparticles and Polymers: Towards the Generation of Highly Persistent Superparamagnetic Nanorods. *Advanced Materials*, *20*(20), 3877-3881.

[266] Frka-Petesic, B., Erglis, K., Berret, J. F., Cebers, A., Dupuis, V., Fresnais, J., ... & Perzynski, R. (2011). Dynamics of paramagnetic nanostructured rods under rotating field. *Journal of Magnetism and Magnetic Materials*,*323*(10), 1309-1313.

[267] Kornev, K. G., Gu, Y., Aprelev, P., & Tokarev, A. (2015). Magnetic rotational spectroscopy for probing rheology of nanoliter droplets and thin films. *arXiv preprint arXiv:1503.05229*.

[268] Doi, M., & Edwards, S. F. (1988). *The theory of polymer dynamics* (Vol. 73). oxford university press.

[269] Perlov, C. M., & Middleman, S. (1987). Dynamics of orientation in particulate media. *Journal of Applied Physics*, *61*(8), 3892-3894.

[270] R. Courant and D. Hilbert, Methods of mathematical physics, Interscience Publishers, New York, 1989.

[271] Larson, R. G. The structure and rheology of complex fluids. 1999. *New York: Oxford*, *688*.

[272] Wang, D., Yang, J., Li, X., Geng, D., Li, R., Cai, M., ... & Sun, X. (2013). Layer by layer assembly of sandwiched graphene/SnO 2 nanorod/carbon nanostructures with ultrahigh lithium ion storage properties. *Energy & Environmental Science*, *6*(10), 2900-2906.

[273] Srivastava, S., & Kotov, N. A. (2008). Composite layer-by-layer (LBL) assembly with inorganic nanoparticles and nanowires. *Accounts of chemical research*, *41*(12), 1831-1841.

[274] R. E. Rosensweig, Ferrofluids, Magnetically Controllable Fluids and Their Applications (1997).

[275] Arsalani, N., Fattahi, H., & Nazarpoor, M. (2010). Synthesis and characterization of PVP-functionalized superparamagnetic Fe3O4 nanoparticles as an MRI contrast agent. *Express Polym Lett*, *4*(6), 329-38.

[276] Si, S., Li, C., Wang, X., Yu, D., Peng, Q., & Li, Y. (2005). Magnetic monodisperse Fe3O4 nanoparticles. *Crystal growth & design*, *5*(2), 391-393.

[277] Xuan, S., Wang, Y. X. J., Yu, J. C., & Cham-Fai Leung, K. (2009). Tuning the grain size and particle size of superparamagnetic Fe3O4 microparticles.*Chemistry of Materials*, *21*(21), 5079-5087.

[278] Carey, V. P., & Wemhoff, A. P. (2006). Disjoining pressure effects in ultra-thin liquid films in micropassages—comparison of thermodynamic theory with predictions of molecular dynamics simulations. *Journal of Heat Transfer*, *128*(12), 1276-1284.

[279] Neimark, A. V., & Kornev, K. G. (2000). Classification of equilibrium configurations of wetting films on planar substrates. *Langmuir*, *16*(13), 5526-5529.

[280] Kornev, K., & Shugai, G. (1998). Thermodynamic and hydrodynamic peculiarities of a foam lamella confined in a cylindrical pore. *Physical Review E*, *58*(6), 7606.

[281] Derjaguin, B. V., Churaev, N. V., Muller, V. M. Surface Forces, Plenum Press: New York, 1987.

[282] Kheifets, L. I., & Neimark, A. V. (1982). Multiphase processes in porous media. *Khimiya, Moscow*, 320.

[283] De Gennes, P. G. (1985). Wetting: statics and dynamics. *Reviews of modern physics*, *57*(3), 827.